Dynamic Ion Transport: From Electrolytic Cells to Conical Channels

Alexander Barnaveli

PhD thesis, Utrecht University, April 2024

ISBN: 978-94-6473-522-2

Cover Illustration: Alexander Barnaveli, pigment liner pen on paper.

- *Front cover* - Drawn during bachelor's at Tbilisi State University (TSU) 2015.
- *Rear cover* - Central illustration and top corner objects drawn at Callantsoog DRSTP School in 2022. Smaller figures drawn at TSU in 2015.

About the cover: As the reader will find out in the introduction of the thesis, the Electric Double Layers (EDLs) are essential for keeping our cells functioning, making EDLs of crucial importance for every living organism. Since this crucial importance is invariant of the living habitat of the organism $\partial I / \partial L_H = 0$, with I being the importance and L_H - the Living Habitat, the cover illustration serves as a manifestation of the EDLs uniting the huge variety of organisms and plants living under the ground, on the surface and in the air.

Dynamic Ion Transport: From Electrolytic Cells to Conical Channels

Dynamisch Ionentransport: Van Elektrolytische Cellen tot Kegelvormige Kanalen

(met een samenvatting in het Nederlands)

Proefschrift

ter verkrijging van de graad van doctor aan de Universiteit Utrecht op gezag van de rector magnificus, prof. dr. H.R.B.M. Kummeling, ingevolge het besluit van het college voor promoties in het openbaar te verdedigen op woensdag 3 juli 2024 des ochtends te 10.15 uur

door

Alexander Barnaveli

geboren op 9 mei 1995 te Tbilisi, Georgië

Promotoren:

Prof. dr. R.H.H.G. van Roij
Prof. dr. B.M. Mulder

Beoordelingscommissie:

Prof. dr. E. Alarcón Lladó
Prof. dr. R.A. Duine
Dr. J. de Graaf
Prof. dr. W.K. Kegel
Prof. dr. A.P. Mosk

TABLE OF CONTENTS

PREFACE

This Thesis is the result of four years of work at the Institute for Theoretical Physics of Utrecht University. This work is part of the Delta Institute for Theoretical Physics (DITP) consortium, a program of the Netherlands Organization for Scientific Research (NWO) that is funded by the Dutch Ministry of Education, Culture, and Science (OCW).

All the chapters in the thesis revolve around dynamic ionic transport driven by an externally applied alternating (AC) voltage. The first chapter (Introduction) is devoted to laying the necessary foundation for the following three chapters, where the main results of the research are presented.

At the end of the Thesis, the reader will find the bibliography, the summaries in English and Dutch and acknowledgments.

Alexander Barnaveli
April 2024, Utrecht

LIST OF PUBLICATIONS

This Thesis is based on the following publications:

- [1] **Barnaveli, A.** & van Roij, R. Asymmetric rectified electric fields: non-linearities and equivalent circuits. *Soft Matter* **20**, 704–716 (2024).
- [2] **Barnaveli, A.** & van Roij, R. Asymmetric rectified electric fields for symmetric electrolytes 2024. arXiv: 2404.15055 [cond-mat.soft]. (Accepted in ***Langmuir***)
- [3] **Barnaveli, A.,** Kamsma, T. M., Boon, W. Q. & van Roij, R. Pressure-Gated Microfluidic Memristor for Pulsatile Information Processing 2024. arXiv: 2404.15006 [cond-mat.soft].

Other publications by the author:

- **Barnaveli, A.,** Lucat, S. & Prokopec, T. Inflation as a spontaneous symmetry breaking of Weyl symmetry. *Journal of Cosmology and Astroparticle Physics* **2019**, 022 (2019).
- **Barnaveli, A. A.** & Shatashvili, N. L. Mechanism for flow generation/acceleration in dense degenerate stellar atmospheres. *Astrophysics and Space Science* **362**, 1–12 (2017).

1

GENERAL INTRODUCTION

SHORT OVERVIEW

In this chapter we introduce the basic information, ideas and notations needed for the later chapters of the thesis. We will start by introducing the field of Soft Condensed Matter field (SCM), discuss the main theoretical toolbox that one uses in SCM, where we also give an example the toolbox in action. In the second part of the chapter we cover the main element of the thesis - the Electric Double Layer (EDL). After describing the origins of EDLs together with briefly going through their history, we describe them mathematically by introducing the governing equations in both static and dynamic cases. At the end of the chapter we will also give a brief outline of the whole thesis and describe how it is structured.

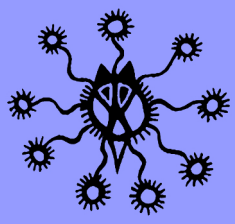

1.1 SOFT CONDENSED MATTER (SCM)

General description of Soft Condensed Matter

The seemingly simple task of categorizing different sub-fields of physics can quickly become complicated. Boundaries between them are often blurry, making it difficult to isolate one field from another. Sometimes, one area of physics serves as the foundation for another, as seen in how Quantum Field Theory contributes to certain aspects of Cosmology. Additionally, there is the complexity of discerning whether something constitutes a distinct sub-field of physics, as is the case with Astrophysics, or simply functions as a toolbox, as is the case with statistical physics or quantum mechanics.

Nevertheless, to see the big picture of physics, it is, in general, necessary to understand the approximate boundaries between its sub-fields and the toolboxes employed within each of them. Given the focus of this thesis on Soft Condensed Matter (SCM) systems, we will only discuss the boundaries and toolboxes relevant to SCM here.

Conveniently, almost all of this information is contained in the name of the field itself. Starting with **condensed matter**, it tells us that SCM is concerned with systems of "many" interacting constituents/particles. Here the word "many" implies the presence of particles in large quantities such that statistical physics methods are required to study the system, demonstrating the need for a statistical physics toolbox in SCM. And while this property can be attributed to any condensed matter system, what makes soft condensed matter systems stand out is their interaction energy scale, with the word **soft** denoting that the constituents of SCM systems have weak binding energies of the order of the thermal energy at room temperature, which amounts to (tens of) meV and can be relatively easily deformed by the external influence of the same energy order [4, 5]. This is in contrast with the typical interaction energies of the order of eV in Hard Condensed Matter (HCM) Systems [5], therefore significantly higher energies are needed to influence the structure of a HCM system (hence the names "hard" and "soft"). As a consequence, the microscopic structure of HCM is usually much more strictly organized than that of SCM systems, making it hard (or sometimes impossible) to predict

macroscopic features of a SCM system based on its microscopic building blocks [4].

At the same time, SCM system constituents are not only limited by the interaction energy scales, but also their size. The typical building blocks of SCM systems are of the mesoscopic scale i.e. larger than microscopic, such as electrons, and smaller than macroscopic, such as stones, marbles or grains of sand [6]. Stemming from the demand that the SCM system stays classical rather than quantummechanical, the microscopic scale sets the lower boundary for the size of an SCM system element. Mathematically speaking the size of a building block should be much larger than its characteristic thermal de Broglie wavelength. On the other end, if we keep increasing the size of particles, they will inevitably get heavy enough such that thermal collisions from the environment will fail to displace them in a meaningful way to keep them spread throughout the system and they will sediment to the bottom under the influence of the gravitational pull. This sets the upper limit for the length scales of an SCM system building block. Thus, based on the above restrictions we can roughly estimate the typical sizes of SCM building blocks to range approximately between 1nm to 1μm [5].

A system satisfying all the requirements stated above, is considered to be a SCM system and there are plenty of them surrounding us in our everyday life. Some of the examples of SCM systems include emulsions (mixtures of two immiscible liquids, such as oil and water, stabilized by an emulsifying agent. Examples include mayonnaise, salad dressings, and milk), foams (whipped cream, shaving cream, and foam cushions), gels (gelatin desserts, hair gel, and toothpaste), paint, ketchup, soap bubbles, lipid bilayer of cell membranes and the cytoskeleton within cells, polymers (for instance plastics, rubber, and synthetic fibers like nylon and polyester), etc. [6].

Due to their diverse nature soft condensed matter (or simply soft matter) systems showcase a wide range of behaviors. For example, SCM materials can exhibit self-assembly capabilities, forming complex structures like colloidal crystals or liquid crystal phases [4]. Furthermore, phase transitions within soft matter, triggered by factors like temperature or pressure changes, result in significant shifts in material properties, transitioning between liquid and solid states or forming liquid crystal phases. Moreover, soft matter materials demonstrate responsive behavior to external stimuli, like temperature or

pH changes, making them useful for applications such as drug delivery and tissue engineering. Additionally, the viscoelastic nature of certain SCM systems allows for a blend of fluid-like flow and solid-like elasticity, seen in materials such as polymer gels and biological tissues. They can also exhibit nonlinear rheological behavior, with responses to stress deviating from linearity, leading to phenomena like shear-thinning or shear-thickening. Amidst thermal fluctuations, soft matter materials remain in continuous motion, driven by molecular dynamics and interparticle forces, highlighting their complexity and relevance across scientific research and technological applications [7–10].

SCM Toolbox - Statistical Physics

Statistical physics offers an effective and practical way to understand complex systems. Instead of tracking every single constituent particle of the system, which would be challenging and time-consuming (if possible at all), it focuses on the overall patterns and averages across all particles to give conclusions about the macroscopic features of the system. By looking at these averages, statistical physics helps us see the bigger picture and understand how systems behave on a larger scale.

Imagine you are standing at the edge of a vast forest, observing the canopy stretching out before you and trying to memorize the view to describe it to a friend later. Rather than focusing on every single leaf and branch, identifying their colors, how they move when the wind blows and how they look under different light patterns that the shadows create, you concentrate your attention on identifying broader patterns such as the distribution of tree species, colors of the patches (rather than individual leaves) that they form, the density of vegetation and the overall shape of the forest. This is an effective approach, as this broad view provides insights into the forest as a whole, without needing to analyze each individual component of it. Of course, one could bring a pair of binoculars and start studying each individual leaf and branch to then assemble the big picture of the forest, however, even though it would lead to a precise result, this is going to be extremely time consuming and a very challenging task or, most of the time, even a downright impossible one.

Similarly, in statistical physics, while studying a system we take a step back from the microscopic details of individual constituent particles and focus on broader statistical averages. By analyzing these statistical quantities, we build a picture of how a system behaves on a larger scale, without getting lost in the individual particle interaction intricacies.

Another good example would be how we calculate the temperature of a body. For instance, think about a cup of hot tea left on the table. Over time tea gradually cools down until it reaches room temperature. At a microscopic level, tea consists of countless molecules in constant motion. As these molecules collide with each other and with the walls of the cup, they transfer energy to the surroundings, causing the temperature of the tea to decrease. Similarly to the previous example, rather than tracking each individual particle and its velocity evolution to predict how the temperature changes over time, statistical physics does this by only considering the average velocity (kinetic energy) of these molecules. This understanding helps explain why the tea eventually reaches a thermal equilibrium with its surroundings.

It is also beneficial to quickly go through the mathematical details of the above example by calculating the temperature of a body placed in an external heat reservoir using Boltzmann and Maxwell statistical distributions [11]. Besides this derivation serving a purpose of demonstrating convenience of statistical physics, we will also need the Boltzmann distribution later in the thesis, thus deriving it here is beneficial for this reason as well.

The Boltzmann distribution, also known as the Gibbs distribution in statistical mechanics, describes the relative probabilities of particles occupying different energy states in a system at thermal equilibrium. To derive it we consider system A submerged in a very large heat reservoir R. In thermal equilibrium both the system and the reservoir are characterized by the same temperature T, whereas their energies, E and E_r respectively, are not fixed and can vary from 0 to E_0, where E_0 is the energy of a combined system+reservoir system, such that

$$E + E_r = E_0 = \text{const.} \tag{1.1}$$

Considering that the reservoir is much larger than the system A by definition, we can rewrite Eq.(1.1) as

$$\frac{E}{E_0} = \left(1 - \frac{E_r}{E_0}\right) \ll 1. \tag{1.2}$$

Given the system is in a state with a certain energy E, the reservoir can still be in any of the numerous states $\Omega_r(E_r)$ such that the corresponding value of E_r satisfies Eq.(1.1). Additionally, taking into account that the reservoir is equally likely to be in any one of these $\Omega_r(E_r)$ states, the probability of finding it at energy E_r would be proportional to the number $\Omega_r(E_r)$ itself

$$P(E_r) \propto \Omega_r(E_r) \equiv \Omega_r(E_0 - E), \tag{1.3}$$

which can be expanded around $E_r = E_0$, i.e. $E = 0$ point. For convenience we consider the logarithm of Eq.(1.3)

$$\ln \Omega_r(E_r) = \ln \Omega_r(E_0) + \left(\frac{\partial \Omega_r}{\partial E_r}\right)_{E_r = E_0} + \ldots \approx \text{const} - \beta_r E, \tag{1.4}$$

where

$$\beta_r \equiv \frac{\partial \Omega_r}{\partial E_r} \tag{1.5}$$

and in equilibrium $\beta = \beta_r = 1/k_B T$, where k_B is the so-called Boltzmann constant. Now inserting Eq.(1.4) into Eq.(1.3) and normalizing by demanding that the probabilities sum up to 1, we get the expression for the probability of system A to be in a state with energy E at temperature T

$$P(E) = \frac{e^{-\beta E}}{\sum_{ms} e^{-\beta E}}. \tag{1.6}$$

Here $\sum_{ms}$ is the summation over all microstates available for the system A while having temperature T. Eq.(1.6) is called the Boltzmann distribution and describes the energy distribution of the system. It can now be used to derive Maxwell's distribution, which provides a statistical description of the distribution of speeds of gas molecules in a gas at equilibrium at a given temperature T. The Boltzmann distribution for the speed v of gas molecules is given by

$$P(v) = 4\pi \left(\frac{m}{2\pi k_B T}\right)^{\frac{3}{2}} v^2 e^{-\frac{mv^2}{2k_B T}}, \tag{1.7}$$

where m is the mass of the gas molecule, T is the temperature of the gas. The typical velocity v_t of a molecule will correspond to the maximum of $P(v)$ function

$$\frac{\mathrm{d}P(v)}{\mathrm{d}v} = 0 \quad \rightarrow \quad v_t = \sqrt{\frac{2k_BT}{m}}, \tag{1.8}$$

which at room temperature $T = 300K$ for N_2 gives $v_t \approx 422$m/s. This derivation illustrates how the Maxwell velocity distribution provides a statistical description of the velocities of gas molecules in thermal equilibrium, allowing us to conveniently derive macroscopic properties of a body such as temperature by relying on particle velocity averages, rather than tracking the motion and details of each individual molecule.

1.2 ELECTRIC DOUBLE LAYER (EDL)

In this thesis we will be dealing with aqueous systems containing ions, therefore in this section we will cover the basics of such systems.

Objects Submersed in Liquid

The presence of mesoscopic particles in a liquid can give rise to many interesting collective phenomena such as pattern formation in liquids through self-organization mechanisms [12–14], self-assembly of structures [4], electrokinetic processes (e.g. matter transport, discussed in the final part of the thesis) including streaming current, electrophoresis, electro-osmosis, etc. [15]. Studying behavior of such liquids and ions contained in them is one of the central topics of soft condensed matter physics.

One particularly interesting topic of study in this area is the behavior of liquid systems containing charged particles under the influence of externally applied thermal scale electric field. To understand the importance of such systems both in general and in life of all living organisms in particular, let us consider the interaction of two oppositely charged particles with charges $q_1 = q$ and $q_2 = -q$ in two different media - air and water. We know that these charges interact with Coulomb interaction

$$F = \frac{1}{4\pi\varepsilon_0\varepsilon}\frac{q_1q_2}{r^2}, \tag{1.9}$$

where ε_0 is the vacuum permittivity, ε is the relative dielectric constant of the medium and r is the distance between the charges. We see that the force is inversely proportional to the dielectric permittivity of the medium, therefore large values of ε will significantly decrease the interaction force of the charges. Comparing the dielectric constant of water ε_{water} to that of air ε_{air}, we find that ε_{water} is approximately 80 times larger than ε_{air}. Consequently, the forces between charges in water are correspondingly weaker by a factor of 80. The high dielectric constant of water is attributed to the dipole nature of water molecules, which also accounts for the ability of salts, being also polar, to dissolve in water. Water molecules polarise and form a "hydration shell" around the ions [16–18], which weakens the bond between the salt ions to the extent that thermal energy becomes sufficient to dissociate the salt into its constituent parts, allowing it to dissolve in water.

Since even the purest de-ionized water, which has a pH value of around 7, contains some amount of salt, it is fair to state that water (and other liquids with high dielectric constants) usually contains a large amount of free ions that can be manipulated by externally applied electric fields.

Based on all the above and given that liquids such as water are found everywhere around us and play important roles in our bodies, as well as various industries, it is interesting to study how systems with such liquids behave when exposed to external electric fields. Moreover, the application of external electric fields is a convenient and versatile method for manipulating these systems [19–21], further enhancing the scientific interest in their study.

A (Very) Brief History of Electric Double Layers (EDLs)

Due to the abundance of liquids in biological systems and nature overall, the dissociation effect described above has far-reaching implications. Essentially, any non-hydrophobic solid surface in contact with water will experience this dissociation process, releasing ions into the liquid. These ions undergo thermal collisions trying to disperse them uniformly in the water. However, due to electric interactions, the ionized surface of the solid continues to exert an attracting force on the ions, preventing their complete dispersion. Consequently, a diffuse layer of charges accumulates at the surface, effectively screening its electric potential. This layer, along with the ionized surface,

constitutes an Electric Double Layer (EDL). Thus, any non-hydrophobic object submersed into water gets an EDL around it. This is the reason, why, for example, constituents of our cells can stay separated in an aqueous environment [22–24], implying that all organic life on earth owes its existence to EDLs! Interestingly, EDLs can be made to form even in some hydrophobic cases as is in case of homogenized milk, where EDLs form around fat droplets, prohibiting them to aggregate into a separate phase from the rest of the liquid. In the unhomogenized milk straight from the cow there would eventually be the phase separation between milk and fat. However, milk is usually homogenized by breaking up fat clumps into many smaller ones (fat globules). Stability of the solution is ensured by the charge carrying proteins attaching to the membrane of the fat globules, leading to EDL formation around globules and making them repel each other and not phase separate as a result [25–28].

The initial concept of an EDL was introduced in 1853 by Helmholtz, who showed that an electric double layer stores charge electrostatically, acting like a molecular capacitor [29]. Importantly, however, in Helmholtz's model the charge stored in an EDL depends linearly on the applied voltage, leading to a constant differential capacitance (ratio of rate of change of the stored charge and the rate of change of the voltage applied to the surface). While this model was able to describe the basics of EDLs well, it still needed a lot of refinement, as it was not taking into account important effects such as impurity of EDL structure, ionic entropy, ion adsorption to the surface, ion size etc.

The first major improvements came from Louis Georges Gouy and David Leonard Chapman, who independently observed variability of the differential capacitance in 1910 and 1913, respectively [30, 31]. They pioneered the idea of an EDL consisting of a diffuse layer of charges gathered at the electrode. The distribution of charges was established to follow Maxwell-Boltzmann statistics, decaying exponentially away from the electrode into the liquid bulk.

Further refinements to the model were introduced by Stern, Grahame and others. Stern came to the conclusion that an EDL can be described by a mixture of Helmholtz's and Gouy-Chapman's ideas. Some ions of the EDL get adsorbed to the surface of the electrode, forming a firm layer attached

to it, like in Helmholtz's model. However, the majority of ions stay close to the electrode in the form of a Gouy-Chapman diffuse layer [32]. And in 1947 Grahame was the first one to suggest the impurity of an EDL, claiming, that some ions can penetrate the Stern layer, though, this is not a very common occurence [33].

While there are other notable improvements to the original Helmholtz's model of an EDL, in this thesis we are not going to delve into the such details of EDL structure and we will treat EDLs within the Gouy-Chapman framework.

1.2.1 *Equilibrium EDL - Poisson-Boltzmann Distribution*

A system allowing us to conveniently describe an EDL mathematically consists of a semi-infinite 3D aqueous electrolyte of relative dielectric constant ε at room temperature T being bounded by a macroscopic planar electrode from one side while extending infinitely in the other direction, where we assume translational invariance in the lateral directions. The electrolyte consists of two types of monovalent point-like ions: cations $(+)$ and anions $(-)$ characterized by valencies $z_\pm = \pm 1$ and diffusion coefficients $D_\pm$. The total number of cations and anions is equal, hence the total system is electroneutral. We fix the concentrations of ions at bulk concentration c_s far away from the electrode, which is blocking, so that no ion can penetrate it and we exclude any chemical REDOX reactions. Thus $c_\pm(z \to \infty) = c_s$. We also exclude surface chemistry, so that an electrode submerged in liquid would not acquire an EDL via the dissociation mechanism described above. A schematic representation of the system is shown in Fig. 1.1.

Initially electrode is not charged and as a result the ions are spread evenly by entropic forces across the bulk liquid, as seen in Fig. 1.1(a). If we now apply a positive surface charge $\sigma_c > 0$ to the electrode, the negative charges will get attracted to it and the positive ones repelled, such that they form an EDL, as seen in Fig. 1.1(b).

In order to describe the EDL analytically, we need to connect the electric potential to the charge distribution in the system. For this we recall the

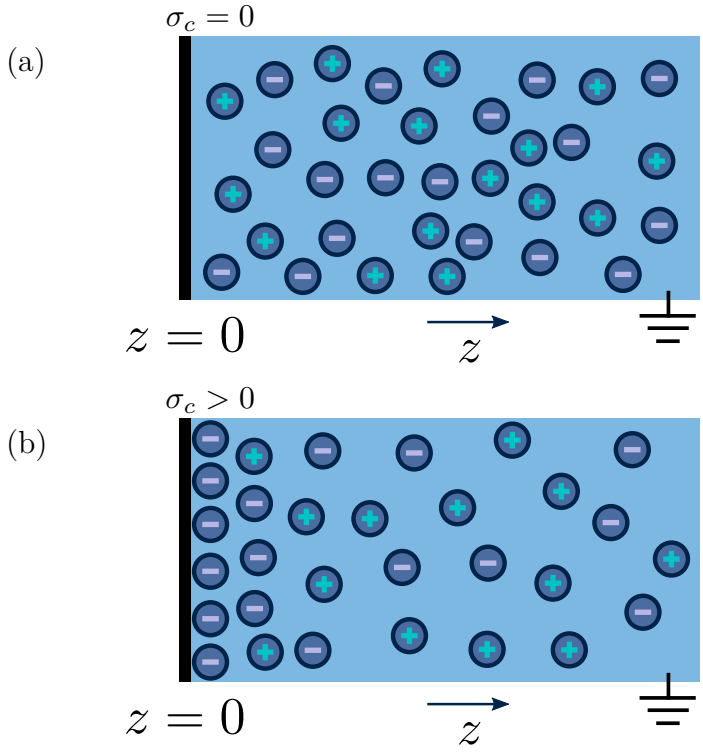

Figure 1.1: Schematic representation of the aqueous 1:1 electrolyte of interest containing a continuum solvent and two ionic species in a semi-infinite system bounded from the left by a planar blocking electrode. The bulk of the electrolyte is grounded so that $\Psi(z \to \infty) = 0$. In (a) the electrode is not charged $\sigma_c = 0$ and the ions are spread evenly across the electrolyte, whereas in (b) a positive surface charge density $\sigma_c > 0$ is applied to the electrode, leading to aggregation of a negative layer of ions in its vicinity, forming an EDL.

Coulomb law describing electric field $E \equiv -\nabla\Psi$ originating from a point charge

$$-\nabla\Psi = \frac{\hat{\mathbf{r}}}{|\mathbf{r}|^2}\frac{e}{4\pi\varepsilon\varepsilon_0}, \tag{1.10}$$

where e is the elementary charge and $\hat{\mathbf{r}}$ is the unit vector. If we take the divergence of the electric field, it becomes clear that the electric field is sourced by the localized point charge $\nabla\Psi^2 = -e\delta(\mathbf{r})/\varepsilon\varepsilon_0$, where $\delta(\mathbf{r})$ is the Dirac delta function. And as $\nabla\Psi \propto e$ is a linear relation, for a collection of charges the electric field will simply be a sum of electric fields created by the individual charges

$$\nabla^2\Psi = -\frac{e}{\varepsilon\varepsilon_0}c_e(\mathbf{r}), \tag{1.11}$$

where $c_e(\mathbf{r}) = c_+(z) - c_-(z)$ is the ionic charge distribution in the system. This equation is called Poisson equation and describes the relation of the electric potential to the charge distribution in the system.

This, however, is not enough to describe the system, as we have 3 unknown functions Ψ, c_+ and c_- in this equation, so we need two additional relations connecting electric potential to charge concentrations to close the system of equations. For this we employ the aforementioned Boltzmann distribution of Eq.(1.6), as it connects the distribution of ion con,

$$c_\pm(z) = c_s \exp[\mp\beta e\Psi(z)], \tag{1.12}$$

where $\beta = 1/k_BT$. Eqs.(1.11) and (1.12), called Poisson-Boltzmann (PB) equation, form a set of self-consistent equations, solving which gives us analytical results for the distributions of ion concentrations and electric potential in the system.

Poisson-Boltzmann Analytical Solution

For a general geometry the set of PB equations does not have an analytic solution. However, in certain simple geometries like the single plate geometry of Fig. 1.1(a) PB equations can, fortunately, be solved, shedding some light on the EDL structure.

We start by inserting Eq.(1.12) into Eq.(1.11), leading to a second order differential equation

$$\frac{\mathrm{d}^2\Psi(z)}{\mathrm{d}z^2} = \frac{2c_s e}{\varepsilon_0\varepsilon}\sinh(-\beta e\Psi(z)), \tag{1.13}$$

which needs two boundary conditions

$$\Psi(z)|_{z\to\infty} = 0, \tag{1.14}$$

$$\sigma_c = -\int_0^\infty c(z)\mathrm{d}z, \tag{1.15}$$

where $c(z) = c_+(z) - c_+(z)$ and $\sigma_c = \sigma/e$ is the surface charge density on the electrode. Both of the boundary conditions are constructed using the fact that in equilibrium EDL fully screens electric potential of the electrode. The first one describes the electric potential far away from the electrode, whereas the second one equates the total excess charge gathered at the electrode to the surface charge on the electrode, so that the total system stays charge neutral. Eq.(1.15) can be further simplified by using Eq.(1.11), so that by combining it with Eq.(1.13) and Eq.(1.14) we arrive at the system of equations that we have to solve

$$\nabla^2\Phi(z) = \kappa^2 \sinh(\Phi(z)), \tag{1.16}$$

$$\nabla\Phi(z)|_{z=0} = -4\pi\lambda_B\sigma_c, \tag{1.17}$$

$$\Phi(z)|_{z\to\infty} = 0, \tag{1.18}$$

where we introduced a convenient re-scaled electric potential

$$\Phi(z) \equiv \frac{e\Psi(z)}{k_B T} \tag{1.19}$$

and κ - a coefficient with dimensions of inverse length, physical meaning of which is given below. Integrating the equations and using the boundary conditions we arrive at the expressions describing the profile of the electric potential as well as the concentration of charges

$$\Phi(z) = 2\log\left(\frac{1+\gamma e^{-z/\lambda_D}}{1-\gamma e^{-z/\lambda_D}}\right), \tag{1.20}$$

$$c_\pm(z) = c_s\left(\frac{1\mp\gamma e^{-z/\lambda_D}}{1\pm\gamma e^{-z/\lambda_D}}\right)^2, \tag{1.21}$$

where

$$\gamma = \frac{\sqrt{1+(y/2)^2}-1}{y/2}, \qquad \text{with} \qquad y = -4\pi\lambda_B\lambda_D\sigma_c, \tag{1.22}$$

where

$$\lambda_B = \frac{e^2}{4\pi\varepsilon\varepsilon_0 k_B T} \tag{1.23}$$

is called the Bjerrum length and characterizes the solvent by denoting the distance, over which the value of the electric interaction potential between two dissolved unit charges e is equal to $k_B T$. The second length scale

$$\lambda_D = \sqrt{\frac{1}{8\pi\lambda_B c_s}}, \tag{1.24}$$

which can also be denoted as κ^{-1}, is called the Debye length and is a characteristic length of an EDL. It denotes how fast the exponents of the electric potential and the charge concentration decay when moving away from the electrode. The decay profile for the electric potential can be seen in Fig. 1.2(a), which gets fully screened by the EDL as we get far away from the electrode. A similar behavior can be seen in Fig. 1.2(b), where due to the positive charge on the electrode the concentration of the negative ions increases exponentially as we approach the electrode, whereas that of the negative ions decreases. In the bulk, far away from the electrode, both concentrations converge to the bulk concentration c_s.

Grahame Equation

For future convenience here we also derive an expression describing how the surface charge σ is connected to the magnitude of the electrode potential Ψ_0 explicitly.

For this we integrate the PB equation of Eq.(1.16) where we employ the variable change $s \equiv \kappa z$ to arrive at

$$\frac{\mathrm{d}\Phi(s)}{\mathrm{d}s} = 2\sinh\left(\frac{\Phi(s)}{2}\right)\mathrm{sgn}(\Phi(s)), \tag{1.25}$$

where we now change the variable back to z

$$\kappa^{-1}\frac{\mathrm{d}\Phi(z)}{\mathrm{d}z} = 2\sinh\left(\frac{\Phi(z)}{2}\right) \tag{1.26}$$

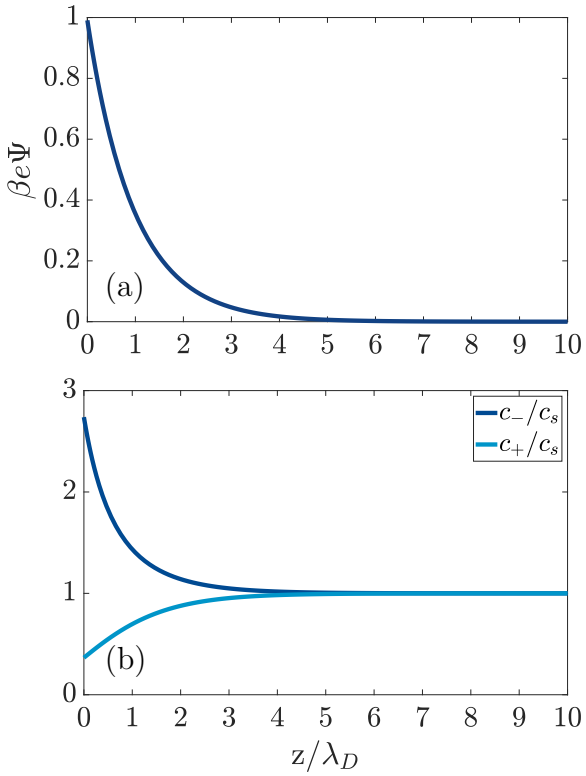

Figure 1.2: Profiles of (a) electric potential and (b) ion concentrations for a semi-infinite system with a planar blocking electrode in contact with an semi-infinite electrolyte. In (a) the potential decreases to 0 far away from the electrode as it gets screened by the EDL. In (b) the charges decrease exponentially with the distance from the electrode converging to bulk density c_s far away from it. Surface charge $\sigma = 1.8 \cdot 10^{-3}\text{C/m}^2$ corresponds to the zeta potential of $\beta e\Psi_0 = 1$. As an electrolyte we used water at room temperature $T = 293\text{K}$ with dielectric constant $\varepsilon = 78.5$. The bulk ionic concentration was taken to be $c_s = 0.93\text{mM}$ corresponding to the Debye length of $\lambda_D = 10\text{nm}$.

and employ Gauss' law for an infinite, charged plate

$$\hat{\mathbf{n}} \cdot \nabla \Psi = \frac{\sigma}{\varepsilon \varepsilon_0}, \tag{1.27}$$

where $\hat{\mathbf{n}}$ is the outer normal to the surface. This leads us to

$$\frac{e\Psi_0}{k_B T} = 2\sinh^{-1}\left(2\pi\lambda_D\lambda_B\sigma_c\right), \tag{1.28}$$

called the Grahame equation, relating the surface charge σ to the surface potential Ψ_0.

1.2.2 *Non-equilibrium EDL: Poisson-Nernst-Planck-Stokes equations*

In contrast to the static analysis of Electric Double Layers, dynamic electrochemical systems experience a far wider range of effects.

Langevin Force Balance Equation

The only equation that stays the same when we transition from the static equilibrium case to the dynamic non-equilibrium case is the Poisson equation (1.11), as the relationship between the charge distribution in the system with the profile of the electric potential does not change, as long as retardation effects can be ignored. The Boltzmann distribution, on the other hand, being an equilibrium distribution is not directly applicable anymore. In the dynamic case it gets substituted by the Nernst-Planck (NP) equation describing the ion transport under the influence of external forces.

The reason for a wider range of effects in the dynamic case is the variety of sources affecting ion movement in the system. To describe this, we employ a force balance equation which we will now construct.

Consider a particle of mass m moving through a fluid. Since there is a preferred direction in the system along the movement path of the particle, the distribution of collisions with other particles across the surface of the moving particle will be asymmetric and skewed towards the patch of the particle surface that is at the forefront of the movement direction i.e. its "front" part. This creates a friction force $m\xi\mathbf{v}(t)$ which is proportional to the velocity of the particle and is characterized by the friction coefficient ξ. Therefore in absence of external forces and thermal fluctuations the force balance equation, called Langevin equation can be written as

$$m\frac{\mathrm{d}\mathbf{v}_{\pm}(t)}{\mathrm{d}t} = -m\xi\mathbf{v}_{\pm}(t), \tag{1.29}$$

bringing any particle to rest according to the solution $\mathbf{v}(t) = \mathbf{v}_0 \exp(-\xi t)$, with $\mathbf{v_0}$ the initial velocity. In this thesis, however, we will be working with charged particles moving in a fluid at room temperature $T = 293K$ under the influence of an external electric field, implying presence of additional external force terms and fluctuations on the right hand side of the Langevin equation (1.29).

First, as the fluid moves, advection of particles by the fluid can also be considered as a force $m\xi\mathbf{u}$, which is proportional to the fluid velocity. Since we will be working at the room temperature, there will be a random thermal force $\mathbf{f}(t)$ acting on the particle. And finally, external electric field will subject ions to the electric force $\mp e\nabla\Psi$ for charges $\pm e$. Collecting these terms in the Langevin equation results in

$$m\frac{\mathrm{d}\mathbf{v}_\pm(t)}{\mathrm{d}t} = -m\xi(\mathbf{v}_\pm(t) - \mathbf{u}) \mp e\nabla\Psi + \mathbf{f}(t), \tag{1.30}$$

where the advection and random force terms will be discussed in more detail below. In absence of thermal collisions the equilibrium velocity reached by the ion is going to be

$$\mathbf{v}_\pm = \mp e\nabla\Psi/(m\xi) + \mathbf{u} \tag{1.31}$$

when $t \gg \xi^{-1}$, independent of the initial velocity. For the typical parameter values of this thesis the terminal velocity is of the order of ~ 1mm/s.

Ionic diffusion

We start with the diffusive term due to thermal collisions $\mathbf{f}(t)$. As described in the initial section of this chapter, the energy ranges of the systems that we consider are such that thermal collisions in electrolyte play a role comparable to that of the external forces applied to the system. Thermal collisions can be described by a random force $\mathbf{f}(t)$ applied to ions. The main feature of this force is that it has a zero mean $\langle\mathbf{f}(t)\rangle = 0$ (where $\langle\ldots\rangle$ denotes an ensemble average over the solved degrees of freedom), while having a non-zero mean square amplitude $\langle f_i(t) f_j(t')\rangle = 2mk_BT\xi\delta_{ij}\delta(t-t')$, where δ_{ij} is the Kronecker-delta [34].

In order to find the effect of thermal collisions on the transport of the ions in electrolyte we substitute the above force $\mathbf{f}(t)$ into the Langevin equation

(1.30) assuming that no other external forces act on the ions, i.e. $\nabla\Psi = 0$ and $\mathbf{u} = 0$. The resulting equation

$$m\frac{\mathrm{d}\mathbf{v}_{\pm}(t)}{\mathrm{d}t} = -m\xi\mathbf{v}_{\pm}(t) + \mathbf{f}(t) \tag{1.32}$$

can be solved for $\mathbf{v}(t)$

$$\mathbf{v}(t) = \mathbf{v}_0\exp(-\xi t) + \frac{1}{m}\int_0^t \mathrm{d}s\mathbf{f}(s)\exp(\xi(s-t)), \tag{1.33}$$

however, in order for this solution to be useful, one needs to know the properties of $\mathbf{f}(t)$. Due to its random nature, the only known characteristic is its expectation value, thus, instead of studying $\mathbf{v}(t)$ we draw our attention to $\langle\mathbf{v}(t)\cdot\mathbf{v}(t')\rangle$, which after performing some algebra can be shown to be

$$\langle\mathbf{v}(t)\cdot\mathbf{v}(t')\rangle = 3k_BT\exp(-\xi'|t-t'|))/m, \tag{1.34}$$

which also satisfies the equipartition condition $(m/2)\langle\mathbf{v}(t')\cdot\mathbf{v}(t')\rangle = 3k_BT/2$ at equal state times, as it should if the coefficient of the random force correlation function $2mk_BT\xi$ was chosen correctly. With this we can now calculate the displacement of the ion from its origin $\mathbf{R}(t)$ at time t

$$\mathbf{R}(t) = \mathbf{R}(0) + \int_0^t \mathrm{d}s\mathbf{v}(s). \tag{1.35}$$

Due to the nature of $\mathbf{v}(t)$ this translates into a zero mean displacement for the ion

$$\langle\mathbf{R}(t) - \mathbf{R}(0)\rangle = 0, \tag{1.36}$$

and in 3 dimensions a non-zero mean-squared displacement

$$\langle|\mathbf{R}(t) - \mathbf{R}(0)|^2\rangle = \int_0^t\int_0^t \mathrm{d}s\mathrm{d}s'\langle\mathbf{v}(t)\cdot\mathbf{v}(t')\rangle \approx 6Dt \quad \text{if} \quad t \gg \xi^{-1}. \tag{1.37}$$

Here $D \equiv k_BT/(m\xi)$ is defined as a diffusion coefficient of ions and has dimensions of m^2/s, implying that the typical time t it takes an ion to travel a distance $|\mathbf{R}|$ from its origin at $t = 0$ under the influence of thermal fluctuation is $\tau \propto |\mathbf{R}|^2/D$. Phenomenologically one can also determine $\xi = \frac{6\pi\eta a}{m}$, where a is the radius of ion and η the viscosity of the medium. From this we can also get the famous Stokes-Einstein expression for the diffusion coefficient

$$D = \frac{k_B T}{6\pi\eta a}. \tag{1.38}$$

A typical diffusion coefficient for $a = 0.2$nm and $\eta = 1$ mPa·s is $D = 10^{-9}\text{m}^2/\text{s}$. Equations (1.36) and (1.37) imply that the ion does get displaced from its origin $R(t = 0)$ on average, however, there is no preferred displacement direction due to the random nature of $\mathbf{f}(t)$ force. All this indicates, that the probability distribution $p(\mathbf{R}, t)$ of finding an ion at time t at a position $\mathbf{R}$ relative to its origin at $t = 0$ should be a Gaussian distribution with variance $6Dt$ and zero mean and can be written as

$$p(\mathbf{R}, t) = \frac{1}{(12\pi Dt)^{3/2}} e^{-\frac{|\mathbf{R}|^2}{12Dt}}. \tag{1.39}$$

Evolution of this probability distribution gives the desired equation of motion of a particle undergoing diffusion due to thermal collisions

$$\partial_t p(\mathbf{R}, t) = D\nabla^2 p(\mathbf{R}, t), \tag{1.40}$$

called the diffusion equation, which also yields Fick's law $\mathbf{J} = -D\nabla p$ for the diffusive flux.

Ion Advection and Fluid Flow

Now we turn our attention to the bulk fluid motion. As the liquid flows within the system, ions are transported along with it, following the fluid dynamics. Fluid flow is mathematically described in terms of velocity distribution $\mathbf{u}(x, y, z, t)$ and two thermodynamic properties: pressure $p(x, y, z, t)$ and mass density $\rho_m(x, y, z, t)$. The equation connecting these functions is the Navier-Stokes equation

$$\rho_m \frac{\partial \mathbf{u}}{\partial t} + \mathbf{u} \cdot \nabla \mathbf{u} = \eta \nabla^2 \mathbf{u} - \nabla p - e(c_+ - c_-)\nabla \Psi, \tag{1.41}$$

the most general equation governing the viscous fluid flow. It can be, however, significantly simplified in many cases. Different layers of liquid can have different velocities and if the difference is large enough for neighboring layers, they can start mixing creating a turbulent flow. The viscosity of the fluid is counteracting this effect by damping the fluid motion and if it is strong

enough, the flow will be laminar. This competition is described by the Reynolds number $\mathrm{Re} = uL/\nu$, where L is the typical linear size of the system where the liquid is flowing and ν the kinematic viscosity. Thus, depending on the scale of the system, the above term can be neglected. Throughout this thesis we will be considering flows on a micrometer scale, where $\mathrm{Re} \ll 1$, hence the flow will be laminar and instead of Navier-Stokes equation, liquid flow will be governed by the incompressible Stokes equation

$$\rho_m \frac{\partial \mathbf{u}}{\partial t} = \eta \nabla^2 \mathbf{u} - \nabla p - e(c_+ - c_-)\nabla \Psi; \qquad \nabla \cdot \mathbf{u} = 0, \tag{1.42}$$

where the continuity equation of fluid flow $\partial \rho_m / \partial t = -\nabla \cdot (\rho_m \mathbf{u})$ transforms into $\nabla \cdot \mathbf{u} = 0$, because $\rho_m = \text{const.}$, denoting incompressibility.

Ionic Flux - Nernst-Planck Equation

Having discussed the mechanisms of individual ion movement in the electrolyte, we can now combine these results and write down an expression for the ionic flux density in the electrolyte. We define ionic densities $c_\pm = pN_\pm/V$ and fluxes $\mathbf{J}_\pm = c_\pm \mathbf{v}_\pm$, where $N_\pm$ is the number of negative and positive ions in the unit volume V. We also assume absence of interparticle correlations beyond mean field, allowing us to simply convert the above results for individual ions into the equation of motion for ion concentrations. Such a treatment is valid until we stay at low concentrations $c_\pm \lesssim 1\mathrm{M}$, as for dense electrolytes interparticle interactions become large enough to significantly change the dynamics of ionic movement. In this thesis we stay in the dilute regime, thus Eq. (1.31) can be written as

$$\partial_t c_\pm(\mathbf{R}, t) = D \nabla^2 c_\pm(\mathbf{R}, t). \tag{1.43}$$

Recalling the continuity equation

$$\partial_t c_\pm = -\nabla \cdot \mathbf{J}_\pm, \tag{1.44}$$

we can interpret the left hand side of Eq.(1.43) as the contribution of diffusion to the ionic flux, $\mathbf{J}_\pm = -D\nabla c_\pm$. At the same time rewriting the ionic flux in terms of individual ion velocity $\mathbf{J}_\pm = \mathbf{v}_\pm c_\pm$ allows us to insert Eq. (1.31), describing the terminal velocity of ions when exposed to the electric field and

fluid flow, into the continuity equation to obtain the diffusion-conduction-advection equation

$$\partial_t c_\pm = D\left(\nabla^2 c_\pm \pm \nabla\cdot\left(c_\pm \frac{e\nabla\Psi}{k_B T}\right)\right) - \nabla\cdot(c_\pm \mathbf{u}), \tag{1.45}$$

called Fokker-Planck or Smoluchowski equation. Comparing it to Eq.(1.44) finally allows us to write the desired expression for the ionic flux in the system as

$$\mathbf{J}_\pm = -D\left(\nabla c_\pm \pm c_\pm \frac{e\nabla\Psi}{k_B T}\right) + c_\pm \mathbf{u}, \tag{1.46}$$

called Nernst-Planck equation, which in equilibrium, when $\partial/\partial t = 0$, $J_\pm = 0$ and $\mathbf{u} = 0$, reads

$$\nabla c_\pm \pm c_\pm \frac{e\nabla\Psi}{k_B T} = 0,$$

and leads to the Poisson-Boltzmann distribution

$$c_\pm(\mathbf{r}) = c_s e^{\mp\beta e\Psi(\mathbf{r})},$$

where $c_{\pm,s}$ is the bulk concentration of the ions.

Closed set of equations

Now we have all the necessary equations to describe the system. Interaction of the electric potential with the distribution of ions in the system is governed by the Poisson equation (1.11). How the ionic fluxes are driven by the electric field, diffusion and advection is determined by the Nernst-Planck equation (1.46), whereas fluid dynamics is described by the Stokes equation (1.42) augmented by the incompressibility condition $\nabla\cdot\mathbf{u} = 0$. These equations, collectively named Poisson-Nernst-Planck-Stokes (PNPS) equations, complete a set of linear second-order differential equations for $\rho_\pm$, $\mathbf{J}_\pm$, Ψ, $\mathbf{u}$, and p, describing the non-equilibrium dynamics of ion concentrations, electric potential and fluid flow in an electrolytical system subjected to external electric and mechanical forces

$$\nabla^2 \Psi = -\frac{e}{\varepsilon \varepsilon_0} c_e, \tag{1.47}$$

$$\rho_m \frac{\partial \mathbf{u}}{\partial t} = \eta \nabla^2 \mathbf{u} - \nabla p - e(c_+ - c_-)\nabla \Psi; \qquad \nabla \cdot \mathbf{u} = 0, \tag{1.48}$$

$$\mathbf{J}_\pm = -D\left(\nabla c_\pm \pm c_\pm \frac{e \nabla \Psi}{k_B T}\right) + c_\pm \mathbf{u}, \tag{1.49}$$

that will be accompanied by the appropriate boundary conditions for a given system.

1.3 SUMMARY AND OUTLOOK

The introductory chapter covered two main topics. As the systems studied in this thesis belong to the field of soft condensed matter, in the first part a general overview of SCM was provided. The applicability of SCM methods was discussed in terms of length and energy scales of the system of interest. This was followed by the demonstration of statistical mechanics methods as the main theoretical toolbox to describe and study SCM systems. By employing ensemble averages of physical quantities of interest, rather than having to track each individual constituent at every moment of time, it becomes significantly easier to study systems with statistically large amounts of constituent elements/particles.

In the second part of the chapter the main object of study in this thesis, an electric double layer, was introduced. After covering its origins and providing a brief history of how its theory was being developed in the 20^{th} century, the governing equations needed to describe a simple equilibrium EDL mathematically were introduced in form of Poisson-Nernst-Planck non-linear coupled differential equations. In the following section the theory was extended to the non-equilibrium EDL. The governing set of equations was updated to the dynamic Poisson-Nernst-Planck-Stokes system of equations, with Stokes equation describing the fluid flow.

This lays the foundation for the thesis, where systems with non-equilibrium EDLs will be the central topic of study, thus, relying on the information provided in this chapter.

The thesis is structured as follows. Chapter 2 covers the emergence of Asymmetric Rectified Electric Fields (AREF) in an electrolytic cell consisting of an asymmetric electrolyte with unequal ionic diffusion coefficients confined between two blocking electrodes and driven by a harmonic voltage. Chapter 3 covers AREF in a similar system where the electrolyte is symmetric with equal ionic diffusion coefficients, however in this case it is driven by a sawtooth-like electric potential, opening possibilities for tuning AREF in experiments much more flexibly, compared to the original version. Chapter 4 covers the the emergence of a hysteresis voltammetry loop in a microfluidic conical channel when driven by AC voltage and pressure, where the latter allows for the tuning of the hysteresis. As described in more detail in the chapter, such devices can be used in various neuromorphic computing applications, making them very interesting to study. Each chapter has its own introduction and summary. At the end of the thesis there is a summary of the whole thesis both in English and Dutch, followed by the acknowledgements and bibliography.

2

ASYMMETRIC RECTIFIED ELECTRIC FIELDS: NONLINEARITIES AND EQUIVALENT CIRCUITS

ABSTRACT

Recent experiments [S. H. Hashemi et al., Physical Review Letters **121**, 185504 (2018)] have shown that a long-ranged steady electric field emerges when applying an oscillating voltage over an electrolyte with unequal mobilities of cations and anions confined between two planar blocking electrodes. To explain this effect we analyse full numerical calculations based on the Poisson-Nernst-Planck equations by means of analytically constructed equivalent electric circuits. Surprisingly, the resulting equivalent circuit has two capacitive elements, rather than one, which introduces a new timescale for electrolyte dynamics. We find a good qualitative agreement between the numerical results and our simple analytic model, which shows that the long-range steady electric field emerges from the different charging rates of cations and anions in the electric double layers.

2.1 INTRODUCTION

Studying the response of an aqueous electrolyte to an externally applied oscillating electric field is a very active research direction, as AC voltages can be used to achieve various goals in a wide range of practical applications in electrolytes. For example, an AC voltage can be used to drive electrokinetic pumps [35, 36], induce fluid flow within microfluidic systems [37–40], manipulate charged colloids in aqueous electrolytes [41–43], desalinate and de-ionize the electrolyte using porous membranes [44–46], study the electrolyte dynamics with impedance and dielectric spectroscopy [41, 47–51], render memristive properties to aqueous electrolytes in confinement [52–54], and study bioparticles [55, 56]. For various applications, one of the key motivations to use AC electric fields over DC fields is to eliminate any net current or net charge in the system due to the vanishing field when averaged over a period. Here we will see, however, that the period-averaged current and charge do not necessarily vanish.

The simplest geometry allowing the study of the basic physical effects in an electrolyte under the influence of AC fields consists of a globally neutral 1:1 electrolyte of point-like ions confined between two blocking electrodes, to which an AC voltage is applied. It is well known that in equilibrium or at low frequencies a so-called Electric Double Layer (EDL) arises at the interface between a charged solid (electrode, colloid, etc.) and an electrolyte. The EDL consists of the surface charges of the solid and an oppositely charged diffuse ionic cloud with an excess of counter-ions and a depletion of co-ions [57]. The EDL has a characteristic thickness equal to the Debye length λ_D of the order of 10 nm when the salt concentration in water is around 1 mM at room temperature.

The behavior of the EDLs in this seemingly simple system can be described by Poisson-Nernst-Planck (PNP) equations, which take the Coulomb interactions into account as well as the diffusive and conductive properties of ions dissolved in water, viewed as a dielectric continuum. In this planar geometry the PNP equations form a system of coupled non-linear partial differential equations, that has been solved analytically only perturbatively [58, 59] or in terms of special functions [60]. Due to this, a large number of studies has concentrated on the quasi-equilibrium approach and weak driving electric

potentials [61–63]. In recent years, however, more studies have considered AC potentials whose amplitude Ψ_0 is well into the non-linear screening regime $\Psi_0 \gtrsim \beta^{-1}e \approx 25\text{mV}$, where e is the elementary charge and β^{-1} the product of the Boltzmann constant and room temperature. Thorough reviews of the response of an electrolytic cell to large applied DC and AC signals have been presented in Refs. [64, 65]. The most notable effect appearing at these high voltages is the presence of higher-order modes of the ion movement from the pattern of the driving potential - e.g. a sinusoidal driving voltage does not translate into (possibly phase shifted) sinusoidal ionic fluxes in the electrolyte anymore, because higher-order harmonics appear.

The inspiration to study non-linear effects in systems driven by an AC electric field has also come from experimental studies such as those in Refs. [41, 42]. The authors considered a vertical system consisting of an aqueous electrolyte confined between two horizontal blocking electrodes. The electrolyte contained charged colloids that tend to sediment in the gravitational field. However, it was observed that under the influence of a sufficiently strong harmonic AC voltage applied between the electrodes, a fraction of colloidal particles would float in the gravitational field rather than sediment to the bottom electrode [66]. A similar method to employ an AC voltage to generate non-zero steady effects has also been used in Ref. [67] to reverse the flow of AC electroosmosis. The physical mechanisms behind these effects remain somewhat unclear.

Observations such as the floating colloids and flow reversal mentioned above led to an investigation whether the ionic response to an AC driving voltage applied to the horizontal electrode could affect the ability of colloids to counteract the gravitational force [66]. This study used the aforementioned electrolytic cell model with blocking electrodes. It was discovered that ions with unequal diffusion coefficients in an electrolytic cell driven by a harmonic external potential can produce non-zero time-averaged electric fields that extend from the electrodes well into the bulk of the electrolyte. This phenomenon was called Asymmetric Rectified Electric Field (AREF) [66]. Besides this effect being interesting on its own, it was also suggested that the electric force exerted by this field could be responsible for keeping the charged colloids afloat in a gravitational field in the experiments of Ref. [41]. Therefore the AREF was investigated in more detail in follow-up

papers concerned with the dependence on several system parameters [68] and with perturbative solutions of the governing system of non-linear differential equations [58], the latter even replicating the main characteristics of the AREF structure analytically. Interestingly, however, the physical mechanism responsible for AREF generation has not been discussed in any detail, except perhaps for a toy model proposed in Ref.[68] that we will briefly discuss at the very end of this study. It is also interesting to note that a recent study regarding floating colloids under AC voltage in an electrolytic cell [69] suggested that besides AREF, dielectrophoresis can also counter the gravitational force depending on the parameters of the system. It is, however, still not clear to what extent each of these two mechanisms is contributing to the floating height of the colloids [69].

In this chapter we focus on AREF and numerically solve the PNP equations and also construct an analytical expression based on an equivalent RC circuit, modified, however, to take nonlinearities into account. This captures the behavior of the AREF qualitatively, helping us to identify the core physical mechanism responsible for the effect by reducing it to simple charging-discharging processes of capacitors. The structure of this chapter is as follows. In section 2.2 we introduce the system of interest together with the PNP equations that govern the processes in the electrolytic cell. In section 2.3 we describe and give an explanation of the AREF effect for a particular set of system parameters, essentially reproducing, confirming, and reformulating some earlier results. In section 2.4 we numerically study how the AREF depends on the main system parameters. Then, in section 2.5 we solve the PNP equations to identify the equivalent circuit corresponding to the electrolytic cell and use it to construct an analytic toy model in section 2.6 that compares quite favourably to the numerical solutions of the PNP equations. Finally, in section 2.7 we conclude and discuss our results.

2.2 POISSON-NERNST-PLANCK EQUATIONS

The system of interest consists of a 3D aqueous electrolyte of relative dielectric constant ε at room temperature confined between two parallel macroscopic planar electrodes at a distance L from each other, where we assume translational invariance in the lateral directions. The electrolyte

consists of two types of monovalent point-like ions: cations $(+)$ and anions $(-)$ characterized by valencies $z_\pm = \pm 1$ and diffusion coefficients $D_\pm$. The total number of cations and anions is equal, hence the total system is electroneutral. The electrodes are blocking, so that no ion can leave the electrolyte and we exclude any chemical REDOX reactions. The system is driven by an AC voltage $\Psi(t) = \Psi_0 e^{i\omega t}$ applied to the left electrode placed in the plane $z = -\frac{L}{2}$, whereas the right one, placed at $z = \frac{L}{2}$, is kept grounded. Here ω is the imposed angular frequency and Ψ_0 the amplitude. A schematic representation of the system is shown in Fig. 2.1.

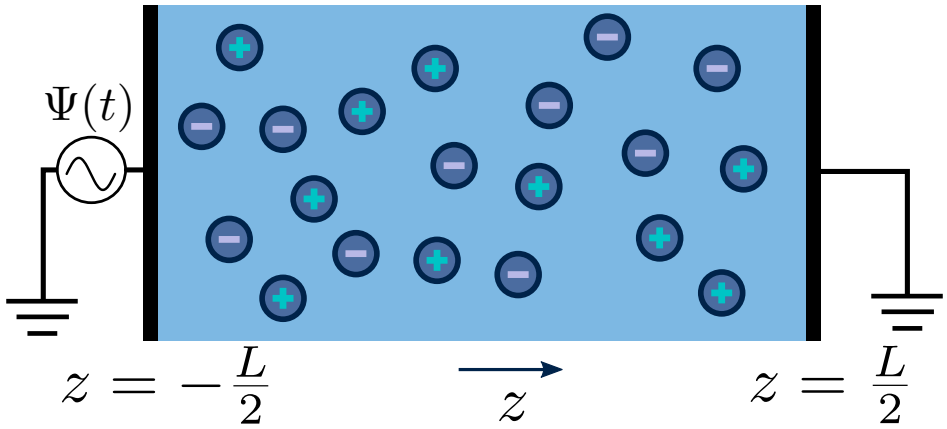

Figure 2.1: Schematic representation of the aqueous 1:1 electrolyte of interest containing a continuum solvent and two ionic species confined between two parallel blocking electrodes separated by a distance L. The electrolyte is driven by a time-dependent electric potential $\Psi(t)$ applied to the electrode at $z = -\frac{L}{2}$, while the other one at $z = \frac{L}{2}$ is kept grounded.

We use the Poisson-Nernst-Planck (PNP) equations to study the system. The first is the Poisson equation, which relates the local electric potential

profile $\Psi(z,t)$ to the local charge density $e\Big(c_+(z,t)-c_-(z,t)\Big)$, where $c_\pm(z,t)$ denotes the concentration of cations $(+)$ and anions $(-)$ at position z and time t. For $|z|<\frac{L}{2}$ the Poisson equation reads

$$\frac{\partial^2\Psi(z,t)}{\partial z^2}=-\frac{e}{\varepsilon_0\varepsilon}\Big(c_+(z,t)-c_-(z,t)\Big), \tag{2.1}$$

where ε_0 is the permittivity of vacuum and $\varepsilon=80$ represents water as a structureless continuum. The ionic fluxes $J_\pm(z,t)$ contain a diffusive contribution due to the gradients of ion concentrations and a conductive contribution due to the potential gradient, jointly described by the Nernst-Planck equation

$$J_\pm(z,t)=-D_\pm\left(\frac{\partial c_\pm(z,t)}{\partial z}\pm\beta e c_\pm(z,t)\frac{\partial\Psi(z,t)}{\partial z}\right), \tag{2.2}$$

where we consider the diffusion coefficients to be spatially constant and different for cations (D_+) and anions (D_-). Because we exclude any chemical reaction in the system, the concentrations and fluxes are coupled by the continuity equation

$$\frac{\partial c_\pm(z,t)}{\partial t}+\frac{\partial J_\pm(z,t)}{\partial z}=0. \tag{2.3}$$

The PNP equations (2.1), (2.2) and (2.3) form a closed set for the concentrations $c_\pm$, the fluxes $J_\pm$ and the potential Ψ. Solving PNP equations explicitly requires boundary and initial conditions, which we write as

$$\Psi(-L/2,t)=\Psi_0 e^{i\omega t}, \tag{2.4}$$

$$\Psi(L/2,t)=0, \tag{2.5}$$

$$J_\pm(-L/2,t)=J_\pm(L/2,t)=0, \tag{2.6}$$

$$c_\pm(z,t=0)=c_s, \tag{2.7}$$

where c_s is the fixed initial average salt concentration, that is equal for both ionic species in our symmetric $1:1$ electrolyte. Due to Eq. (2.3) combined

with boundary conditions Eq. (2.6) the number of cations and anions will be conserved such that

$$\frac{1}{L}\int_{-L/2}^{L/2} c_{\pm}(z,t)\,dz = c_s. \tag{2.8}$$

Here we note that for convenience during derivations below we use a complex representation of physical quantities (like for the voltage in Eq. (2.4)), however, in numerical calculations we use $\sin(\omega t)$ to drive the system (ensuring that the system starts from equilibrium with $\Psi(z,0) = 0$), therefore the physical quantities will correspond to the imaginary part of derived complex expressions. For given Ψ_0, $D_{\pm}$, ω and c_s, Eqs. (2.1) – (2.8) complete the system of non-linear coupled differential equations. We solve these equations numerically employing COMSOL® as a finite-element method solver software.

Convenient insight into relevant system parameters can be obtained as follows. In static equilibrium, so for $\omega = 0$, the applied potential $\Psi(-L/2,t) = \Psi_0$ (a constant), and $J_{\pm}(z,t) = 0$, and in the linear regime with $|\beta e\Psi_0| \lesssim 1$, the EDLs get fully developed at the two electrodes and the NP equation (2.2) can be integrated to obtain the Boltzmann distribution

$$c_{\pm}(z) = c_s'\left(1 \mp \frac{\Psi_0\beta e\sinh(\kappa z)}{2\sinh(\kappa L/2)}\right), \tag{2.9}$$

with κ^{-1} the characteristic Debye length of the equilibrium EDL given by

$$\kappa^{-1} = \sqrt{\frac{\varepsilon\varepsilon_0}{2e^2\beta c_s'}} \equiv \lambda_D. \tag{2.10}$$

The concentration c_s' is an integration constant that is very close to c_s in the large L-limit of interest here, so throughout the chapter we set $c_s' = c_s$ in the definition of λ_D. In this limit, as we will derive below, the characteristic timescale of EDL formation [65, 70] is written as the RC time

$$\tau_{RC} = \frac{L\lambda_D}{2D} = \frac{L}{2\kappa D}. \tag{2.11}$$

For future convenience we also define the Debye time

$$\tau_D = \frac{1}{\kappa^2 D} = \tau_{RC}\frac{2}{\kappa L}, \tag{2.12}$$

during which the ions diffuse over a distance of the order of the Debye length [65, 71]. Here the effective diffusion coefficient of the ions in the electrolyte is given by

$$D = \frac{2D_+D_-}{D_+ + D_-}. \tag{2.13}$$

For later reference it proves convenient to keep D fixed and to characterise the asymmetry of D_+ and D_- by

$$\delta \equiv \frac{D_-}{D_+}, \tag{2.14}$$

such that

$$D_\pm = \frac{D}{2}(1 + \delta^{\mp 1}). \tag{2.15}$$

Clearly, for equal diffusivities we have $D = D_+ = D_-$, however, for extremely asymmetric diffusivities the effective diffusion coefficient is essentially twice the smallest one.

For a few typical 1:1 electrolytes the asymmetry parameter δ is given in Table 1. Although close-to-symmetric electrolytes with $\delta \simeq 1$ exist according to the table, others have some degree of mobility asymmetry up to $\delta \simeq 2$ in the present examples. For simplicity we restrict attention to monovalent ions here, however we note that the mobility asymmetry of multivalent ions can be larger, for instance $BeCl_2$ has $\delta = 3.44$. Without loss of generality we choose $\delta > 1$ throughout this study, such that the negative ions will be the faster ones, thus $D_- > D_+$.

2.3 ASYMMETRIC RECTIFIED ELECTRIC FIELD (AREF)

2.3.1 *AREF Description*

According to Ref.[66], a mobility mismatch of ions, $\delta \neq 1$, can introduce a long-range steady electric field upon AC driving. This also follows from our numerical results. For convenience we define a standard parameter set including an amplitude and frequency of the driving potential given by $\beta e\Psi_0 = 3$ and $\omega\tau_{RC} = 1$, respectively. The standard system size is characterized by $\kappa L = 50$, and the standard diffusion coefficients are $D_+ =$

Salt	Ions	D_+	D_-	δ
CsCl	Cs^+, Cl^-	2.06	2.03	0.99
CsI	Cs^+, I^-	2.06	2.05	1.00
KCl	K^+, Cl^-	1.96	2.03	1.03
NaCl	Na^+, Cl^-	1.33	2.03	1.53
LiI	Li^+, I^-	1.03	2.05	1.99
		$\times 10^{-9}\mathrm{m}^2/\mathrm{s}$		

Table 1: Ionic mobility ratio $\delta = D_-/D_+$ for various common aqueous 1:1 electrolytes [72].

$D_-/\delta = 1.09 \cdot 10^{-9}\mathrm{m}^2/\mathrm{s}$ (resulting in $D = 1.456 \cdot 10^{-9}\mathrm{m}^2/\mathrm{s}$) with $\delta = 2$ by default. The bulk concentration of ions is $c_s = 1\mathrm{mM}$, resulting in a Debye length $\lambda_D = 10^{-8}\mathrm{m}$. Any deviation from this set will be explicitly stated. The coordinate z is measured in terms of Debye length $\lambda_D = \kappa^{-1}$ and ranges from $-L/2$ to $L/2$. Our standard focus is also on the late-time limit-cycle when all transients have decayed such that all time-dependence has the same period as that of the driving potential, potentially, however, with higher-order harmonics.

In Fig. 2.2 we plot for the standard parameter set, with asymmetries $\delta = 1, 2$ and 3.5, the late-time period-averaged position-dependent profiles of (a) the dimensionless charge distribution $\langle c_+ - c_- \rangle(z)$, (b) the electric field $\langle E \rangle(z)$, and (c) the potential $\langle \Psi \rangle(z)$. Here time-averaging is defined by

$$\langle f \rangle(z) = \frac{1}{T} \int_{t_0}^{t_0+T} f(z,t)\, dt, \tag{2.16}$$

where t_0 is the (sufficiently late) time at which we start averaging, $T = \frac{2\pi}{\omega}$ is the period of AC voltage, and f can be any of the functions that we are considering - either the electric field E, the electric potential Ψ, or a combination of the ion concentrations $c_\pm$.

For $\omega > 0$, so for finite T, Fig. 2.2 shows for symmetric electrolytes ($\delta = 1$) that $\langle c_+ - c_- \rangle = \langle \Psi \rangle = \langle E \rangle = 0$, meaning that charges are distributed evenly across the system, as expected. However, if the ionic mobilities become mismatched ($\delta = 2$ and $\delta = 3.5$), the average charge distribution $\langle c_+ - c_- \rangle$ becomes spatially non-uniform (see Fig. 2.2(a)), which, in turn, gives rise to a non-zero time-averaged electric field and a steady non-uniform electric potential, presented in Fig. 2.2(b) and Fig. 2.2(c), respectively. We note in Fig. 2.2(c) that the time-averaged electrode potential is zero by construction, as imposed by the boundary conditions. Nevertheless, the steady electric field extends several Debye lengths into the electrolyte (in the current case it is more than $5\lambda_D$, however this can be even more, as demonstrated in Ref.[68]). Fig. 2.2 gives a first clue of the underlying physics, as we see that $\langle c_+ - c_- \rangle$ is negative in the vicinity of the surfaces and positive a few Debye lengths away, showing that the faster anions manage to approach the electrode in larger quantities, on average, than the slower cations.

Fig. 2.2(b) shows an example of the long-range steady electric field that is referred to as Asymmetric Rectified Electric Field (AREF) in Ref.[66]. Parametric studies of AREF performed in Ref.[68] concentrate on two characteristics of AREF - the position and the height of the largest peak of the concentration profile of the slower ions. Instead, here we use the spatio-temporal average U of the (dimensionless) electric potential profile to characterize the magnitude of AREF,

$$U \equiv \beta e \frac{1}{L} \int_{-\frac{L}{2}}^{\frac{L}{2}} dz \langle \Psi \rangle(z), \tag{2.17}$$

which is a convenient integrated quantity to study numerically. Moreover, for large L, the dimensionless quantity U is a measure for the time-averaged electroosmotic (EO) mobility [73], as it plays the same role as the zeta potential of charged surfaces; it is proportional to the physically measurable EO mobility μ_{EO}. However, EO is not the focus of the current chapter and can be explored in future studies. Finally, it is also interesting to note that the period-averaged surface charge density on the electrodes, $\langle \sigma \rangle \propto \langle E|_{z=-L/2} \rangle$ vanishes by Gauss law due to the electric neutrality of the system. This is also clear from Fig. 2.2(b), where the curves of $\langle E \rangle$ approach zero at $z = \pm L/2$. Thus the layers of fast anions that we see at each of the electrodes in Fig. 2.2(a)

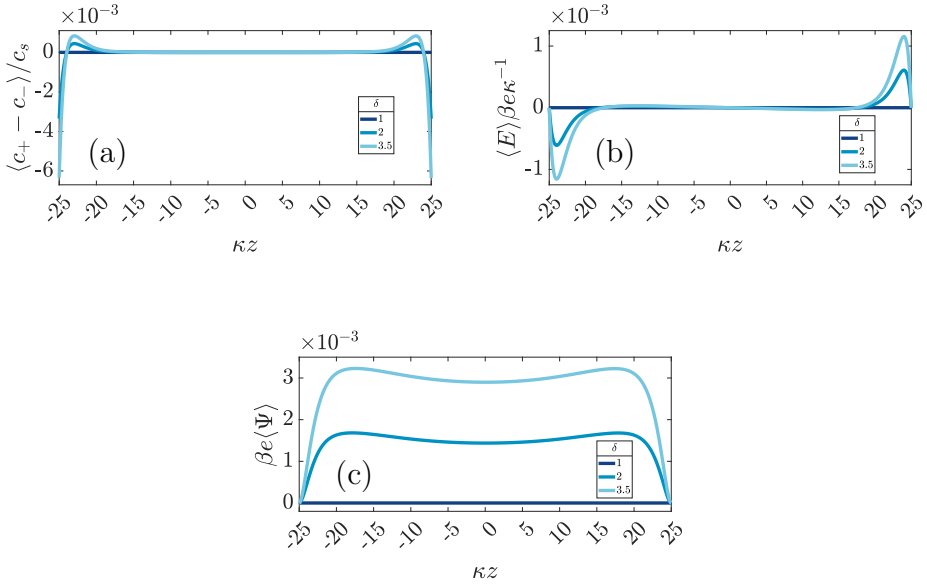

Figure 2.2: Dimensionless spatial profiles of the time-averaged (a) ionic charge density $\langle c_+ - c_- \rangle / c_s$, (b) electric field $\beta e \kappa^{-1} \langle E \rangle$, and (c) electric potential $\beta e \langle \Psi \rangle$ for an aqueous 1:1 electrolyte with Debye length $\lambda_D = 10$nm confined between two planar electrodes at distance $L = 50\lambda_D$. The electrode at $z = L/2$ is grounded, the one at $z = -L/2$ has an AC potential $\Psi_0 e^{i\omega t}$ with amplitude $\Psi_0 = 3/\beta e = 75$ mV and frequency $\omega = \tau_{RC}^{-1}$ with RC-time τ_{RC} given by Eq. (2.11). The different colors represent the three different mobility ratios $\delta = D_- / D_+$ of the faster anions and the slower cations.

essentially play the role of charged electrodes that are screened by the cloud of slow cations.

2.3.2 *AREF Mechanism*

Here we discuss the mechanism for AREF generation. It is perhaps best understood by tracking the number of ions gathering at one of the electrodes

(e.g. the one at $z = -L/2$) for the whole period $T = 2\pi/\omega$. In the electrolytic cell that we are considering with the driving voltage given by Eq. (2.4), in the first half of the period $T/2$ the negative (faster) ions will gather at the chosen electrode because it is positive, whereas in the second half the positive (slower) ones will tend to get closer. If the frequency of the voltage is such that the EDLs have enough time to develop (but not fully form) during the $T/2$ time span, the faster ions will manage to gather at the electrode in larger amounts. Therefore, if we average the number of ions at the electrode over the whole period T, we will get an excess of faster ions at the electrode. Exactly the same thing occurs at the opposite electrode, however with a $T/2$ shift in phase. This is what we also observe in Fig. 2.2(a), where the negative (faster) ions are accumulating at both electrodes on average in time. Moreover, due to the global electroneutrality of the cell, the surface charge on both electrodes is zero on average, such that the excess of the negative ions at both electrodes is screened by the excess of the oppositely charged ions located several Debye lengths away from the electrodes for the current parameters, as seen in Fig. 2.2(a).

2.4 PARAMETER DEPENDENCE OF AREF

In this section we study the dependence of the numerically obtained AREF magnitude U on the main system parameters.

2.4.1 *Applied Voltage Amplitude*

We start by studying the dependence of the space- and time-averaged potential U as defined in Eq. (2.17) on the amplitude Ψ_0 of the externally applied AC potential. The range that we consider for the driving voltage amplitude Ψ_0 is limited from above by our point ion approximation, which for $c_s = 1\text{mM}$ can become unrealistic due to strong ion crowding effects at the electrodes [74–76]. This occurs beyond $\beta e\Psi_0 \approx 8$, which is therefore the upper limit that we consider.

Fig. 2.3 shows the dependence of U on Ψ_0 for various driving frequencies for our standard parameter set. For the full range of frequencies $\omega\tau_{RC} \in [0.1, 10]$

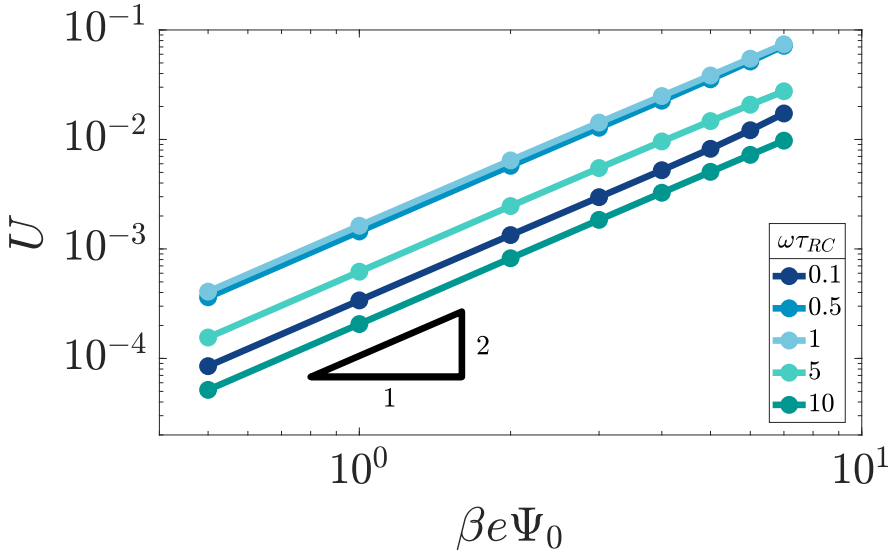

Figure 2.3: Double-logarithmic representation of the period- and space-averaged dimensionless potential U of Eq. (2.17) as a function of the driving voltage amplitude for varying driving frequencies ω at our standard parameter set (see text). The quadratic scaling $U \sim \Psi_0^2$ demonstrates that AREF is a non-linear effect.

that we consider here, the slope of the double-logarithmic curves is essentially identical to 2, i.e. $U \sim \Psi_0^2$ for all frequencies considered, which is in line with the findings of Ref.[68]. It should be noted, however, as was also demonstrated in Ref.[68], that the AREF scaling deviates somewhat from Ψ_0^2 at even higher voltage amplitudes $\Psi_0 > 10$. This voltage range leads, at least at low frequencies, to high ionic concentrations outside the regime of applicability of the underlying point-ion model. For this reason we leave this high-voltage regime out of the discussion in the current chapter. In the regime of interest the scaling confirms that AREF is a non-linear screening effect and motivates the study of its dependence on frequency, mobility asymmetry, and system size in terms of the scaled form $U/(\beta e \Psi_0)^2$ below.

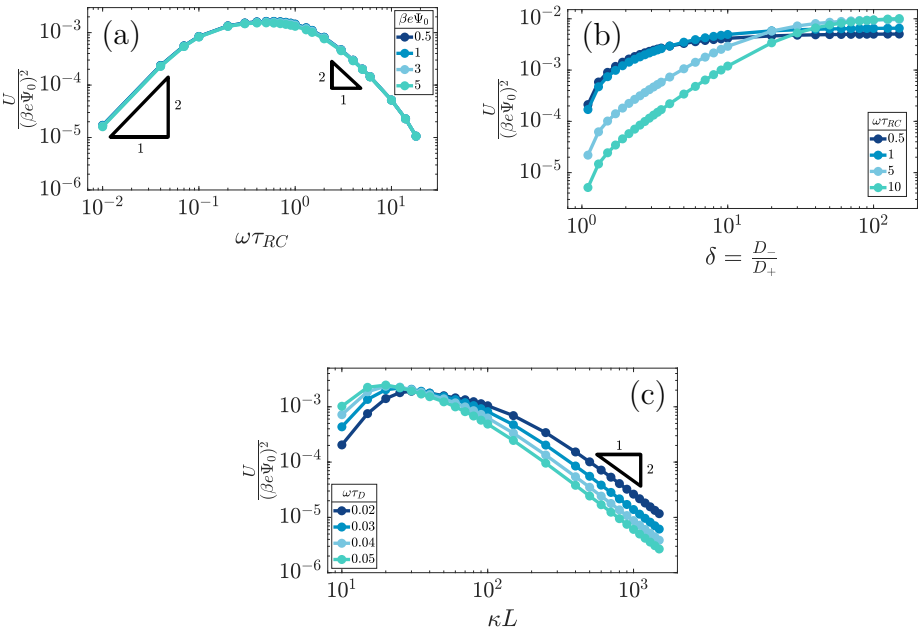

Figure 2.4: Dimensionless and scaled period-averaged potential $U/(\beta e\Psi_0)^2$ as obtained from numerical late-time solutions of the PNP equations for the standard parameter set (see text), in (a) as a function of the dimensionless frequency $\omega\tau_{RC}$, in (b) as a function of the the mobility asymmetry $\delta = D_-/D_+$, and in (c) as a function of the dimensionless system size κL, in all three cases in a double-logarithmic representation. In (a) we see a collapse of the curves for several voltage amplitudes Ψ_0. In (b) and (c) we consider several dimensionless frequencies $\omega\tau_{RC}$ and $\omega\tau_D$, respectively.

2.4.2 *Frequency*

Fig. 2.3 already showed that U is relatively large at $\omega\tau_{RC} \approx 1$ and considerably smaller at $\omega\tau_{RC} = 0.1$ and 10. Here we study for several Ψ_0 the frequency-dependence of U as obtained from the numerical solutions of the PNP equations in full detail for our standard parameter set. Fig. 2.4(a)

shows $U/(\beta e\Psi_0)^2$ as a function of $\omega\tau_{RC}$, featuring the expected collapse for all Ψ_0, a broad maximum at $\omega\tau_{RC} \sim 1$, and an algebraic decay $\sim \omega^2$ for small frequencies ω. For frequencies ω in the $\omega\tau_{RC} \sim 1-10$ range, the curve shows an algebraic $\sim \omega^{-2}$ decay, however, as the frequency ω gets increased further, the slope of the curve becomes steeper (stronger decay) due to an overscreening effect that starts to appear at the electrodes in this regime.

Qualitatively this frequency dependence can be explained by the mechanism that we proposed above. In the low-frequency limit, the system is nearly static and during the time span $T/2$ both ion species have enough time to essentially fully build up an EDL at the corresponding electrodes. Thus the number of ions in this fully developed EDL is the same for both half periods, the average ionic charge and thus the potential at the electrodes in the timespan T approaches zero, which agrees with the low-frequency part of the curve in Fig. 2.4(a). In the high-frequency limit, on the other hand, none of the ion species, not even the faster ones, has enough time to develop the EDLs. Therefore no net accumulation of charge occurs at the electrodes, yielding a decaying trend for U as the frequency increases. The maximum of the effect is reached for intermediate frequencies of the order of the characteristic RC time for EDL formation $\omega\tau_{RC} \sim 1$. At these frequencies the difference between the number of fast and slow ions gathering at the electrodes in the $T/2$ timespan is largest.

2.4.3 *Ion Mobility Asymmetry*

The asymmetry of ion mobility, $\delta \neq 1$, is the main cause of AREF and here we study how U depends on δ at fixed effective diffusion coefficient D -such that τ_{RC} remains fixed if we vary δ for fixed L and λ_D. For our standard parameter set Fig. 2.4(b) shows the δ-dependence of $U/(\beta e\Psi_0)^2$ for several driving frequencies $\omega\tau_{RC}$. Here we extend the interval for $\delta \in [1, 100]$ far beyond the typical range for small ions to identify that apart from the common monotonic increase of U with δ the curves are highly non-universal, with a frequency-dependent asymptotic saturation of U at high δ that is larger for higher frequencies whereas U is smaller for higher frequencies in the low-δ regime, with a crossover at $\delta \simeq 20-30$.

These results can qualitatively be explained within the scope of our proposed mechanism, where the large-δ limit proves helpful. Let us consider a (late-time) period $[t_0, t_0 + T]$ and divide it into two half periods in which the potential of the electrode at $z = -L/2$ is positive for $t \in [t_0, t_0 + T/2] \equiv t_+$ and negative for the complementary interval $t \in [t_0 + T/2, t_0 + T] \equiv t_-$. Introducing the maximum of the (absolute) areal ionic charge on this electrode during either of these periods as

$$\Gamma_\pm = \max_{t \in t_\pm} \left\{ \int_{-L/2}^{0} \mathrm{d}z \Big(|c_+(z,t) - c_-(z,t)| \Big) \right\}, \tag{2.18}$$

we expect, for $\delta > 1$, that $\Gamma_- > \Gamma_+$ since the faster anions can accumulate faster in $z \in [-L/2, 0]$ during t_- than the slower cations can during t_+ (for simplicity we ignore the fact that the faster anions also deplete faster than the slower cations, as depletion has a weaker contribution to the competition of number of ions present at the electrode compared to the accumulation).

Now let us assess how δ affects the charge accumulation process. From Eq. (2.15) we see for increasing δ at fixed D that cations will asymptotically settle at a fixed diffusion coefficient $\lim_{\delta \to \infty} D_+ \to D/2$ while the anions become increasingly mobile. At finite frequency, their finite mobility sets a limit for the amount of accumulation or depletion of cations at the electrode. For anions, despite the fact that their diffusion coefficient becomes increasingly faster, the equilibrium EDL configuration still imposes a limit to the anion concentration close to the electrode. Taking this into account, it becomes clear that $\lim_{\delta \to \infty} U \propto \Gamma_- - \Gamma_+ \to \text{const}$, which is exactly what we see in Fig. 2.4(b).

To explain the different saturation values of U in Fig. 2.4(b), we notice that at the low (realistic) values of δ the value of U follows the logic of the $U(\omega)$ curves - the maximum is achieved at around $\omega \tau_{RC} \sim 1$. However, as we increase δ, the hierarchy of the curves changes and in the $\delta \to \infty$ limit $U(\delta)$ reaches higher values for higher frequencies ω. The number of charges contained in a fully developed EDL only depends on the thermodynamic properties of the electrolytic cell together with the magnitude of the applied voltage, therefore, in the $\delta \to \infty$ limit anions will fully form an EDL irrespective of the (finite) voltage frequency ω. However, the concentration of cations gathered at the electrode decreases with the frequency ω (as the

higher the frequency ω, the less time there is for ions to gather), therefore the saturation value of U, proportional to the difference in the number of anions and cations gathered at the electrode, will increase with frequency, which is again exactly what we observe in Fig. 2.4(b).

2.4.4 *System Size*

In Fig. 2.4(c) we plot $U/(\beta e\Psi_0)^2$ as a function of the system size L (in units of the Debye length) for our standard parameter set at a number of dimensionless frequencies $\omega\tau_D$. Up to this point we used the dimensionless combination $\omega\tau_{RC}$ of Eq. (2.12) to characterize the frequency of the AC voltage, which, however, is not convenient here since τ_{RC} itself depends on the system size, according to Eq. (2.11). For the system sizes $\kappa L \in [10, 10^3]$ that we consider here, we see that U peaks at larger κL for lower frequencies $\omega\tau_D$, which corresponds in fact to a peak in the regime where $\omega\tau_{RC} \sim 1$, consistent with our earlier findings in Fig. 2.4(b). For $\kappa L \gg 10^2$ we observe an algebraic decay $U \propto L^{-2}$, the exponent of which resembles that of the decay $U \propto \omega^{-2}$ that we found in Fig. 2.4(a). This similar decay is not surprising since the key dimensionless parameter $\omega\tau_{RC}$ is linear in both L and ω. However, as we will see in section 2.6.2, the reason for this quadratic algebraic decay $U \propto L^{-2}$ is a bit more subtle than it seems here.

2.5 EQUIVALENT CIRCUIT FROM LINEARIZED PNP EQUATIONS

An alternative way of studying the system of interest involves the construction of an equivalent RC circuit, rather than relying solely on the numerical calculations [50, 77–80]. This convenient strategy of studying electro-chemical systems has been employed in this field for many years; for a historical overview on this matter we refer the reader to Ref.[81]. In the present case we first construct an equivalent RC circuit corresponding to the electrolytic cell in Fig. 2.1 in the linear regime for which $\Psi_0 \ll 1/\beta e$ -we will modify this model later to account for the intrinsically nonlinear character of AREF. In the linear regime, a widely used scheme is a simple RC circuit

with R and C elements connected in series [64, 65, 82]. However, as we will now show, it is not entirely accurate at high frequencies where $\omega\tau_{RC} > 1$.

In order to determine an equivalent circuit for our model we study its frequency response using the electrical impedance defined as

$$Z(\omega) = \frac{\Psi_0 \exp(i\omega t)}{I(t)}, \tag{2.19}$$

where $I(t)$ is the current flowing through the external (electronic) system due to the applied potential over the electrodes. The current is the time derivative (indicated by a dot) of the charge $Q(t) = A\sigma(t)$ on the electrode at $z = -L/2$ and can be calculated from the time-dependent potential profile $\Psi(z,t)$ using Gauss' law as

$$I(t) = \dot{Q}(t) = -A\varepsilon_0\varepsilon \left.\frac{\partial\dot{\Psi}(z,t)}{\partial z}\right|_{z=-L/2}, \tag{2.20}$$

with A the surface area of the electrode. Within the linear regime the PNP equations and boundary conditions of Eqs. (2.1) – (2.8) are well known to be solvable analytically, resulting in

$$\Psi(z,t) = \frac{\Psi_0}{2}\left(1 - \frac{\sinh(kz) + i\omega\tau_D\cosh(k\frac{L}{2})\cdot kz}{\sinh(k\frac{L}{2}) + i\omega\tau_D\cosh(k\frac{L}{2})\cdot k\frac{L}{2}}\right)e^{i\omega t}, \tag{2.21}$$

where we define the complex wavenumber

$$k = \sqrt{\kappa^2 + \frac{i\omega}{D}}. \tag{2.22}$$

Here D is the effective diffusion coefficient introduced in Eq. (2.13).

Inserting Eq. (2.21) together with Eq. (2.20) into Eq. (2.19) and also assuming that the system is large, $L \gg \kappa^{-1}$, we obtain the explicit expression

$$Z(\omega) \approx R\frac{1 + i\omega\tau_{RC}\sqrt{1 + i\omega\tau_D}}{i\omega\tau_{RC}(1 + i\omega\tau_D)^{3/2}}, \tag{2.23}$$

where

$$R = \frac{L}{A}\cdot\frac{1}{\varepsilon\varepsilon_0 D\kappa^2} = \frac{L}{A}\cdot\frac{1}{2D\beta e^2 c_s} \tag{2.24}$$

is the resistance of the system and τ_{RC}, as defined in (2.11), the timescale characterizing the EDL formation process. Note that $Z(\omega)/R$ depends only on $\omega\tau_{RC}$ and $\tau_{RC}/\tau_D = \kappa L/2$.

There are several ways to plot the frequency dependence of the impedance [47]. We will use the so-called Argand complex plane diagrams for the complex impedance $Z(\omega) = Z'(\omega) + iZ''(\omega)$, as represented by a parametric (ω dependent) plot of $(Z'(\omega),-Z''(\omega))$. The Argand diagram will also be backed up with a Bode plot, describing how the impedance modulus $|Z(\omega)|$ depends on the frequency ω. The combination of Argand diagram together with a Bode plot often allows readily for an identification of a circuit, not only of the linear elements included in the circuit but also how they should be connected - either in series, parallel or combinations thereof. Usually the frequency response plots mentioned above are unique for relatively simple electric circuits [47]. Nonetheless, in order to ensure the robustness of the chosen equivalent circuit configuration, it is a commonly employed strategy to support its selection with physical considerations. This ensures that the circuit mimics the behavior of the system it represents, as detailed in Ref.[48]. An electric circuit that produces similar Argand and Bode curves while also possessing a configuration consistent with physical principles is denoted as the equivalent electric circuit associated with the electrolytic cell.

We plot, for $\kappa L = 500$, the Argand diagram of the dimensionless combination $Z(\omega)/R$ given by Eq. (2.23) in Fig. 2.5(a) and the corresponding Bode plot in Fig. 2.5(b), in both cases with dots at three characteristic frequencies. The Argand diagram features a vertical line at $Z' = R$ in the low-frequency limit, characteristic for a resistor R with a capacitor connected in series, and a semi-circle with a maximum of $-Z'' = R/2$ at $Z' = R/2$ for higher frequencies, characteristic for a parallel connection of a resistor R and a capacitor. The Bode plot gives us similar clues, allowing us to identify the electric response of the electrolytic cell with that of an equivalent circuit that consists of a capacitor C_2 in parallel with a resistor R and a capacitor C_1 in series, as illustrated in Fig. 2.7(a). The impedance $Z_c(\omega)$ corresponding to this circuit can easily be calculated and reads

$$Z_c(\omega) = \frac{i\omega C_1 R + 1}{i\omega\Big(C_1 + (i\omega C_1 R + 1)C_2\Big)}. \tag{2.25}$$

We note that the functional forms of Eqs. (2.23) and (2.25) are actually slightly different, however with a remarkable agreement for our regime of interest where $C_1 \gg C_2$, which translates into $\kappa L \gg 1$ as we will discuss in more detail below. In order to derive the expressions for the individual elements C_1, C_2 and R of the circuit, we match the impedances of the electrolytic cell and the circuit from Eqs. (2.23) and (2.25), respectively, by considering the high- and low-frequency limits $\omega\tau_{RC} \to \infty$ and $\omega\tau_D \to 0$, respectively. For R this yields the bulk resistance of the electrolyte given by Eq. (2.24) and for the capacitances we find

$$C_1 = \frac{A\varepsilon\varepsilon_0\kappa}{2}, \tag{2.26}$$

$$C_2 = \frac{A\varepsilon\varepsilon_0}{L}. \tag{2.27}$$

Physically C_1 corresponds to the net capacitance of the two fully developed EDLs in series, i.e. at both planar electrodes, each with the linear-screening capacitance $A\varepsilon\varepsilon_0\kappa$. Likewise, C_2 corresponds to the capacitance of a dielectric (water-filled) parallel-plate capacitor of size L without any ionic charge carriers (and hence without any EDL).

We remarked already that the functional form of the impedances of the cell and the effective circuit are not identical. Using the matching parameters for R, C_1, and C_2 determined above, we compare in Fig. 2.6 the Argand plots of the cell (solid lines) and the electric circuit of Fig. 2.7(a) (dashed lines), for system sizes $\kappa L = 30$, 100, and 1000. For all three system sizes the agreement is rather good for all frequencies, especially for high frequencies $\omega\tau_D \gg 1$ where EDLs can hardly develop. For the two smaller systems sizes deviations between the solid and dashed lines can be seen by eye at higher frequencies, however their distinction is beyond the resolution of the plot for $\kappa L = 1000$. This can be quantitatively appreciated by the inset of Fig. 2.6, where the maximum difference between unity and the ratios Z'/Z'_c and Z''/Z''_c, defined as $\Delta_{\mathrm{Re}}(L) = \max_\omega |Z'(\omega, L)/Z'_c(\omega, L) - 1|$ and $\Delta_{\mathrm{Im}}(L) = \max_\omega |Z''(\omega, L)/Z''_c(\omega, L) - 1|$ are plotted as a function of system size κL. Here we denote the real and imaginary parts of the circuit impedance from Eq. (2.25) by Z'_c and Z''_c, respectively. The inset of Fig. 2.6 clearly shows an increasing agreement between the two frequency responses with increasing

system size with differences decaying proportional to $(\kappa L)^{-1}$. Hence we can faithfully use the circuit in Fig. 2.7(a) to represent the electrolytic cell for $\kappa L \gg 1$.

Interestingly, the circuit of Fig. 2.7(b) can be shown to have an impedance of the exact same functional form as Eq. (2.25), however with modified elements $C_1' = C_1 + C_2$, $C_2' = C_2(C_1 + C_2)/C_1$, and $R' = RC_1^2/(C_1 + C_2)^2$. This implies that the capacitor ratio of the two circuits is the same, $C_2'/C_1' = C_2/C_1$, and also that $1/C_1' + 1/C_2' = 1/C_2$. Since the difference between the circuits becomes irrelevant in the limit $C_1 \gg C_2$ of our main interest, we focus on the circuit of Fig. 2.7(a) in the remainder of this work.

Let us return to the Argand diagram of Fig. 2.5(a), for which we already discussed the vertical line at sufficiently low frequencies, which implies that in this regime the equivalent circuit is the simple serial circuit shown in Fig. 2.7(c), with R and C_1 in series without the second capacitor C_2 in parallel. This simplified equivalent circuit has been used to model electric cells in many studies before [64, 65, 82, 83], however the presence of the semi-circle shows that the simplified circuit breaks down at high enough driving frequencies. Interestingly, the crossover between the semi-circle and the vertical line, i.e. the crossover regime for the (un)importance of C_2 in the equivalent circuit, does *not* occur at frequencies as high as $\omega \simeq 1/\tau_D$ *nor* at frequencies as low as $\omega \simeq 1/\tau_{RC}$, but rather at frequencies $\omega \simeq \tau_s^{-1}$ where we introduce the intermediate characteristic time scale

$$\tau_s = \sqrt{\tau_{RC}\tau_D} = \frac{\sqrt{\frac{1}{2}L\kappa^{-3}}}{D}, \tag{2.28}$$

where the label "s" stands for "series". The simplified series approximation shown in Fig. 2.7(c) only holds for $\omega \lesssim \tau_s^{-1}$. Physically, τ_s characterises the timescale at which the imaginary part of the impedance (i.e. the capacitive effects of the circuit) is minimized. This is clearly visible in Fig. 2.5(b), where the phase angle $\phi = \arctan \frac{-Z''(\omega)}{Z'(\omega)}$ is seen to exhibit a minimum for $\omega\tau_s \sim 1$.

We should note here though, that the presence of the additional τ_s and τ_D timescales does not influence the characteristic charging time of the full circuit and it matches that of an RC in series circuit. The reason for this is that we work with large systems $\kappa L \gg 1$ which translates into $C_1 \gg C_2$,

meaning that the total charging time will be dictated by how fast the C_1 capacitor is charged.

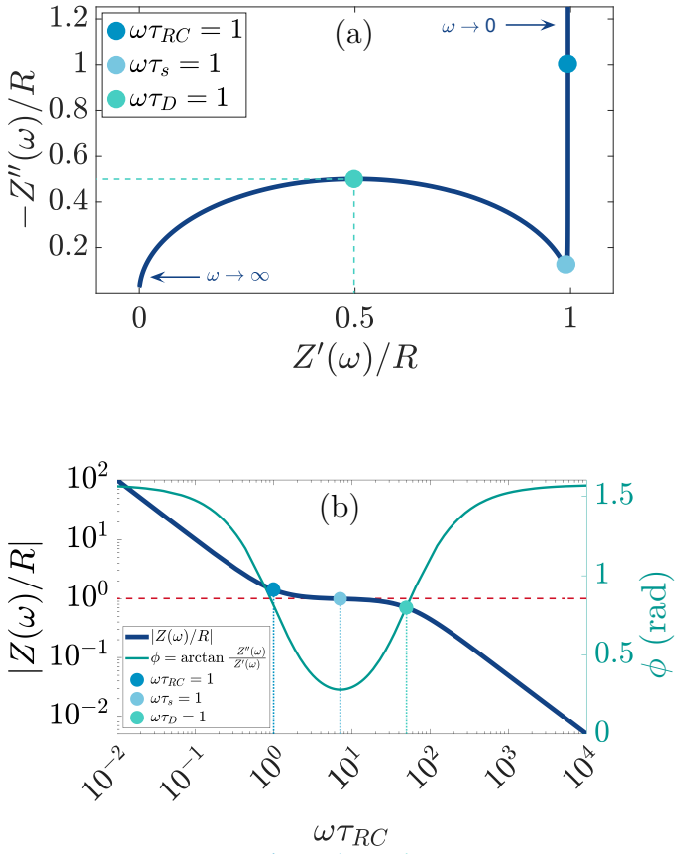

Figure 2.5: (a) Argand diagram and (b) Bode plot characterising the frequency-dependence of the complex impedance of an electrolytic cell given by Eq. (2.23), with system size $\kappa L = 500$ for our standard parameter set (see text). Characteristic frequencies corresponding to the (long) RC-time τ_{RC}, the (short) Debye time τ_D, and the (intermediate) time $\tau_s = \sqrt{\tau_{RC}\tau_D}$ (see text) are indicated with dots. The Bode plot also features the frequency dependence of the phase shift, showing a minimum at $\omega\tau_s = 1$.

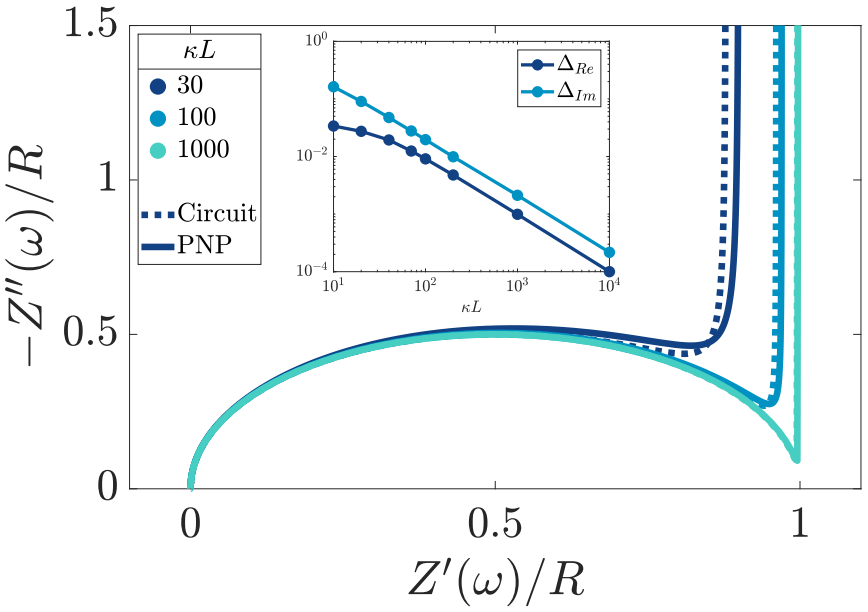

Figure 2.6: Argand diagrams for the complex impedance of the electrolytic cell (solid lines) and the equivalent circuit (dashed lines) for system sizes $\kappa L = 30, 100, 1000$ and our standard parameter set (see text). The inset shows the (small) maximum deviation of the ratios $Z'(\omega)/Z'_c(\omega)$ and $Z''(\omega)/Z''_c(\omega)$ from unity as a function of system size κL, indicative of the increasingly good agreement between PNP calculations of the cell and the equivalent circuit for larger system sizes.

2.6 TOY MODEL

2.6.1 *Modified linear circuit*

Even though the mechanism of the AREF allows for a qualitative understanding of the numerical results of section 2.4, a more quantitative explanation remains missing, for instance on the exponents characterising the algebraic decay of the time- and space-averaged potential U at high and low frequencies and the scaling with system size. For this reason we will now

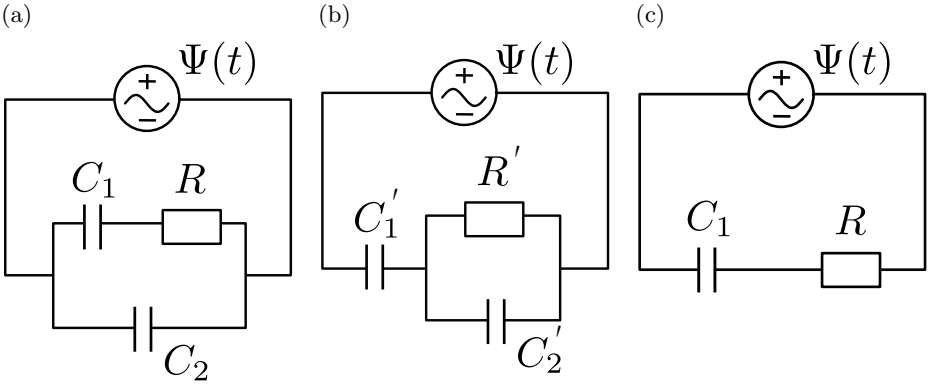

Figure 2.7: (a) Equivalent electric circuit corresponding to the electrolytic cell in the linear regime for large system sizes $L \gg \kappa^{-1}$. (b) Alternative version of the equivalent circuit with modified elements (see text). (c) Simplified equivalent electric circuit corresponding to the low-frequency case $\omega\tau_{RC} \ll \sqrt{\kappa L/2}$. Here R and C_2 correspond to the resistance and capacitance of the cell at infinite frequency, respectively, and C_1 is the total capacitance of two fully developed electric double layers at the electrodes, as described by Eqs. (2.24), (2.26), and (2.27).

construct a simplified model of the electrolytic cell based on the equivalent circuit of Fig. 2.7(a). This model will allow us to analytically calculate a proxy of U, namely the period-averaged charge gathered in the EDL. As we will see below, in the majority of cases this charge has a similar dependence on the system parameters as U.

Clearly, however, due to the linear nature of the equivalent circuit, some modifications are needed to account for the intrinsically non-linear nature of AREF. For the clarity of explanation, we start by exploiting the mirror symmetry of the geometry to concentrate only on the left half of the system $z \in [-L/2, 0]$, as the right half $z \in [0, L/2]$ will be in exact anti-phase. In our toy model we calibrate the time such that the electrode potential at $z = -L/2$ is positive during $t \in [0, T/2]$ and negative during $t \in [T/2, T]$, with $T = 2\pi/\omega$ the period. We assume that the EDL of the left electrode gets charged only by the fast anions in the first half of the period, while only the slow cations charge the same electrode in the second half of the period. This assumption significantly simplifies the treatment of the system, as it clearly separates the timescales of EDL charging/discharging processes by fast and slow ions, while allowing us to characterize the inherently non-linear charging process by combining two separate linear equivalent circuits albeit with different system parameters during the two half periods. Throughout we use the equivalent circuit of Fig. 2.7(a), however with two different ionic mobilities $D_\pm$, and hence two different resistances R_- for $t \in [0, T/2]$ and R_+ for $t \in [T/2, T]$, which in analogy to Eq. (2.24), are given by

$$R_\pm = \frac{L}{A\varepsilon\varepsilon_0 D_\pm \kappa^2}. \tag{2.29}$$

For $\Psi(t) = \Psi_0 e^{i\omega t}$, by employing Kirchhoff's equation and Laplace transformation, it is straightforward to calculate the total electric charge $Q_\pm(t)$

on the two capacitors C_1 and C_2 for each of the two equivalent circuits, and we find

$$Q_{\pm}(t) = \frac{\Psi_0}{1 + C_1^2 R_{\pm}^2 \omega^2} \times \left(\left(C_1 + C_2 + C_1^2 C_2 R_{\pm}^2 \omega^2 \right) \sin(\omega t) - C_1^2 R_{\pm} \omega \cos(\omega t) \right), \quad (2.30)$$

where we neglected all the transient terms, as we are interested in the limit-cycle solutions. Here we note that C_1 and C_2 are thermodynamic quantities that do not depend on the ionic transport properties such as diffusion coefficient; they are given in Eqs. (2.26) and (2.27) and are the same for both types of ions during each of the two half periods. For both sets of circuit parameters we can then calculate the average charge $\{Q_{\pm}\}$ on the capacitors in the interval $t \in [t_0, t_0 + T/2]$, yielding

$$\{Q_{\pm}\} = \frac{2}{T} \int_{t_0}^{t_0 + T/2} Q_{\pm}(t)\, dt. \quad (2.31)$$

We now chose t_0 such that $Q_{\pm}(t)$ is positive for $t \in [t_0, t_0 + T/2]$, which is always possible because $Q_{\pm}(t)$ of (2.30) is a harmonic function with the same frequency as the driving voltage. Inserting Eq. (2.30) into Eq. (2.31) yields

$$\{Q_{\pm}\} = Q_{Ref} \frac{\omega R_{\pm} C_1 \sqrt{1 + \frac{\left(C_1 + C_2 + \omega^2 R_{\pm}^2 C_1^2 C_2 \right)^2}{\omega^2 R_{\pm}^2 C_1^4}}}{\left(1 + \omega^2 R_{\pm}^2 C_1^2 \right)}, \quad (2.32)$$

with a convenient reference charge defined by $Q_{Ref} = (2/\pi) C_1 \Psi_0$ that is identical in the circuits and the two half-periods. Following our convention that $D_- > D_+$ we can then calculate the dimensionless period-averaged net charge

$$Q' = \frac{\{Q_-\} - \{Q_+\}}{Q_{Ref}}, \quad (2.33)$$

which is a measure for the time-averaged excess charge that is accumulated in a circuit with low resistance (corresponding to the fast anions charging an EDL at a positive electrode potential) compared to the circuit with a higher resistance (corresponding to the slower cations charging the EDL). Below we will consider Q' as a proxy for the space- and time-averaged potential U of Eq. (2.17). Interestingly, one checks that Q' only depends on three dimensionless parameters that can be represented by C_1/C_2, R_+/R_-, and $\frac{1}{2}\omega(R_+ + R_-)C_1$, which are equal to the system size κL, the mobility asymmetry δ, and $\omega\tau_{RC}$, respectively. These three parameters correspond exactly to three of the four parameters on which U depends, the fourth one being the amplitude of the driving potential $\beta e\Psi_0$. The disagreement between the nonlinear dependence $U \propto \Psi_0^2$ that we identified earlier and the independence of Q' on Ψ_0 is the price we pay for analysing the nonlinear AREF phenomenon in terms of linear-circuit theory. The dependence of Q' on κL, δ, and $\omega\tau_{RC}$ will, however, be quite similar to the dependence of U on these parameters, as we will discuss now.

2.6.2 *Parameter dependence of the proxy Q'*

In section IV we studied the dependence of U on several system parameters numerically, using a standard reference set. Here we study to what extent the analytical expression of Eq. (2.33) for the proxy Q' gives similar results, where we use the same standard parameter set.

First we study the frequency dependence. In Fig. 2.8(a) we plot Q' as a function of $\omega\tau_{RC}$, not only for the full RC-circuit of Fig. 2.8(b) but for comparison also for the simplified circuit of Fig. 2.7(c), for which $C_2 = 0$ as in an infinitely large system with $\kappa L \to \infty$. It is apparent that for low to medium frequencies $\omega \lesssim \tau_s^{-1}$, as indicated by the vertical dashed line, both curves are strikingly similar to each other and to the one for U in Fig. 2.4(a), as all three share a broad maximum at $\omega\tau_{RC} \sim 1$ and an algebraic decay $\propto \omega^2$ for small frequencies. However, at higher frequencies $\omega\tau_{RC} \gg 1$ Fig. 2.8(a) shows a remarkable difference between the simplified and the full circuit, the former showing a decay $Q' \propto \omega^{-1}$ and the latter a decay $Q' \propto \omega^{-2}$. This can be attributed to C_2 acting increasingly similar to a short circuit or a wire as we increase the frequency. Hence, the high-frequency

scaling of Q' of the full circuit is clearly closer to that of U, although the phenomenon of overscreening (that is obviously not included in the linear-circuit theory) causes deviations of the algebraic high-frequency scaling of U that is not included in Q'. Nevertheless, the overall agreement of the frequency dependence of U and Q' is comforting and supports our view of the underlying mechanism. From this point onward we will only use results based on the full circuit that includes both a finite C_1 and C_2.

Next we study the δ-dependence of Q' for exactly the same parameters as we used for U in Fig. 2.4(b), i.e. for our standard parameter set with a fixed τ_{RC}. The resulting Q' is plotted in Fig. 2.8(b) for $\delta \in [1, 100]$ for various driving frequencies $\omega\tau_{RC}$. As was the case for U, we see that Q' is monotonically growing with δ until an asymptotic large-δ limit that is larger for the higher frequencies than for the lower frequencies, which is the exact opposite of the ordering of Q' in the small-δ regime. Hence we see once again that our modified linear circuits can catch some of the essential features of AREF.

Finally, we study the system-size dependence of Q' by plotting it in Fig. 2.8(c) as a function of κL for several frequencies characterised by fixed $\omega\tau_D$, again for the same parameters as we used for U in Fig. 2.4(c). We can see that Q' peaks at system sizes that vary from $\kappa L \simeq 20$ at the highest frequency to $\kappa L \simeq 100$ at the lowest frequency, which corresponds, for every frequency considered, to a peak at that system size where $\omega\tau_{RC} \simeq 1$. This is very similar to our finding for the L-dependence of U in Fig. 2.4(a). However, a key difference between Q' and U involves their large-L scaling behaviour, which is seen to be given by $Q' \propto L^{-1}$ in Fig. 2.8(c) whereas we found $U \propto L^{-2}$ in Fig. 2.4(c). As we mentioned earlier, changing the system size affects the electrolytic cell in a similar way as changing the driving frequency ω. However, in contrast to changing ω, which leaves the geometrical characteristics of the electrolytic cell and, correspondingly, those of the elements of the equivalent circuit unaffected, they change when κL is increased. At larger system sizes $\kappa L \gtrsim 100$, the impedance corresponding to C_2 grows and effectively closes the C_2 branch of the full circuit for the current, turning it into a simplified circuit of Fig. 2.7(c). This in turn implies that the scaling of Q' with L should be the same as with ω in the case of a simplified circuit i.e. it should decay as L^{-1}, which is exactly what

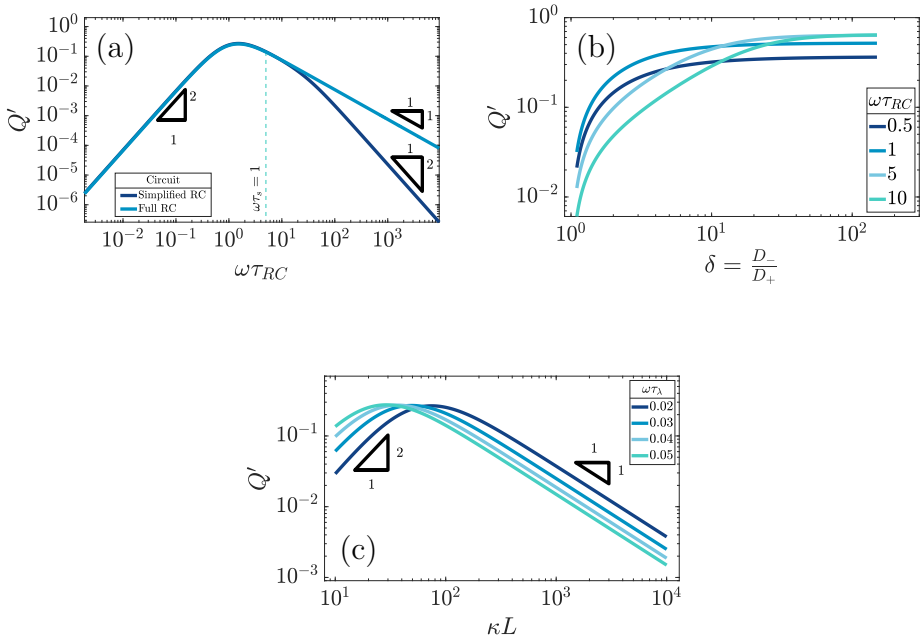

Figure 2.8: Dependence of the analytically calculated period-averaged charge difference Q' given by Eq. (2.33) for our standard parameter set (see text) on (a) the dimensionless frequency $\omega\tau RC$, (b) the asymmetry of ionic mobilities $\delta = \frac{D_-}{D_+} = R_+/R_-$, and (c) system size κL. In (a) Q' is plotted for the full equivalent RC circuit of Fig. 2.7(a) and for the simplified one of Fig. 2.7(c). In (b) Q' is plotted for several driving frequencies ω. The effective diffusion coefficient D, and, consequently, the frequency ω, is kept fixed along each curve. In (c) Q' is plotted for several driving frequencies ω. Both (b) and (c) are based on the full equivalent circuit.

we see in Fig. 2.8(c). The reason why we saw the decay $U \propto L^{-2}$ in the PNP case is that increasing the system size of the electrolytic cell not only reduces C_2 to negligible magnitude for large κL, but also linearly decreases the applied electric field at fixed Ψ_0, which together result in $U \propto L^{-2}$ rather than $U \propto L^{-1}$.

We can conclude that the modified linear-circuit model captures quite a few of aspects of the numerical PNP results of the AREF. The toy model essentially suggests that the key ions are the ones closest to the electrode (anions in one half of the period and cations in the other half). The time-averaged result is dominated by the faster anions.

2.7 SUMMARY AND DISCUSSION

We studied the static time-averaged electric field that arises in the AC-driven electrolytic cell shown in Fig. 2.1 if the cations and anions have unequal diffusion coefficients $D_+ < D_-$. We solved the governing non-linear coupled Poisson-Nernst-Planck (PNP) equations numerically to study how the magnitude of this so-called asymmetric rectified electric field (AREF) depends on the main system parameters such as the amplitude of the applied AC voltage Ψ_0, the driving frequency ω, the ionic mobility asymmetry δ, and the system size L. We also solved the linearized PNP equations analytically and constructed an equivalent RC-circuit for the electrolytic cell. Based on this circuit, which involves a capacitor C_2 in parallel with a series of a restistor R and a capacitor C_1, we propose a modification that serves as our toy model to describe and explain the physical mechanisms responsible for the nonlinear AREF effect in terms of linear circuits. The key is to consider two different resistances (R_+ and R_- associated with the different diffusion coefficients D_+ and D_- of the cations and the anions, respectively) during different phases of the driving voltage, with cations/anions dominating the oscillating dynamics at negative/positive electrode potentials.

Let us for comparison briefly mention an appealing alternative toy model for AREF, proposed in Ref.[66], in which the key idea is to consider two point charges that oscillate in anti-phase with different amplitudes to mimic the AC driving of a (monovalent) cation and anion with different mobilities. Interestingly, the motion of these two ions is shown to create a non-zero time-averaged electric field far from the oscillation origin, which is then considered to be the analogue of AREF. While this picture is very appealing at first sight and seems to capture the essential AREF physics, it would actually only apply to a one-dimensional line of ions that connect the electrodes and that interact with three-dimensional "$1/r$" Coulomb potentials. In the geometry

of interest here, however, the analogue would be oscillating three-dimensional planes of charge, which by Gauss law interact by one-dimensional Coulomb potentials "$|z - z'|$" such that both species produce a spatially constant but oppositely directed electric field that exactly cancels in a globally neutral system. So despite its attractive appeal its predicted AREF is strongly affected by the geometry of three-dimensional space.

The modified linear-circuit toy model proposed here, which is based on the (dis-)charging of 3D capacitive EDLs in planar geometry, also has some shortcomings. Nevertheless, it describes the scaling of the AREF magnitude with several important system parameters quite well and reveals the physical mechanism behind AREF generation. The asymmetry in the ion mobilities introduces an asymmetry in the speed of the charging process of the EDLs during the two half periods of negative and positive electrode potentials. At driving frequencies ω of the order of the characteristic charging time of EDLs in the system, $\omega\tau_{RC} \sim 1$, the asymmetry causes a time-averaged ionic charge distribution where the faster ions are on average closer to the electrode and play the role of the surface charge in conventional EDLs, while the slower ones play the role of the screening cloud. This results in a non-zero time-averaged EDL-like AREF structure. Even though AREF is essentially a non-linear screening phenomenon, we could gain some additional insight from a linearized RC-circuit analysis where we considered the resistance R to take different values $R_+ \propto D_+^{-1}$ and $R_- \propto D_-^{-1}$ during different phases of the AC-potential. Interestingly, our circuit analysis also yields a new time scale $\tau_s = \sqrt{\tau_{RC}\tau_D}$ which implies the peculiar scaling $\tau_s \propto L^{1/2}$ for a given electrolyte. This time scale involves a key role for the dielectric capacitor C_2, even in the large-L regime of interest where the EDL capacitor $C_1 = \kappa L C_2 \gg C_2$. Physically τ_s corresponds to the timescale that separates the low-frequency regime from the high-frequency one. When $\omega\tau_s = 1$ the phase angle of the current in the full electric circuit (see Fig. 2.7(a)) has a minimum. While C_2 might be safely set to zero at correspondingly low frequencies $\omega\tau_s \lesssim 1$, it becomes increasingly important at higher frequencies. The timescale τ_s therefore also defines the threshold between the regimes in which the system can be treated as the simple RC circuit in series of Fig. 2.7(c) at low frequencies $\omega\tau_s \ll 1$ and the full circuit of Fig. 2.7(a) at high frequencies $\omega\tau_s \gg 1$.

Finally, by studying the currents in the full electric circuit of Fig. 2.7(a) as shown in Fig. 2.9, we can also give the Debye time τ_D an additional physical interpretation. The currents in the C_1 and C_2 branches of the circuit of Fig. 2.7(a) become approximately equal in magnitude when $\omega\tau_D = 1$ (for $\kappa L \gg 1$). This means that τ_D corresponds to a timescale, at which the EDLs are built to such an extent that the combined impedance of the EDL capacitance and the bulk resistance of the cell becomes equal to that of the capacitor created by the electrodes of the cell.

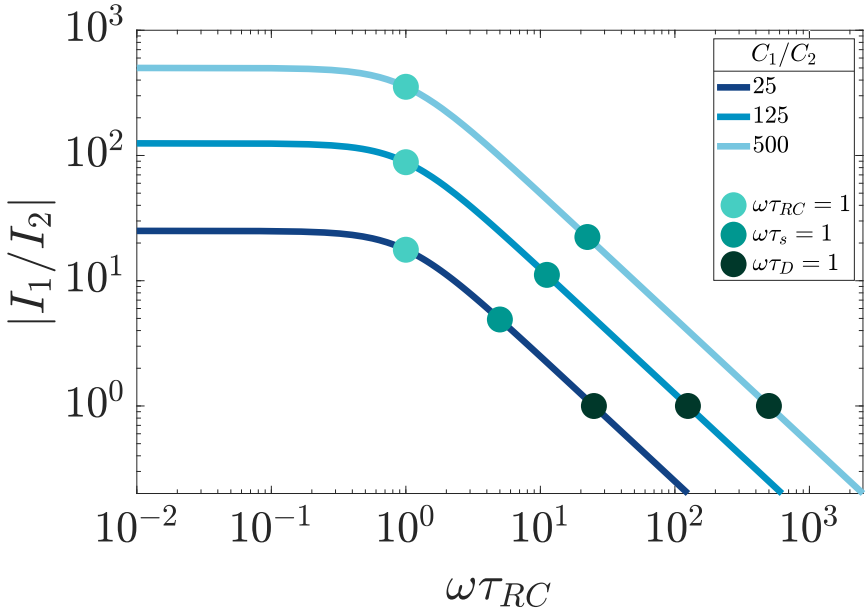

Figure 2.9: Dependence of the ratio of electric current magnitudes $|I_1/I_2|$ in the RC_1 and C_2 branches of the full circuit on the driving frequency ω, for various ratios of C_1/C_2 for our standard parameter set (see text). We clearly see that the currents have equal magnitude $I_1 = I_2$ for $\omega\tau_D = 1$, independently of the ratio C_1/C_2.

Extensions of our work could possibly involve the inclusion of REDOX or acid-base reactions, which would give additional time scales because of the reaction rates. Other directions could involve AC-electroosmosis or non-sinusoidal sawtooth-like potentials that break the symmetry between

charging and discharging, in fact even for electrolytes with equal mobilities of the cations and anions. We speculate that amplification or suppression of the AREF effect is possible by tuning the combination of electrolyte, surface chemistry, and driving potential.

2.8 APPENDIX

The goal of this Appendix is to construct a linear equivalent electric circuit for the electrolytic cell of the main text in Chapter 2. For convenience we briefly describe the system of interest here once again. It consists of a 3D aqueous electrolyte of relative dielectric constant ε at room temperature confined between two parallel macroscopic planar electrodes at a distance L from each other, where we assume translational invariance in the lateral directions. The electrolyte consists of two types of monovalent point-like ions: cations $(+)$ and anions $(-)$ characterized by valencies $z_\pm = \pm 1$ and diffusion coefficients $D_\pm$. The total number of cations and anions is equal, hence the total system is electroneutral. The electrodes are blocking, so that no ion can leave the electrolyte and we exclude any chemical REDOX reactions. The system is driven by an AC voltage $\Psi(t) = \Psi_0 e^{i\omega t}$ applied to the left electrode placed in the plane $z = -\frac{L}{2}$, whereas the right one, placed at $z = \frac{L}{2}$, is kept grounded. Here ω is the imposed angular frequency and Ψ_0 the amplitude. The system is presented as a schematic image in Fig. 2.10).

As it was stated in the main text, we use the Poisson-Nernst-Planck (PNP) equations to study the system.

$$\frac{\partial^2 \Psi(z,t)}{\partial z^2} = -\frac{e}{\varepsilon_0 \varepsilon}\Big(c_+(z,t) - c_-(z,t)\Big), \tag{A1}$$

$$J_\pm(z,t) = -D_\pm\left(\frac{\partial c_\pm(z,t)}{\partial z} \pm \beta e c_\pm(z,t)\frac{\partial \Psi(z,t)}{\partial z}\right), \tag{A2}$$

$$\frac{\partial c_\pm(z,t)}{\partial t} = -\frac{\partial J_\pm(z,t)}{\partial z}. \tag{A3}$$

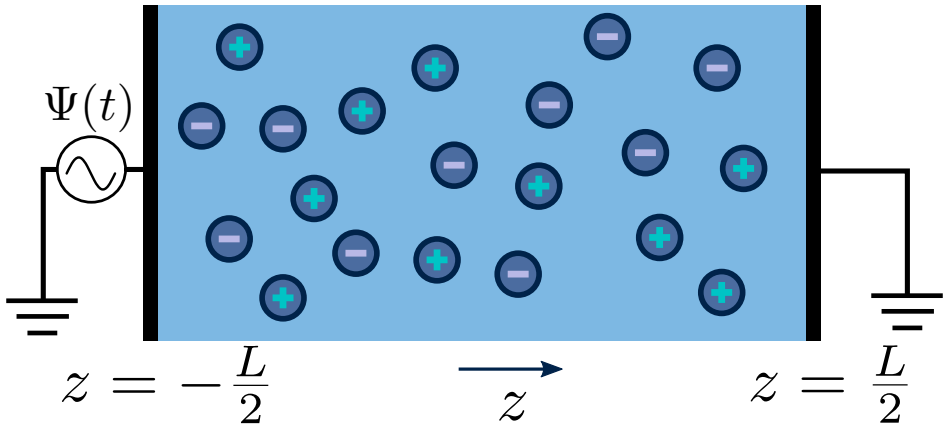

Figure 2.10: Schematic representation of the aqueous 1:1 electrolyte of interest containing a continuum solvent and two ionic species confined between two parallel blocking electrodes separated by a distance L. The electrolyte is driven by a time-dependent electric potential $\Psi(t)$ applied to the electrode at $z = -\frac{L}{2}$, while the other one at $z = \frac{L}{2}$ is kept grounded.

The PNP equations Eqs. (A1), (A2) and (A3) form a closed set for the concentrations $c_\pm$, the fluxes $J_\pm$ and the potential Ψ. Solving PNP equations explicitly requires boundary and initial conditions, which we write as

$$\Psi(-L/2, t) = \Psi_0 e^{i\omega t}, \tag{A4}$$

$$\Psi(L/2, t) = 0, \tag{A5}$$

$$J_\pm(-L/2, t) = J_\pm(L/2, t) = 0, \tag{A6}$$

$$c_\pm(z, t = 0) = c_s, \tag{A7}$$

where c_s is the fixed initial average salt concentration, that is equal for both ionic species in our symmetric $1:1$ electrolyte. Due to Eq. (A3) combined with boundary conditions Eq. (A6) the number of cations and anions will be conserved such that

$$\frac{1}{L}\int_{-L/2}^{L/2} c_{\pm}(z,t)\,dz = c_s. \tag{A8}$$

As the non-linear set of PNP equations can not be solved fully analytically, in order to qualitatively understand physical processes taking place in the electrolytic cell we employ a toy model relying on the combination constructed by combining two simple linear electric circuits, as described in the main text. In this appendix we will demonstrate how the equivalent electric circuit is determined by deriving the frequency response of the electrolytic cell with a harmonic voltage applied to it and then matching it to that of a linear electric circuit. In order to do so we will use PNP equations to derive an expression for the impedance $Z(\omega)$ of the system and determine the corresponding equivalent circuit by matching the frequency response of the circuit impedance $Z_c(\omega)$ to $Z(\omega)$.

2.8.1 *Linearising PNP Equations*

If we were to construct an equivalent circuit that matched the frequency response of the impedance $Z(\omega)$ derived from the non-linear PNP equations exactly, we would need to employ non-linear circuit elements for it. This, however, would not be of much use for us, as the main goal of constructing an equivalent circuit is to simplify the system. On the contrary, if we linearise the PNP equations, they can be easily solved analytically allowing us to derive an expression for the electrolytic cell impedance $Z(\omega)$ to then match it to the impedance of a linear electric circuit $Z_c(\omega)$. In the following sections we show how $Z(\omega)$ is derived from linearised PNP equations and construct the corresponding equivalent circuit. But before we proceed with derivations, we first simplify the equations and notation. We start by introducing the following combinations for concentrations:

$$c_+(z,t) - c_-(z,t) \equiv q(z,t), \tag{A9}$$

$$c_+(z,t) + c_-(z,t) \equiv s(z,t). \tag{A10}$$

We then also expand all the variables into Fourier modes

$$q(z,t) = c_s \sum_{n=-\infty}^{\infty} q_n(z) e^{in\omega t}, \tag{A11}$$

$$s(z,t) = c_s \left(2 + \sum_{n=-\infty}^{\infty} s_n(z) e^{in\omega t} \right), \tag{A12}$$

$$\Psi(z,t) = A \sum_{n=-\infty}^{\infty} \Phi_n(z) e^{in\omega t}, \tag{A13}$$

where we will us $A = \Psi_0$ for notational convenience in the intermediate steps. We also introduced the $2c_s$ term in Eq. (A12) to take the bulk concentration into account and streamline the Fourier expansion.We also expand the driving potential

$$\Psi(z = -L/2, t) = A \sum_{n=-\infty}^{\infty} a_n(z) e^{in\omega t}, \tag{A14}$$

$$\Psi(z = L/2, t) = 0, \tag{A15}$$

where $a_n = a^*_{-n}$ coefficients are real and known, as the driving voltage is of a defined form. Notice the difference between the system description and this condition - instead of applying the driving voltage to one electrode while having the other one grounded, in calculations we apply the driving voltage (with opposite signs) to both electrodes simultaneously. It is easy to see, that these conditions are equivalent, whereas having both electrodes driven simplifies the expressions further in the calculations without affecting the final result.

We now insert all the above into the PNP equations to rewrite them in terms of Fourier modes. Eqs. (A11) and (A13) are inserted into the Poisson equation

$$\nabla^2\Psi(z,t) = -\frac{e}{\varepsilon_0\varepsilon}q(z,t), \tag{A16}$$

and equate the powers of exponents (i.e. frequencies) on both sides of the equation. As a result we get

$$\nabla^2\Phi_n(z) = -\frac{ec_s}{\varepsilon_0\varepsilon}q_n(z). \tag{A17}$$

Before inserting Fourier decompositions into the Nernst-Planck equations, we rewrite them more conveniently.

$$\frac{J_+(z,t)}{D_+} = -\frac{1}{2}\left((s+q)' + \beta e(s+q)\Psi'\right), \tag{A18}$$

$$\frac{J_-(z,t)}{D_-} = -\frac{1}{2}\left((s-q)' - \beta e(s-q)\Psi'\right), \tag{A19}$$

where $'$ denote the ∂_z derivatives. Summing them up gives

$$\frac{J_+(z,t)}{D_+} + \frac{J_-(z,t)}{D_-} = -\frac{1}{2}\left(2s' + 2\beta eq\Psi'\right), \tag{A20}$$

whereas taking the difference gives

$$\frac{J_+(z,t)}{D_+} - \frac{J_-(z,t)}{D_-} = -\frac{1}{2}\left(2q' + 2\beta es\Psi'\right). \tag{A21}$$

Now we sum both continuity Eqs. (A8) and insert Eq. (A20) into the sum to get

$$\frac{1}{2}\left(\frac{1}{D_+}(\dot{s}+\dot{q}) + \frac{1}{D_-}(\dot{s}-\dot{q})\right) = s'' + \beta e(q'\Psi' + q\Psi''), \tag{A22}$$

where $\dot{q} \equiv \partial_t q$. We can rewrite this as

$$\frac{1}{2}\frac{D_+ + D_-}{D_+D_-}\left(\dot{q}\frac{D_- - D_+}{D_+ + D_-} + \dot{s}\right) = s'' + \beta e(q'\Psi' + q\Psi''). \tag{A23}$$

Here we define the effective diffusion coefficient

$$D \equiv \frac{2D_+D_-}{D_+ + D_-}, \tag{A24}$$

and another important combination of diffusion coefficients

$$B \equiv \frac{D_+ - D_-}{D_+ + D_-}, \tag{A25}$$

which vanishes when the mobilities of ions are equal. Using these variables the expression becomes

$$\frac{1}{D}(\dot{s} - B\dot{q}) = s'' + \beta e(q'\Psi' + q\Psi''). \tag{A26}$$

Performing the same actions for the difference of fluxes we get

$$\frac{1}{D}(\dot{q} - B\dot{s}) = q'' + \beta e(s'\Psi' + s\Psi''). \tag{A27}$$

We now insert the Fourier expansions Eqs. (A13),(A12) and (A11) here and again, equate equal frequencies on both sides of the equation. From Eq. (A26) we get

$$\begin{aligned}
&\frac{c_s}{D}\left(\sum_{n=-\infty}^{\infty} in\omega s_n(z)e^{in\omega t} - B\sum_{n=-\infty}^{\infty} in\omega q_n(z)e^{in\omega t}\right) = \\
&= c_s\left(\sum_{n=-\infty}^{\infty} s_n''(z)e^{in\omega t} + \beta e\left[\sum_{k=-\infty}^{\infty} q_k'(z)e^{ik\omega t}\sum_{m=-\infty}^{\infty}\Phi_m'(z)e^{im\omega t} + \right.\right. \\
&\left.\left. + \sum_{k=-\infty}^{\infty} q_k(z)e^{ik\omega t}\sum_{m=-\infty}^{\infty}\Phi_m''(z)e^{im\omega t}\right]\right).
\end{aligned} \tag{A28}$$

Grouping appropriate terms together gives

$$\frac{1}{D}\sum_{n=-\infty}^{\infty}\left(\Big[s_n(z)-Bq_n(z)\Big]in\omega-Ds_n''(z)\right)e^{in\omega t}= \\ =\sum_{k=-\infty}^{\infty}\sum_{m=-\infty}^{\infty}\beta e\left(q_k'(z)\Phi_m'(z)+q_k(z)\Phi_m''(z)\right)e^{i(k+m)\omega t}. \tag{A29}$$

Since we equate terms with similar exponential factors on both sides of the equation, this imposes a condition for indices: $k+m=n\rightarrow k=n-m$. Inserting this back into the equation and equating terms with similar exponents gives

$$\sum_{n=-\infty}^{\infty}\left(\frac{1}{D}\Big[s_n(z)-Bq_n(z)\Big]in\omega-s_n''(z)\right)= \\ =\sum_{m=-\infty}^{\infty}\beta e\left(q_{n-m}'(z)\Phi_m'(z)+q_{n-m}(z)\Phi_m''(z)\right). \tag{A30}$$

Similarly, from Eq. (A27) we get:

$$\sum_{n=-\infty}^{\infty}\left(\frac{1}{D}\Big[q_n(z)-Bs_n(z)\Big]in\omega-Dq_n''(z)-2\beta e\Phi_n''(z)\right)= \\ =\sum_{m=-\infty}^{\infty}\beta e\left(s_{n-m}'(z)\Phi_m'(z)+s_{n-m}(z)\Phi_m''(z)\right), \tag{A31}$$

where we can further rewrite the $2\beta e\Phi_n''(z)$ term. Poisson equation Eq. (A17) can be rewritten in terms of Debye length κ^2. From $\kappa^{-2}=\frac{1}{8\pi\lambda_B c_s}$ we get $\lambda_B=\frac{\kappa^2}{8\pi c_s}$. At the same time by definition $\lambda_B=\frac{e^2\beta}{4\pi\varepsilon\varepsilon_0}$, giving $\frac{e}{\varepsilon\varepsilon_0}=\frac{\kappa^2}{2\beta c_s e}$. Inserting this into the Poisson equation gives:

$$\nabla^2\Phi_n(z)=-\frac{\kappa^2}{2\beta e}q_n(z), \tag{A32}$$

which gives $2\beta e\Phi_n''(z)=-\kappa^2 q_n(z)$. Inserting this back into Eq. (A31) we get:

$$\sum_{n=-\infty}^{\infty}\left(\frac{1}{D}\Big[q_n(z)-Bs_n(z)\Big]in\omega - Dq_n''(z)+\kappa^2 q_n(z)\right)= \\ =\sum_{m=-\infty}^{\infty}\beta e\left(s'_{n-m}(z)\Phi'_m(z)+s_{n-m}(z)\Phi''_m(z)\right). \tag{A33}$$

Denoting the right hand side of Eqs. (A30) and (A33) by $F_q^{(n)}(z)$ and $F_s^{(n)}(z)$ respectively, we can conveniently write these equations as

$$-\frac{in\omega}{D}Bq_n(z)+\frac{in\omega}{D}s_n(z)-s_n''(z)=F_q^{(n)}(z) \tag{A34}$$

$$\left(\kappa^2+\frac{in\omega}{D}\right)q_n(z)-\frac{in\omega}{D}Bs_n(z)-q_n''(z)=F_s^{(n)}(z). \tag{A35}$$

Up to this point we were rewriting the initial equations in such a way that the further treatment and linearization became more convenient. In order to linearize Eqs. (A34) and (A35), we should identify the amplitude of the driving voltage A as a small parameter compared to the thermal voltage $\beta e\Psi_0 = 1$. Using this parameter we can expand all three quantities - $\Phi_n(z)$, $q_n(z)$ and $s_n(z)$ as power series in A. This is allowed to do as deviations of all three variables from their equilibrium conditions (when no voltage is applied to the system) are caused by the applied driving voltage. Additionally, since the applied voltage does not have a static part, the series will start with terms linear in A. So we have

$$\Phi_m(z)=A\Phi_{m,1}(z)+A^2\Phi_{m,2}(z)+\ldots=\sum_{l=1}^{\infty}A^l\Phi_{m,l}(z) \tag{A36}$$

$$q_m(z)=Aq_{m,1}(z)+A^2q_{m,2}(z)+\ldots=\sum_{l'=1}^{\infty}A^{l'}q_{m,l'}(z) \tag{A37}$$

$$s_m(z)=As_{m,1}(z)+A^2s_{m,2}(z)+\ldots=\sum_{l''=1}^{\infty}A^{l''}s_{m,l''}(z). \tag{A38}$$

We now insert this into the right hand side Eqs. (A34) and (A35).

$$F_q^{(n)}(z) = \sum_{m=-\infty}^{\infty} \beta e \Bigg(\sum_{l'=1}^{\infty} A^{l'} q'_{n-m,l'}(z) \sum_{l=1}^{\infty} A^l \Phi'_{m,l}(z) + \\ + \sum_{l'=1}^{\infty} A^{l'} q_{n-m,l'}(z) \sum_{l=1}^{\infty} A^l \Phi''_{m,l}(z) \Bigg) = \\ = A^2 \sum_{m=-\infty}^{\infty} \beta e \Big(q'_{n-m,1}(z) \Phi'_{m,1}(z) + q_{n-m,1}(z) \Phi''_{m,1}(z) \Big) + \mathcal{O}(A^3). \tag{A39}$$

Similarly

$$F_s^{(n)}(z) = A^2 \sum_{m=-\infty}^{\infty} \beta e \Big(s'_{n-m,1}(z) \Phi'_{m,1}(z) + s_{n-m,1}(z) \Phi''_{m,1}(z) \Big) + \mathcal{O}(A^3). \tag{A40}$$

The LHS of Eqs. (A34) and (A35) with this expansion is trivial. Since we are interested in linearized form of the equations, we only consider terms up to a linear order in A on both sides. We end up with the following result:

$$\begin{pmatrix} -B\frac{in\omega}{D} & \frac{in\omega}{D} \\ \kappa^2 + \frac{in\omega}{D} & -B\frac{in\omega}{D} \end{pmatrix} \cdot \begin{pmatrix} q_{n,1} \\ s_{n,1} \end{pmatrix} + \frac{\mathrm{d}^2}{\mathrm{d}z^2} \begin{pmatrix} q_{n,1} \\ s_{n,1} \end{pmatrix} = 0, \tag{A41}$$

which, together with Poisson equation Eq. (A17) is the governing system of equations for our system in the linear regime. As we said in the beginning, we are interested in the frequency response of the electrolytic cell that we are considering. We could continue the derivations with differing diffusion coefficients to derive the proper response of the system, however, it has been shown in Ref.[83] that the frequency response of the system change only very weakly if we take both diffusion coefficients to be the same. And since it is significantly easier to solve Eq. (A41) for $D_+ = D_-$, we will do so here. In this case, $B = 0$ and the system becomes:

$$\begin{pmatrix} 0 & \frac{in\omega}{D} \\ \kappa^2 + \frac{in\omega}{D} & 0 \end{pmatrix} \cdot \begin{pmatrix} q_{n,1} \\ s_{n,1} \end{pmatrix} + \frac{\mathrm{d}^2}{\mathrm{d}z^2} \begin{pmatrix} q_{n,1} \\ s_{n,1} \end{pmatrix} = 0. \tag{A42}$$

Solving the Linearized PNP Equations

Now we can actually solve the system of equations Eq. (A42). Both equations are ordinary differential equations, which can be easily solved to give the general solutions:

$$q_{n,1}(z) = Q_1 e^{k_n z} + Q_2 e^{-k_n z} \tag{A43}$$

$$s_{n,1}(z) = S_1 e^{k_n z} + S_2 e^{-k_n z}, \tag{A44}$$

with

$$k_n^2 = \sqrt{\kappa^2 + \frac{in\omega}{D}}. \tag{A45}$$

We address the s solution first. Combining Eqs. (A6) and (A20) we get

$$s' + \beta e q \Psi' = 0 \tag{A46}$$

Using Eqs. (A11) and (A38) this becomes

$$s_n'(z) \mid_{z=\pm L/2} = 0, \tag{A47}$$

up to linear order in A. Inserting Eq. (A44) here, we end up with $S_1 = S_2 = 0$, giving $s(z) = 0$ as a result in linear regime. This simplifies the equations for $q_{n,1}(z)$ and $\Phi_n(z)$. Due to symmetry of the system $q_{n,1}(0) = 0$ in the middle of the system. This gives $Q_2 = -Q_1$. Hence $q_{n,1}(z) = 2Q_1 \sinh(k_n z)$. As a consequence

$$\nabla^2 \Phi_n(z) = -\frac{2ec_s}{\varepsilon\varepsilon_0} Q_1 \sinh(k_n z) \equiv G \sinh(k_n z). \tag{A48}$$

Integrating this expression twice gives us a solution for $\Phi_n(z)$

$$\Phi_n(z) = G\left(\frac{1}{k_n^2}\sinh(k_n z) + P_1 z + P_2\right). \tag{A49}$$

Using the boundary conditions at the electrodes Eqs. (A4) and (A5)

$$G\left(\frac{1}{k^2}\sinh(-k\frac{L}{2}) - P_1\frac{L}{2} + P_2\right) = \Psi_0 \tag{A50}$$

$$G\left(\frac{1}{k^2}\sinh(k\frac{L}{2})+P_1\frac{L}{2}+P_2\right)=0, \tag{A51}$$

we see, that due to the simple harmonic nature of the driving potential, boundary conditions for the electric potential Eqs. (A4) and (A5) allow us to write

$$\Psi = A\sum_{n=-\infty}^{\infty}\Phi_n(z)e^{in\omega t}=\frac{\Psi_0}{2}\Phi_1(z)e^{i\omega t}\equiv\frac{\Psi_0}{2}\Phi(z)e^{i\omega t}, \tag{A52}$$

i.e. only a single mode $n=1$ survives and we can drop the subscript n from now. Up to linear order in A this gives

$$q(z,t)=c_s\sum_{n=-\infty}^{\infty}q_{n,1}(z)e^{i\omega nt}=c_sq_{1,1}(z)e^{i\omega t}\equiv c_sq(z)e^{i\omega t} \tag{A53}$$

$$\begin{aligned} s(z,t)&=c_s\left(2+\sum_{n=-\infty}^{\infty}s_{n,1}(z)e^{in\omega t}\right)= \\ &=c_s\left(2+s_{1,1}(z)e^{i\omega t}\right)\equiv c_s\left(2+s(z)e^{i\omega t}\right). \end{aligned} \tag{A54}$$

Summing Eqs. (A50) and (A51) equations gives

$$G\left(\frac{1}{k^2}\left[\sinh(-k\frac{L}{2})+\sinh(k\frac{L}{2})\right]+2P_2\right)=\Psi_0\ \ \rightarrow\ \ GP_2=\frac{\Psi_0}{2}, \tag{A55}$$

since $\sinh(-k\frac{L}{2})=-\sinh(k\frac{L}{2})$. And now taking the difference between them gives

$$G\left(-\frac{2}{k^2}\sinh(k\frac{L}{2})-2P_1\frac{L}{2}\right)=\Psi_0 \tag{A56}$$

from where

$$GP_1=-\frac{1}{L}\left(\frac{2G}{k^2}\sinh(k\frac{L}{2})-\Psi_0\right) \tag{A57}$$

In order to determine Q_1 (contained in G), we now need to use the blocking electrode boundary condition for the difference of fluxes Eq. (A21). Up to the linear order in A it takes the following form

$$\begin{aligned} & q'(z,t) + \beta e s \Psi'(z,t) \mid_{z=L/2} = 0 \quad \rightarrow \\ \rightarrow \quad & c_s q'(z = L/2) + 2\beta e c_s \Phi'(z = L/2) + \mathcal{O}(A^2) = 0. \end{aligned} \tag{A58}$$

Inserting here $q'(z) = 2Q_1 k \cosh(kz)$ and $\Phi'(z) = G\left(\frac{1}{k}\cosh(kz) + P_1\right)$ we get

$$kQ_1 \cosh(k\frac{L}{2}) + \beta e G\left(\frac{1}{k}\cosh(k\frac{L}{2}) + P_1\right) = 0. \tag{A59}$$

Inserting $G = -\frac{2ec_s}{\varepsilon\varepsilon_0}Q_1$ and combining similar terms, we end up with an expression for Q_1:

$$Q_1 = -\frac{\frac{1}{2}\beta e k}{\frac{i\omega}{D}\cdot\frac{L}{2}\cosh(k\frac{L}{2}) + \frac{\kappa^2}{k}\sinh(k\frac{L}{2})}\Psi_0. \tag{A60}$$

Using this expression, we also get:

$$GP_1 = \frac{\frac{i\omega}{2D}\cosh(k\frac{L}{2})}{\frac{i\omega}{D}\cdot\frac{L}{2}\cosh(k\frac{L}{2}) + \frac{\kappa^2}{k}\sinh(k\frac{L}{2})}\Psi_0, \tag{A61}$$

giving us together with Eq. (A49) the final expression for the potential

$$\begin{aligned} \Phi(z) = & \left\{\frac{2ec_s}{\varepsilon\varepsilon_0 k^2}\cdot\frac{\frac{1}{2}\beta e k\cdot\sinh(kz)}{\frac{i\omega}{D}\cdot\frac{L}{2}\cosh(k\frac{L}{2}) + \frac{\kappa^2}{k}\sinh(k\frac{L}{2})} + \right. \\ & \left. + \frac{\frac{i\omega}{2D}\cosh(k\frac{L}{2})}{\frac{i\omega}{D}\cdot\frac{L}{2}\cosh(k\frac{L}{2}) + \frac{\kappa^2}{k}\sinh(k\frac{L}{2})}z + \frac{1}{2}\right\}\Psi_0 = \\ = & \frac{\Psi_0}{2}\left(\frac{\frac{\kappa^2}{k}\sinh(kz) + \frac{i\omega}{D}\cosh(k\frac{L}{2})\cdot z}{\frac{\kappa^2}{k}\sinh(k\frac{L}{2}) + \frac{i\omega}{D}\cdot\frac{L}{2}\cosh(k\frac{L}{2})} + 1\right), \end{aligned} \tag{A62}$$

where in the first term we used that $\kappa = \frac{2e^2\beta c_s}{\varepsilon\varepsilon_0}$. This can be further simplified to

$$\Phi(z) = \frac{\Psi_0}{2}\left(\frac{\sinh(kz) + i\omega\tau_1\cosh(k\frac{L}{2})\cdot kz}{\sinh(k\frac{L}{2}) + i\omega\tau_1\cosh(k\frac{L}{2})\cdot k\frac{L}{2}} + 1\right), \tag{A63}$$

where $\tau_1 \equiv \frac{1}{D\kappa^2}$. As we will see in the coming section, these results allow us to study the frequency response of the electrolytic cell, knowing which will allow us to construct an equivalent electrical circuit.

2.8.2 *Constructing Equivalent Circuit*

Frequency Response of the System

In order to study the frequency response of an electrolytic system, we use electrical impedance defined as

$$Z(\omega) = \frac{\Delta\Psi}{I}, \tag{A64}$$

where $\Delta\Psi$ is the total voltage drop over the system and I is the current flowing through the system. Physically impedance acts like an effective resistance of the whole cell.

There is a good reason why the impedance is used to study the frequency response of an electrolytic system. Electrolyte consists of electrically neutral molecules and mobile charges. When an external voltage is applied to it, the mobile charges will rearrange in a specific way to screen the electric field created by the external voltage. This process can be characterised by a characteristic timescale. At the same time, molecules of the electrolyte will reorient in the electric field created by the external voltage, further decreasing the electric field inside the electrolyte. Depending on the molecule type, their reorientation timescales are different. Therefore, we end up with different timescales for the response of the system to an alternating driving voltage. This implies, that the effective resistance of the system, impedance, will vary depending on the frequency of the driving voltage. This, together with the possibility to measure it experimentally, makes impedance a good candidate for the frequency response study.

We will be using Argand Complex Plane plots for a complex impedance $Z(\omega) = Z'(\omega) + iZ''(\omega)$ (in conjunction with the Bode plot, which is discussed in the main text). In these parametric plots x axis represents the real part of the complex number $Z'(\omega)$, whereas y axis - the imaginary part $Z''(\omega)$ with ω being the parameter. Argand diagram allows us to readily

identify not only the linear circuit elements that should be included in the equivalent electrical circuit, but also how they should be connected - in series, or parallel.

To make matters clearer, let us consider two examples of Argand plots for the simplest electrical circuits - RC circuit in series and in parallel. For the series RC circuit, shown in Fig. 2.11(a) the impedance is

$$Z(\omega) = R + \frac{1}{i\omega C}. \tag{A65}$$

We see, that the real part $Z'(\omega) = R$ does not depend on the frequency, whereas the imaginary part $Z''(\omega) = \frac{1}{\omega C}$ is inversely proportional to ω. The corresponding parametric curve will thus be a vertical line, as shown in Fig. 2.11(c). On this plot, the absolute value of the impedance $\mid Z(\omega) \mid$ at a given frequency ω is the distance from the origin of the plot to the corresponding point on the vertical line. And the slope of the line connecting these two points characterizes the ratio of the real and imaginary parts of the impedance

$$\varphi = \arctan\left(\frac{Z''(\omega)}{Z'(\omega)}\right). \tag{A66}$$

For the parallel RC circuit, shown in Fig. 2.11(a), the impedance is also easy to calculate

$$Z(\omega) = \frac{1}{\frac{1}{R} + i\omega C} = \frac{R}{1 + (\omega C)^2} - i\frac{\omega R^2 C}{1 + (\omega C)^2} \tag{A67}$$

and produces a semi-circle curve on the frequency response plot stretching from point $\Big(\mathrm{Re}(Z(\omega)) = 0, \mathrm{Im}(Z(\omega)) = 0\Big)$ when $\omega \to \infty$, to point $\Big(\mathrm{Re}(Z(\omega)) = R, \mathrm{Im}(Z(\omega)) = 0\Big)$ when $\omega \to 0$, as we see in Fig. 2.11(d).

Frequency response of the electrolytic cell impedance is more complicated. Using the definition of impedance we get

$$Z(\omega) = \frac{\Delta\Psi}{I} = \frac{2\Big(\Phi(-L/2) - \Psi_0/2\Big)e^{i\omega t}}{\dot{Q}(-L/2, t)}, \tag{A68}$$

where

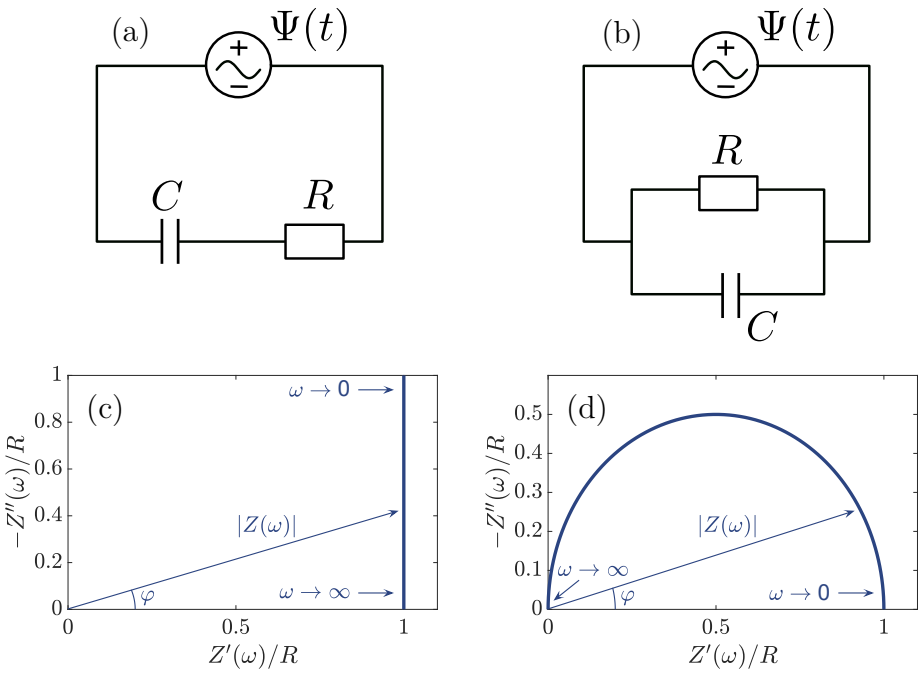

Figure 2.11: (a) RC electrical circuit connected in series. (b) RC electrical circuit connected in parallel. (c) Argand diagram of series RC electrical circuit. The parametric plot is a vertical line positioned at $\mathrm{Re}(Z(\omega)) = R$. The imaginary part $\mathrm{Im}(Z(\omega)) = 0$ when $\omega \to \infty$ and $\mathrm{Im}(Z(\omega)) \to \infty$ when $\omega \to 0$. (d) Argand diagram examples for simple electrical circuits. The parametric plot is a semi-circle. When $\omega \to \infty$, the real and imaginary parts of the impedance take the values of $\mathrm{Re}(Z(\omega)) = 0$ and $\mathrm{Im}(Z(\omega)) = 0$ respectively, whereas when $\omega \to 0$, then they are equal to $\mathrm{Re}(Z(\omega)) = R$ and $\mathrm{Im}(Z(\omega)) = 0$.

$$Q(-L/2,t) = S_0\sigma(-L/2,t) = S_0\varepsilon_0\varepsilon E(-L/2,t) = -S_0\varepsilon_0\varepsilon\Phi'(-L/2)e^{i\omega t} \tag{A69}$$

is the charge on the left plate of the capacitor and $\sigma(-L/2,t)$ the surface charge at the same point. Thus

$$\dot{Q}(-L/2,t) = -i\omega S_0 \varepsilon_0 \varepsilon \Phi'(-L/2) e^{i\omega t}. \tag{A70}$$

Inserting this back into Eq. (A64) we get

$$\begin{aligned} Z(\omega) &= \frac{2}{S_0 \varepsilon \varepsilon_0 i\omega} \frac{\sinh(kL/2) + i\omega\tau_1 \cosh(k\frac{L}{2}) \cdot k \cdot (L/2)}{k\cosh(-kL/2) + i\omega\tau_1 \cosh(k\frac{L}{2}) \cdot k} = \\ &= \frac{2}{S_0 \varepsilon \varepsilon_0} \frac{\tanh(kL/2) + i\omega\tau_1 \cdot k(L/2)}{i\omega k(1 + i\omega\tau_1)}. \end{aligned} \tag{A71}$$

This can be simplified a bit more. We rewrite

$$kL = L\sqrt{\kappa^2 + \frac{i\omega}{D}} = \kappa L\sqrt{1 + i\omega\tau_1} \tag{A72}$$

and split the square root into real and imaginary parts

$$\begin{aligned} x \equiv \sqrt{1 + i\omega\tau_1} &= \left(\sqrt{\frac{\sqrt{1 + \omega^2\tau_1^2} + 1}{2}} + i\sqrt{\frac{\sqrt{1 + \omega^2\tau_1^2} - 1}{2}} \right) \equiv \\ &\equiv \mathrm{Re}(x) + i\mathrm{Im}(x), \end{aligned} \tag{A73}$$

where we see, that $\mathrm{Re}(x) \geq 1$. Using $\tanh(kL/2)$ definition we write

$$\tanh(kL/2) = \frac{1 - e^{-kL}}{1 + e^{-kL}} = \frac{2}{1 + e^{-kL}} - 1. \tag{A74}$$

Combining Eqs. (A73) and (A72) and inserting into Eq. (A74), we get

$$\tanh(x) = \frac{2}{1 + e^{-\kappa L(\mathrm{Re}(x) + i\mathrm{Im}(x))}} - 1 = \frac{2}{1 + e^{-\mathrm{Re}(x)\kappa L} \cdot e^{-i\mathrm{Im}(x)\kappa L}} - 1, \tag{A75}$$

from where it becomes clear, that the imaginary part does not affect the modulus of the expression in the denominator and it is completely dictated by the size of $\kappa L \gg 1$. Therefore we can expand Eq. (A75) to get

$$\tanh(x) \approx 1 - 2 \cdot e^{-R\kappa L} \cdot e^{-iI\kappa L} \approx 1. \tag{A76}$$

This allows us to safely drop $\tanh(kL/2)$ term to arrive at

$$Z(\omega) \approx \frac{1}{S_0 \varepsilon \varepsilon_0} \cdot \frac{2 + i\omega\tau_2\sqrt{1 + i\omega\tau_1}}{i\omega\kappa(1 + i\omega\tau_1)^{3/2}}, \tag{A77}$$

where we also used, that $\tau_2 = \tau_1 \cdot \kappa L = \frac{L}{\kappa D}$. This result allows us now to study the frequency response of the electrolytic cell. The parametric plot $-Z''(\omega)$ vs. $Z'(\omega)$ is presented on Fig. 2.5(a).

Constructing Equivalent Electrical Circuit

Knowing the frequency response of the electrolytic cell, it can be recast into an equivalent electrical circuit containing simple elements connected in such a way, that the frequency response and hence the impedance of such a circuit matches that of the cell. This is convenient, as equivalent circuits are much easier to treat. Since we already know, how each linear circuit element affects the Argand diagram, it is easy to identify, that the frequency response of the electrolytic cell corresponds to an equivalent electrical circuit presented in Fig. 2.7(a), or Fig. 2.7(b) (in the main text we discuss why we chose the former over the latter one). Comparison of frequency response plots between the electroytic cell (solid lines) and the electric circuit (dashed lines) of Fig. 2.7(a) is presented in Fig. 2.6, where we see a good agreement between the shapes of the two at different parameter sets.

Now that we have identified the equivalent electrical circuit, we also need to determine expressions for the individual elements C_1, C_2 and R. For this we need the expression for the equivalent circuit impedance as well. Using the rules of impedance calculation for parallel and series connections, we can easily get the expression for the total impedance

$$Z = \frac{i\omega RC_1 + 1}{i\omega\Big(C_1 + C_2(i\omega RC_1 + 1)\Big)}. \tag{A78}$$

These two expressions for impedances - Eqs. (A77) and (A78) allow us now to extract expressions for the equivalent circuit elements. In principle we could directly compare them and try identifying the elements, however, since these two functions can not be mapped 1 : 1 to each other, as seen in Fig. 2.6, they can not be equated directly. Fortunately, the impedance expressions

get significantly simplified in certain limiting cases, allowing us to derive expressions for the linear elements of the equivalent circuit.

Equating the electrolytic cell impedance to the equivalent circuit one in the limit of $\omega \to \infty$ we get

$$\frac{1}{S_0 \varepsilon \varepsilon_0} \cdot \frac{L}{i\omega} = \frac{1}{i\omega C_2}, \tag{A79}$$

giving us

$$C_2 = \frac{S_0 \varepsilon \varepsilon_0}{L}. \tag{A80}$$

The second one is the limit of $\omega \to 0$. In this case we get:

$$\frac{2}{S_0 \varepsilon \varepsilon_0 \kappa} = \frac{1}{i\omega(C_1 + C_2)}. \tag{A81}$$

Inserting here Eq. (A80) we get

$$C_1 = \frac{S_0 \varepsilon \varepsilon_0 \kappa}{2} - C_2 = \frac{S_0 \varepsilon \varepsilon_0 \kappa}{2} \left(1 - \frac{2}{\kappa L}\right). \tag{A82}$$

Finally, in order to get an expression for R, motivated by the shape of the frequency response curve, we should compare the real parts of both impedances in the infinite frequency limit. For future convenience, we explicitly show the results for the real and imaginary parts of the equivalent circuit impedance

$$Z'(\omega) = \frac{R C_1^2}{(C_1 + C_2)^2 + C_1^2 C_2^2 R^2 \omega^2}, \tag{A83}$$

$$Z''(\omega) = -\frac{C_1 + C_2 + C_1^2 C_2 R^2 \omega^2}{\omega \left((C_1 + C_2)^2 + C_1^2 C_2^2 R^2 \omega^2\right)}. \tag{A84}$$

Doing the same for the electrolytic cell, equating the real parts and applying $\omega \to \infty$ limit we get the following expression for R

$$R = \frac{L}{S_0 \varepsilon \varepsilon_0 \kappa} \cdot \frac{1}{\left(1 - \frac{2}{\kappa^2 L}\right)^2}. \tag{A85}$$

However, since in our case we are always interested in large systems, for which $\kappa L \gg 1$, it makes sense to apply this limit to Eqs. (A80), (A87) and (A85) expressions to get the final expressions for the equivalent electrical circuit elements

$$C_2 = \frac{S_0 \varepsilon \varepsilon_0}{L}, \tag{A86}$$

$$C_1 = \frac{S_0 \varepsilon \varepsilon_0 \kappa}{2}, \tag{A87}$$

$$R = \frac{L}{S_0 \varepsilon \varepsilon_0 D \kappa^2} = \frac{L}{2 S_0 D \beta e^2 c_s}. \tag{A88}$$

It is interesting to note, that these expressions have clear physical interpretations. Capacitance C_2 characterises a plate capacitor with size equal to that of the system - L, i.e. C_2 corresponds to the capacitor created by the two blocking electrodes. Capacitance C_1, on the other hand, characterises the effective capacitor created by two plate capacitors connected in series (introducing factor 2 in the numerator of Eq. (A87)). Size of each of these capacitors is equal to the Debye length κ^{-1}. Therefore, C_1 describes two EDLs, that are created at each electrode. Finally, resistance R characterises the resistance of the bulk part of the system and is, consequently, proportional to the system size L.

Knowing how the equivalent electrical circuit looks like and the expressions for its constituent elements, we can use it to study the electrolytic cell more conveniently. For example, one of the more interesting details about the behavior of the electrolytic cell can be seen by comparing its frequency response in Fig. 2.5(a) to that of the series RC circuit, plotted in Fig. 2.11(c). As we see, for sufficiently low frequencies, the electrolytic cell starts to behave like a series RC circuit. Since this is a convenient simplification of the problem, it is interesting to see, at what frequencies that happens. For this we need to find the extrema of the parametric curve of frequency response. Taking derivatives of Eqs. (A83) and (A84) with respect to ω, dividing them and equating the result to 0 gives us an equation for the extrema of the parametric plot. We only consider positive frequency solutions

$$\omega_1 = \sqrt{\frac{(C_1+C_2)\left(C_1 - \sqrt{C_1^2 - 8C_1C_2} - 2C_2\right)}{2C_1^2C_2^2R^2}}, \tag{A89}$$

$$\omega_2 = \sqrt{\frac{(C_1+C_2)\left(C_1 + \sqrt{C_1^2 - 8C_1C_2} - 2C_2\right)}{2C_1^2C_2^2R^2}}. \tag{A90}$$

As we said, we are interested in the large system limit $\kappa L \gg 1$. First we insert Eqs. (A80), (A87) and (A85) expressions here. Then, we keep terms up to the linear order in $\frac{1}{\kappa L}$ in Eq. (A89) and 0^{th} order terms in Eq. (A90). This gives

$$\omega_1 \approx D\kappa^2\sqrt{\frac{2}{\kappa L}}, \tag{A91}$$

$$\omega_2 \approx \sqrt{\frac{C_1(C_1+C_1)}{2C_1^2C_2^2R^2}} = \frac{1}{C_2R} = D\kappa^2. \tag{A92}$$

The second solution of Eq. (A92) corresponds to the maximum on the semi-circle of the frequency response plot, which is a well known timescale of Eq. (2.12). It is the first solution that we are after - it represents a point on the Argand plot Fig. 2.5(a), that denotes transition to the vertical line, which, as we already know, corresponds to a series RC circuit. So, this point determines the frequency, after which we can treat the electrolytic cell as a series RC circuit. We can put the corresponding frequencies, together with $\omega\tau_{RC} = 1$, on the Argand diagram, as seen on Fig. 2.5(a). All the timescales are discussed in more detail in the main text.

3

ASYMMETRIC RECTIFIED ELECTRIC FIELDS FOR SYMMETRIC ELECTROLYTES

ABSTRACT

In this chapter, building upon the discovery of asymmetric rectified electric fields (AREF) in recent experiments [S.H. Hashemi et al., Physical Review Letters **121**, 185504 (2018)], we explore the generation of AREF by applying a sawtooth-like voltage to 1:1 electrolytes with equal diffusion coefficients confined between two planar blocking electrodes. This differs from an earlier approach based on a sinusoidal AC voltage applied to 1:1 electrolytes with unequal diffusion coefficients. By numerically solving the full Poisson-Nernst-Planck equations, we demonstrate that AREF can be generated by a slow rise and a fast drop of the potential (or vice versa), even for electrolytes with equal diffusion coefficients of the cations and anions. We employ an analytically constructed equivalent electric circuit to explain the underlying physical mechanism. Importantly, we find that the strength of AREF can be effectively tuned from zero to its maximal value by only manipulating the time-dependence of the driving voltage, eliminating the necessity to modify the electrolyte composition between experiments. This provides valuable insights to control the manipulation of AREF, which facilitates enhanced applications in diverse electrochemical systems.

3.1 INTRODUCTION

Studying the behavior of an aqueous electrolyte subjected to an externally applied oscillating electric field often involves the use of alternating current (AC) voltages. For instance, an AC voltage is commonly used in areas such as induced charge electrokinetics [38, 76, 171–173], particle assembly in electrolytes [174–181], AC electroosmosis [182–188], cyclic voltammetry [189–194], batteries [196–203], sensing [183, 185, 195], and impedance spectroscopy [47, 197–204]. One of the main reasons for choosing AC electric fields over DC fields in various applications is to avoid any net current or net charge in the system, since the field has a zero mean over one cycle.

A basic geometry that can capture many of the essential physical effects of an AC field is a globally neutral 1:1 electrolyte of point-like ions confined between two blocking electrodes and subjected to a harmonic AC voltage. If the frequency of the AC voltage is relatively low or zero (as in equilibrium), then a so-called Electric Double Layer (EDL), consisting of the surface charges of the solid and a diffuse ionic cloud with opposite charge, will form at the interface between a charged solid (electrode, colloid, etc.) and an electrolyte. The EDL harbors a surplus of counter-ions and a reduced concentration of co-ions compared to the bulk, thereby screening the electric field of the electrode. The typical thickness of a fully formed EDL is equal to the Debye length λ_D, which is about 10 nm for water with 1 mM salt concentration at room temperature. One of the interesting recent findings in such a (vertical) system with horizontal electrodes concerned colloids floating in the gravitational field. Here, charged colloids suspended in an aqueous electrolyte were confined between two horizontal blocking electrodes that were driven by a harmonic AC potential. Contrary to intuition, rather than sedimenting in the gravitational field the colloidal particles were observed to float against the gravitational pull [41, 42]. This led to a theoretical investigation to elucidate the source of the force that allows the colloids to withstand the gravitational field. In Ref.[66] it was shown that period-averaged electrode charge is not necessarily zero in the case of cations (+) and anions (-) with unequal diffusion coefficients, $D_+ \neq D_-$. The resulting period-averaged induced electric field is therefore also non-zero and stretches from the electrodes well into the bulk of the electrolyte. It was termed Asymmetric Rectified Electric

Field (AREF). The electric force generated by AREF was proposed as a mechanism that would enable the colloids to counteract the gravitational pull. It is noteworthy that a recent study has proposed alternative mechanisms for colloidal floating, including dielectrophoresis (DEP) or electrohydrodynamical (EHD) mechanisms [69]. Interestingly, the predominant contribution of each mechanism to the floating height of colloids remains a subject of investigation.

This paper focuses on AREF. The authors of the original study extensively explored AREF from sinusoidal voltages by examining its space dependence on various system parameters in Ref. [68], numerically solving the governing system of non-linear differential equations in Ref. [58], and investigating the application of AREF in reversing the flow of electroosmosis in Ref. [67]. Nevertheless, several aspects of the underlying physical mechanism of AREF remained unclear. In our recent publication [1] we employ equivalent electric circuits to devise a simplified toy model that qualitatively reproduce the parameter dependencies of AREF, shedding light on the underlying physical mechanism. It was explained how the asymmetry of ion diffusion coefficients in the electrolyte can create AREF. However, the scope of manipulating AREF is constrained by the rather limited range of ion diffusion coefficients and their disparities. Furthermore, experimental studies on AREFs necessitate altering electrolytes for each new experiment, demanding a significant investment of time and effort. To address these challenges, we opted to study one and the same electrolyte, for simplicity a symmetric 1:1 electrolyte with equal ion diffusion coefficients $D \equiv D_+ = D_-$, and instead study the possibility of introducing the necessary asymmetry for AREF generation through the functional form of the driving potential. A convenient form that is both asymmetric and periodic, yet averages to zero over time, is the so-called "sawtooth" potential

$$\Psi(t) = \frac{2\Psi_0}{\pi} \sum_{n=1}^{\infty} (-1)^{n+1} \frac{\sin(n\omega t)}{n}, \tag{3.1}$$

where $\Psi_0 > 0$ is the amplitude and $T = 2\pi/\omega$ the period the of the driving voltage $\Psi(t)$. In Fig. 3.1(a), where we plot two periods of $\Psi(t)$ given by Eq. (3.1) as a function of the dimensionless time t/T , we see that the sawtooth function rises steadily towards its maximum Ψ_0 and then drops "instantaneously" to its minimum $-\Psi_0$. This slow rise and fast drop breaks

the symmetry of the charging and discharging processes at the electrodes, as we will see. At the same time, the (absolute) areas S_1 and S_2 under the curve are equal, $S_1 = S_2$, resulting in a period-averaged applied potential equal to zero, i.e. there is no direct bias of the voltage.

While the full sawtooth function is indeed a very convenient candidate for the time-dependence of the driving voltage, it is less attractive for the numerical study that we undertake in this work, not only because of the large number of required harmonic "modes" in Eq. (3.1) but also because of the discontinuity of the full potential. It turns out that the essence of the creation mechanism of AREF can be studied in full detail by avoiding the sharpest feature of the full potential and keeping only the first two terms in the sawtooth series of Eq. (3.1). Thus, henceforth the driving voltage of interest is given by

$$\Psi(t) = \frac{2\Psi_0}{\pi} \sum_{n=1}^{2} (-1)^{n+1} \frac{\sin(n\omega t)}{n}, \tag{3.2}$$

which is plotted in Fig. 3.1(b). One checks that the role of the second harmonic term is to break the symmetry between rising and lowering voltages. All numerical results in this paper will be based on this "two-term" sawtooth function, that captures the key physics even though its actual amplitude is only $\sim 0.9\Psi_0$. However, for convenience and clarity we will refer to the full sawtooth function when explaining and discussing the AREF mechanism.

This paper is structured as follows: In Section 3.2, we present the system of interest along with the Poisson-Nernst-Planck (PNP) equations that control the processes in the electrolytic cell. In Section 3.3 we explain how AREF effects are generated under the influence of the sawtooth driving potential for a specific set of system parameters. In Section 3.4, we use numerical methods to investigate how the AREF varies with the main system parameters. Finally, in Section 3.5 we sum up and discuss our results.

3.2 POISSON-NERNST-PLANCK EQUATIONS

The system of interest, schematically illustrated in Fig. 3.2, is essentially the same electrolytic cell as the one considered in our previous paper [1],

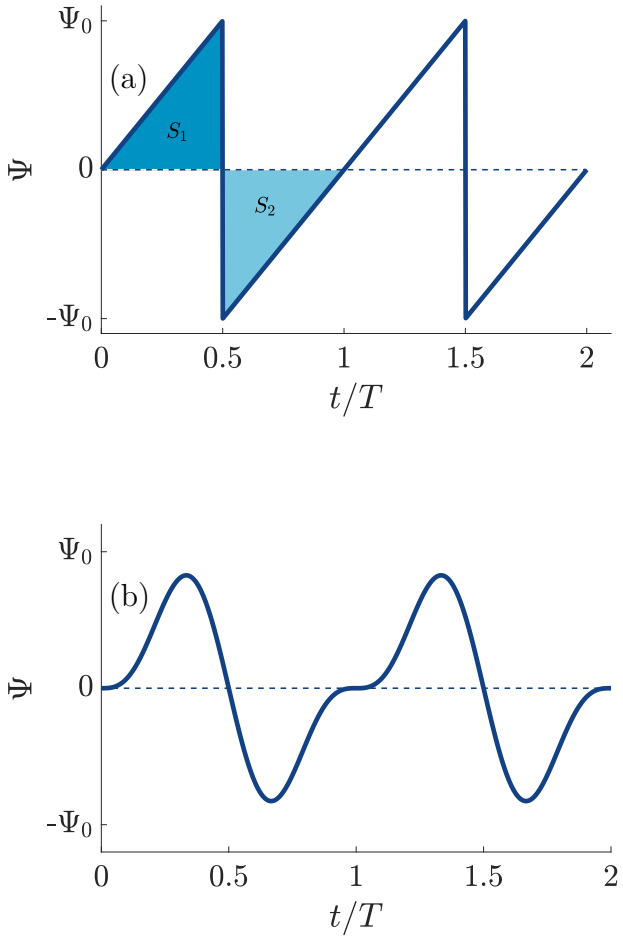

Figure 3.1: Two periods of (a) the full sawtooth voltage $\Psi(t)$ based on Eq. (3.1) and (b) the two-term sawtooth voltage based on Eq. (3.2). Both voltages have a period T, feature an asymmetry between (slow) rising and (fast) lowering voltages, and average out to zero during a period. The two-term sawtooth avoids sharp transitions, rendering itself more convenient for numerical calculations.

therefore its description and the notation we use will follow Ref. [1] very closely. The cell comprises a three-dimensional aqueous electrolyte with a relative dielectric constant ϵ at room temperature, confined between two parallel macroscopic planar electrodes separated by a distance L. We assume translational symmetry in the lateral directions. Apart from the continuum solvent, the electrolyte is composed of two types of monovalent point-like ions: cations $(+)$ and anions $(-)$ with valencies ± 1 and equal diffusion coefficients $D_\pm \equiv D$. The total number of cations and anions is equal, ensuring overall electroneutrality in the system. The electrodes are blocking, preventing ions from leaving the electrolyte, and we exclude any chemical REDOX reactions. The system is subjected to the AC sawtooth voltage of Eq. (3.2) containing only two terms in the series, applied to the left electrode placed in the plane $z = -\frac{L}{2}$, whereas the right one, situated at $z = \frac{L}{2}$, remains grounded. The imposed angular frequency is denoted by ω, and Ψ_0 represents the amplitude of the applied voltage.

We study this system in terms of the the Poisson-Nernst-Planck (PNP) equations. The ionic fluxes, denoted as $J_\pm(z,t)$, comprise a diffusive component arising from ion concentration gradients and a conductive component resulting from the potential gradient. These aspects are collectively described by the Nernst-Planck equation given by

$$J_\pm(z,t) = -D\left(\frac{\partial c_\pm(z,t)}{\partial z} \pm \beta e c_\pm(z,t)\frac{\partial \Psi(z,t)}{\partial z}\right), \tag{3.3}$$

where $c_\pm(z,t)$ represent the concentrations of cations $(+)$ and anions $(-)$ at the position z and time t and $\Psi(z,t)$ the local electrostatic potential. Here e is the elementary charge and β^{-1} the product of the Boltzmann constant and the temperature. Eq. (3.3) also assumes spatially constant diffusion coefficients. Given the absence of chemical reactions in the system, the concentrations and fluxes are connected through the continuity equation

$$\frac{\partial c_\pm(z,t)}{\partial t} + \frac{\partial J_\pm(z,t)}{\partial z} = 0. \tag{3.4}$$

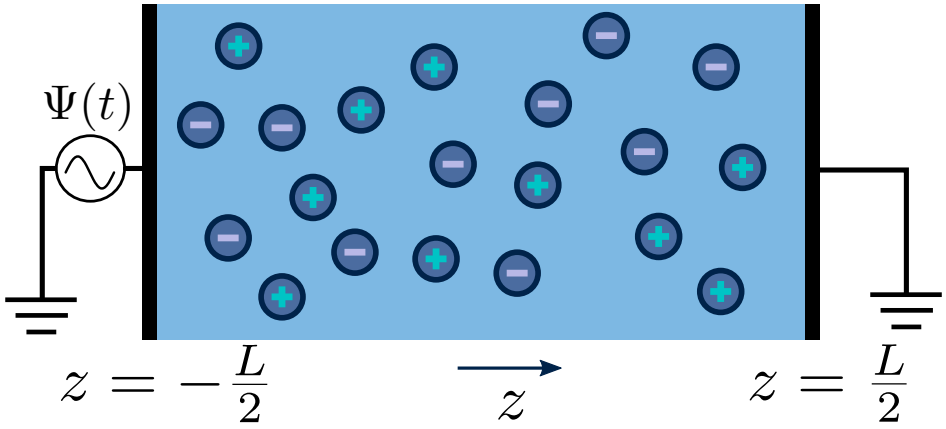

Figure 3.2: Schematic illustration of the aqueous 1:1 electrolyte under consideration, comprising a continuous solvent and two ionic species, enclosed between two parallel blocking electrodes with a separation distance L. The ions in the electrolyte are driven by the time-dependent electric sawtooth potential $\Psi(t)$ of Eq. (3.2) applied to the electrode at $z = -\frac{L}{2}$, while the opposite electrode at $z = \frac{L}{2}$ remains grounded.

The local potential profile $\Psi(z,t)$ is connected to the local charge density $e\Big(c_+(z,t) - c_-(z,t)\Big)$ through the Poisson equation, which for $|z| < \frac{L}{2}$ reads

$$\frac{\partial^2 \Psi(z,t)}{\partial z^2} = -\frac{e}{\epsilon_0 \epsilon}\Big(c_+(z,t) - c_-(z,t)\Big), \tag{3.5}$$

where ϵ_0 is the permittivity of vacuum and $\epsilon = 80$ represents water as a structureless continuum.

The PNP equations (3.3), (3.4), and (3.5) form a closed set that fully describes the time-dependent profiles of the concentrations $c_\pm$, the fluxes $J_\pm$,

and the potential Ψ. The explicit solution of the PNP equations requires boundary and initial conditions, for which we take

$$\Psi(-L/2,t) = \frac{2\Psi_0}{\pi}\left(\sin(\omega t) - \frac{1}{2}\sin(2\omega t)\right), \tag{3.6}$$

$$\Psi(L/2,t) = 0, \tag{3.7}$$

$$J_{\pm}(-L/2,t) = J_{\pm}(L/2,t) = 0, \tag{3.8}$$

$$c_{\pm}(z,t=0) = c_s \quad \text{for} \quad z \in [-L/2, L/2]. \tag{3.9}$$

Here c_s represents the constant initial salt concentration, which is identical for both ionic species in the $1:1$ electrolyte of interest and thus satisfies global charge neutrality. As implied by Eq. (3.4) coupled with the boundary conditions specified in Eq. (3.8), the total number of anions and cations in the system is conserved such that

$$\frac{1}{L}\int_{-L/2}^{L/2} c_{\pm}(z,t)\,dz = c_s \tag{3.10}$$

is satisfied at all times $t \geq 0$. For a given set of parameters Ψ_0, ω, D, c_s, and L Eqs. (3.5) – (2.8) constitute the system of non-linear coupled differential equations. We employ the finite-element solver of COMSOL® to numerically solve these equations.

Convenient insight into relevant dimensionless system parameters can be obtained as follows. In the static (low-frequency) limit equilibrium holds, such that the applied potential $\Psi(-L/2,t) = \Psi_0$ is a time-independent constant and $J_{\pm}(z,t) = 0$. In the linear-screening regime with $|\beta e \Psi_0| \lesssim 1$, the EDLs get fully developed at the two electrodes and the NP equation (3.3) can be integrated to obtain the Boltzmann distribution

$$c_{\pm}(z) = c_s'\left(1 \mp \frac{\Psi_0 \beta e \sinh(\kappa z)}{2\sinh(\kappa L/2)}\right), \tag{3.11}$$

with κ^{-1} the characteristic Debye length of the equilibrium EDL given by

$$\kappa^{-1} = \sqrt{\frac{\epsilon\epsilon_0}{2e^2\beta c_s'}} \equiv \lambda_D. \tag{3.12}$$

The concentration c_s' is an integration constant that is very close to c_s in the large L-limit of interest here, so throughout the paper we set $c_s' = c_s$ in the definition of λ_D. In this limit, as we have shown before in Ref.[1], the characteristic timescale of EDL formation [65] is written as the RC time

$$\tau_{RC} = \frac{L\lambda_D}{2D} = \frac{L}{2\kappa D}. \tag{3.13}$$

For future convenience we also define the Debye time

$$\tau_D = \frac{1}{\kappa^2 D} = \tau_{RC}\frac{2}{\kappa L}, \tag{3.14}$$

during which the ions diffuse over a distance of the order of the Debye length [65, 71].

For the convenience of numerical investigation of AREF, we establish a standard parameter set that includes the (dimensionless) amplitude and frequency of the driving potential, denoted as $\beta e\Psi_0 = 3$ and $\omega\tau_{RC} = 1$, respectively. The standard (dimensionless) system size is fixed at $\kappa L = 50$. We note that this standard parameter set is physically realistic, as it corresponds for an aqueous 1:1 electrolyte with a salt concentration $c_s = 1$ mM to a Debye length $\lambda_D = 10$ nm and hence a system length $L = 500$ nm, and with a typical diffusion coefficient $D = 1.09\ \mu\text{m}^2/\text{ms}$ we find $\tau_{RC} = 2.3\ \mu$s and hence a driving period $T = 14.4\ \mu$s. Any deviation from this standard set will be explicitly stated. All measurements are performed in the late-time limit-cycle regime, when all the transient effects have vanished. This way all the time-dependencies in the system have the same period as that of the driving voltage, with at most a phase difference as we will see.

3.3 AREF FROM SAWTOOTH POTENTIALS

Most of the previous work on AREF concentrated on asymmetric electrolytes containing ions with unequal diffusion coefficients driven by a harmonic (single-frequency sinusoidal) voltage [41, 42, 58, 66–69, 205]. To appreciate the differences of AREF between these asymmetric electrolytes and the systems of interest here consisting of a symmetric 1:1 electrolyte (with equal diffusion coefficients) driven by the sawtooth potential of Eq. (3.6), we briefly recall the mechanism of AREF in the asymmetric case.

As was discussed in Ref.[1], the mechanism behind the creation of AREF in a system with an asymmetric electrolyte relies on the concentration *difference* of the faster (more mobile) ions gathering at the electrodes during a half-period $T/2$ and the slower (less mobile) oppositely charged ions during the complementary half period, an effect that is particularly strong for intermediate driving frequencies $\omega\tau_{RC} \sim 1$. As a result, in the vicinity of both electrodes the period-averaged concentration of the faster ions exceeds that of the slower ions, and the resulting period-averaged charge distribution $e\langle c_+ - c_-\rangle(z)$ in the electrolyte was found to be nonzero and results in a nontrivial period-averaged electrostatic potential $\langle\Psi\rangle(z)$ and an associated period-averaged electric field (AREF) $\langle E\rangle(z) = -d\langle\Psi\rangle(z)/dz$. Here we defined the period-average of a function $f(z,t)$ as

$$\langle f\rangle(z) = \frac{1}{T}\int_{t_0}^{t_0+T} f(z,t)\,dt, \tag{3.15}$$

where t_0 is the (sufficiently late) time at which we start averaging. Because of the symmetry and equivalence between the two electrodes, at least at the period-averaged level, we find (for the asymmetric electrolyte with sinusoidal driving) perfect mirror symmetry with respect to the midplane for the period-averaged potential, so $\langle\Psi\rangle(z) = \langle\Psi\rangle(-z)$, and likewise for the ionic concentrations and the charge density. The electric field, by contrast, exhibits perfect anti-mirror symmetry with respect to the midplane, thus $\langle E\rangle(z) = -\langle E\rangle(-z)$ [1]. As a consequence of this symmetry, it was found in Ref.[1] that a convenient integral quantity to characterize (the strength of) AREF was the time- and space-averaged (dimensionless) electric potential $U \equiv \beta e\frac{1}{L}\int_{-\frac{L}{2}}^{\frac{L}{2}} dz\langle\Psi\rangle(z)$. An additional consequence of these (anti-)symmetries combined with global charge neutrality was a vanishing period-averaged surface charge density $\langle\sigma\rangle$ on both electrodes at $z = \pm L/2$, such that not only $\langle\Psi\rangle(\pm L/2) = 0$ but also $\langle E\rangle(\pm L/2) = 0$ for asymmetric electrolytes with symmetric driving voltages.

Compared to the case of asymmetric ion diffusion coefficients that we just discussed, the system of a 1:1 electrolyte with equal ionic diffusion coefficients driven by the asymmetric sawtooth voltage has a different mechanism for AREF creation. This is immediately apparent from Fig. 3.3(a), that shows the numerical solution of the PNP equations of the period-averaged charge

density profile $\langle c_+ - c_- \rangle(z)$ for our standard parameter set. At the left electrode placed at $z = -L/2$ we see a period-averaged accumulation of negative ionic charge, whereas on the opposite side at $z = L/2$ an equal but opposite (positive) charge density accumulates in the vicinity of the electrode. Clearly, this charge density profile is anti-symmetric with respect to mirroring in the midplane, $\langle c_+ - c_- \rangle(z) = -\langle c_+ - c_- \rangle(-z)$, which contrasts the mirror symmetry we encountered earlier in the cases of unequal ionic mobilities. Such an antisymmetric period-averaged charge distribution creates a perfectly mirror-symmetric AREF $\langle E(z) \rangle$, as also shown in Fig. 3.3(b), where we notice that the electric fields at $z = \pm L/2$, so at the electrodes, do not vanish. This implies by the Gauss law that the period-averaged surface charge $\langle \sigma \rangle$ on the electrodes is non-zero in this case. At the same time we see in Fig. 3.3(c) that the period-averaged potential profile $\langle \Psi \rangle(z)$ follows the anti-mirror-symmetry of the charge distribution. As a consequence, its spatial average U will be identically zero, which implies that, unlike in Ref.[1], it cannot be used as a measure for the AREF strength. Instead, it is now natural to use the time-averaged surface charge density $\langle \sigma \rangle$ on the electrodes for this purpose, or rather its dimensionless version

$$\sigma' \equiv \frac{\langle \sigma \rangle}{\sigma_m} = \left. \frac{\beta e \kappa^{-1} \langle E \rangle(z)}{4\pi \sinh(\beta e \Psi_0/2)} \right|_{z=-L/2}, \tag{3.16}$$

where we introduced the Gouy-Chapman surface charge density $\sigma_m = e(\kappa/\lambda_B)\sinh(\beta e \Psi_0/2) \approx 7.6$ mC/m^2 at the static voltage $\beta e \Psi_0 = 3$ as a reference, with the Bjerrum and Debye length set to $\lambda_B = e^2/4\pi\epsilon_0\epsilon k_B T \simeq 0.72$ nm and $\kappa^{-1} \simeq 10$ nm, respectively.

To understand the mechanism behind AREF in the present system, we will use the so-called equivalent circuit corresponding to the system that we are studying. It is well known that several aspects of electrolytic systems can often be approximated by equivalent electronic circuits [50, 77–80], with Ref.[81] providing a historical overview on this matter. As was shown in Ref.[1], the system in Fig. 3.2 can in the linear screening regime $\beta e \Psi_0 \ll 1$ be approximated by the circuit shown in Fig. 3.4(a), where the capacitors C_1

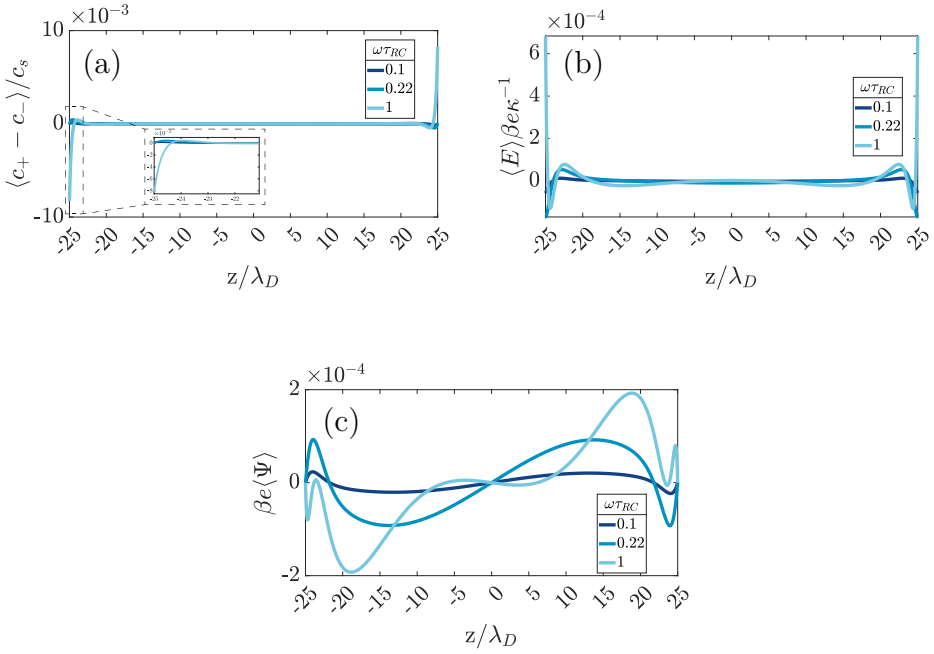

Figure 3.3: Time-averaged dimensionless spatial profiles of the (a) ionic charge density $\langle c_+ - c_- \rangle / c_s$, (b) electric field $\beta e \kappa^{-1} \langle E \rangle$, and (c) electric potential $\beta e \langle \Psi \rangle$ in a 1:1 aqueous electrolyte confined between two planar electrodes separated by distance $L = 50\lambda_D$. The electrode at $z = L/2$ is grounded, whereas the one at $z = -L/2$ is driven by an AC Sawtooth potential of Eq. (3.6) with amplitude $\Psi_0 = 3/\beta e = 75$ mV. Three different driving frequencies $\omega\tau_{RC} = 0.1, 0.22, 1$ with RC-time τ_{RC} given by Eq. (3.13) are denoted with different colors.

and C_2 and the resistor R take, for an electrolytic system of lateral area A, the form

$$C_1 = \frac{A\epsilon\epsilon_0\kappa}{2}; \qquad C_2 = \frac{A\epsilon\epsilon_0}{L}, \tag{3.17}$$

$$R = \frac{L}{A} \cdot \frac{1}{\epsilon\epsilon_0 D\kappa^2} = \frac{L}{A} \cdot \frac{1}{2D\beta e^2 c_s}. \tag{3.18}$$

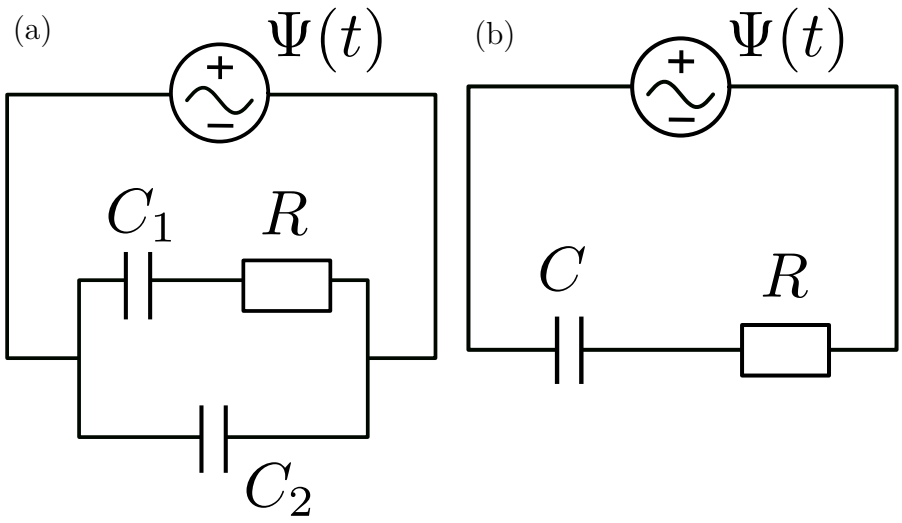

Figure 3.4: (a) Equivalent electric circuit corresponding to the large electrolytic cell with $L \gg \kappa^{-1}$ in the linear regime. Resistance and capacitance of the cell at infinite frequency are denoted by R and C_2 respectively, whereas the total capacitance of two fully developed electric double layers at the electrodes is denoted by C_1, as described by Eqs. (3.17) and (3.18). (b) Simplified equivalent electric circuit corresponding to the low-frequency case $\omega\tau_{RC} \ll \sqrt{\kappa L/2}$ with $C = C_1$.

Physically R corresponds to the Ohmic resistance of the homogeneous aqueous electrolyte with monovalent charge carriers of concentration $2c_s$ and mobility βD, and C_1 represents the capacity of the EDLs at the electrodes - it is the net capacity of the two fully developed EDLs in series, each with the linear-screening capacitance $A\epsilon\epsilon_0\kappa$. Similarly, C_2 represents the purely dielectric capacitance of a water-filled parallel-plate capacitor without any ionic charge carriers and characterized by the size L and area A.

Despite the circuit of Fig. 3.4(a) being only a quantitative mapping in the case of the linearized PNP equations valid at small driving potentials, it was demonstrated in Ref.[1] that a lot of qualitative information can still be extracted even in the non-linear regime of interest here. At the same time, Ref.[1] also showed that for low frequencies $\omega\tau_s \lesssim 1$, where $\tau_s = \sqrt{\tau_{RC}\tau_D}$, the circuit of Fig. 3.4(a) can be successfully approximated by a simplified circuit shown in Fig. 3.4(b), which will be employed in this paper. Following the derivations in Ref.[1], and setting $C = C_1$, we first analytically calculate the charge $Q(t)$ accumulated in the capacitors of the circuit when the sawtooth driving voltage of Eq. (3.1) is applied, yielding

$$Q(t) = \frac{2Q_0}{\pi} \sum_{n=1}^{\infty} \frac{(-1)^{n+1}}{n\sqrt{(n\omega RC)^2 + 1}} \cos\left(n\omega t + \varphi_n\right), \tag{3.19}$$

where $Q_0 = \Psi_0 C$ is a reference charge and $\varphi_n = \arctan(1/(n\omega RC))$ the n-the phase angle. In Fig. 3.5 we plot two periods of $Q(t)/Q_0$ as a function of (dimensionless) time t/T for the same driving as in Fig. 3.1(a) (so for all harmonic modes rather than only two) for driving frequency $\omega\tau_{RC} = 1$. The phase shift between voltage and charge is evident. The plot identifies the two (dimensionless) times t_1 and t_2 in between which $Q(t) > 0$, and likewise the interval between t_2 and $t_3 = t_1 + 1$ during which $Q(t) < 0$. The plot also shows the maximum q_1, the minimum q_2, and the integrated (absolute) surface areas S_3 and S_4 under the curve of $Q(t)/Q_0$. We see for the present example that while the curve corresponding to the area S_3 has a higher amplitude than that of the area S_4, so $|q_1| > |q_2|$, the base of S_4 is actually wider, $\Delta t_1 \equiv t_2 - t_1 < \Delta t_2 \equiv t_3 - t_2$. In the linear response regime this is such that $S_3 = S_4$ when $S_1 = S_2$ in Fig. 3.1(a), which implies a vanishing period-averaged charge on the capacitor in this linearized case.

However, as we will see in more detail in Section 3.4 below, the electrolytic system of interest is in the non-linear screening regime with a nonzero period averaged (dimensionless) surface charge on the left electrode $\sigma' \sim \Psi_0^3$. This is a consequence of a nontrivial rescaling of the time-dependent electrode charge $\sigma(t)$, that causes the analogues of the extrema q_1 and q_2 of the charge curve to scale non-linearly with the voltage amplitude. In turn, this causes a nontrivial relation between the amplitude difference $\Delta q \equiv |q_1| - |q_2|$ and the base width difference $\Delta t \equiv |\Delta t_1 - \Delta t_2|$, leading to a non-zero time-averaged area $\Delta S = S_3 - S_4 \neq 0$ and consequently to a non-zero time-averaged surface charge σ' with a sign that depends on the system parameters, as we will see in section 3.4 below.

3.4 PARAMETER DEPENDENCE OF AREF

In this section we study the dependence of the numerically obtained time-averaged surface charge σ', defined in Eq. (3.16), on the main system parameters. We recall that all numerical calculations are performed using the two-term truncation of Eq. (3.2). The key results are presented in Fig. 3.6, where we show that $\sigma' \propto \Psi_0^3$, and in Fig. 3.7, where we plot $\sigma'/(\beta e \Psi_0)^3$, in (a) and (c) as a function of the driving frequency for different driving amplitudes (a) and different phase angles $\Delta\phi$ between the two sinusoidal terms of the two-term sawtooth function in Eq. (3.2) (c) as we will see in more detail below, and in (b) as a function of system size at driving several frequencies. In all cases shown in Fig. 3.7, we see variations over an order of magnitude and even changes of the sign, which testify for the substantial tunability of AREF. However, we also see in Fig. 3.6 that the order of magnitude of σ' is at most of the order of 10^{-3}, such that the period-averaged surface charge $\langle\sigma\rangle$ is at least three orders of magnitude smaller than the typical static Gouy-Chapman surface charge density σ_m at $\Psi_0 = 75$ mV as defined below Eq. (3.16) for our system parameters. This does not imply, however, that AREFs are a mere quantitative effect without qualitative consequences, since the force that is exerted by an AREF on a (colloidal) body also depends on its net charge (which should therefore be large enough for AREF to be physically relevant, we estimate typically three orders of magnitude larger than the unit charge for the present (typical) parameters). Therefore, we will

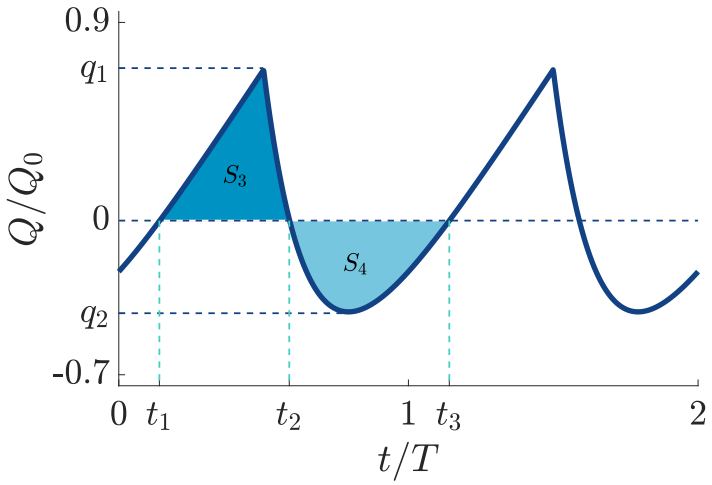

Figure 3.5: The time-dependent charge $Q(t)$ (in units of Q_0) as defined in Eq. (3.19) stored in the capacitor of the linear equivalent circuit of Fig. 3.4(b) as a function of time for the full sawtooth potential $\Psi(t)$ of Eq. (3.1). The asymmetry in the driving potential introduces not only an asymmetry of the positive and negative charge amplitudes, $|q_1| \neq |q_2|$, but also of the time interval that the charge is positive or negative, $t_2 - t_1 \neq t_3 - t_2$. For linear circuits, or linear screening, this translates into a vanishing period-averaged charge since $S_3 = S_4$ identically. In the non-linear case of the electrolytic cell at high voltages, however, this condition gets violated and results in a non-zero period-averaged surface charge σ' on the electrodes.

investigate, discuss, and interpret the dependence of AREF on the system parameters in more detail below.

3.4.1 *Applied Voltage Amplitude*

Similarly to Ref.[1], the range that we consider for the driving voltage amplitude Ψ_0 is limited from above by the point ion approximation, which even for $c_s = 1$mM can become unrealistically high within the point-ion limit due to strong ion crowding effects that take place in actual electrolytes at the

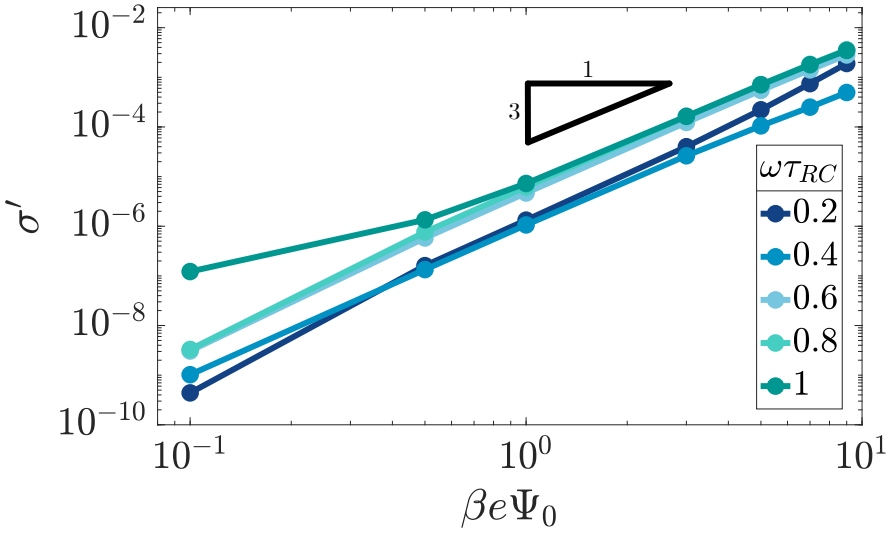

Figure 3.6: Period-averaged dimensionless surface charge σ' of Eq. (3.16) plotted in the double-logarithmic representation against the driving voltage amplitude for varying driving frequencies ω at our standard parameter set (see text). The cubic scaling $\sigma' \sim \Psi_0^3$ demonstrates that AREF is a non-linear effect.

electrodes [74–76]. This occurs beyond $\beta e\Psi_0 \approx 8-9$, which is therefore the upper limit that we consider in Fig. 3.6, where we plot, for various driving frequencies, the dependence of σ' on Ψ_0 for our standard parameter set. The slope of the double-logarithmic curves is essentially identical to 3 across the range of frequencies $\omega\tau_{RC} \in [0.2, 1]$ that we consider here, i.e. $\sigma' \propto \Psi_0^3$. This non-linear scaling confirms that AREF is a non-linear screening effect in the present case of a symmetric electrolyte driven by the sawtooth voltage, very similar to the earlier case of a sinusoidal voltage driving an asymmetric electrolyte as studied in Refs.[1, 66, 68]. This entices the further study of its dependence on frequency, the phase shift between the two harmonic modes of the driving voltage, and the system size in terms of the scaled form $\sigma'/(\beta e\Psi_0)^3$ below.

3.4.2 *Frequency*

In Fig. 3.7(a) we plot $\sigma'/(\beta e\Psi_0)^3$ as a function of the dimensionless frequency $\omega\tau_{RC}$ for our standard parameter set at a number of voltage amplitudes Ψ_0. As expected, the curves essentially collapse for all Ψ_0 and decay to zero in the high and low frequency limits. We assign the irregularities in the graph for the lowest voltage in the high-frequency regime $\omega\tau_{RC} \sim 2-3$ as numerical artefacts without any significant physical meaning, stemming from the small numbers involved. Interestingly, however, in the frequency range $\omega\tau_{RC} \sim 0.1-2$ where the graphs are smooth, the average surface charge curves exhibit a change of sign while featuring both a positive maximum at $\omega\tau_{RC} \sim 1$ and a negative minimum at $\omega\tau_{RC} \sim 0.3$. The mechanism that generates such curves can be best understood in the context of an "area competition" between S_3 and S_4 under the $Q(t)$ curve for the equivalent circuit in Fig. 3.5, as we discussed above, but now with the time-dependent surface charge density $\sigma(t)$ obtained from the nonlinear PNP equations being the analogue of the capacitor charge $Q(t)$ in the linear circuit.

Depending on the parameter range, the $\sigma(t)$ analogue of either Δq or Δt dominates during a period of the (late time) voltage and charge oscillation, determining the the sign of the time-averaged charge. To check this statement, we calculate (the analogues of) Δq and Δt for the numerical results of $\sigma(t)$ (driven by the two-term sawtooth function) and plot their ratio $\Delta q/\Delta t$ as a function of the dimensionless frequency $\omega\tau_{RC}$ in Fig. 3.8. Interestingly, comparing this ratio to the $\sigma'(\omega)$ curve in Fig. 3.7(a), we see a remarkable similarity in the shape of the curves, which suggests that a nontrivial competition between the amplitudes of the time-dependent surface charge and the duration of the time-interval of its positive and negative sign is indeed able to explain the nontrivial non-monotonic shape of the $\sigma'(\omega)$ curve of Fig. 3.7(a).

3.4.3 *System Size*

Fig. 3.7(b) shows the dependence of $\sigma'/(\beta e\Psi_0)^3$ on system size L (in units of the Debye length) for various driving frequencies $\omega\tau_D$ for our standard parameter set. Rather than using the dimensionless combination $\omega\tau_{RC}$ of

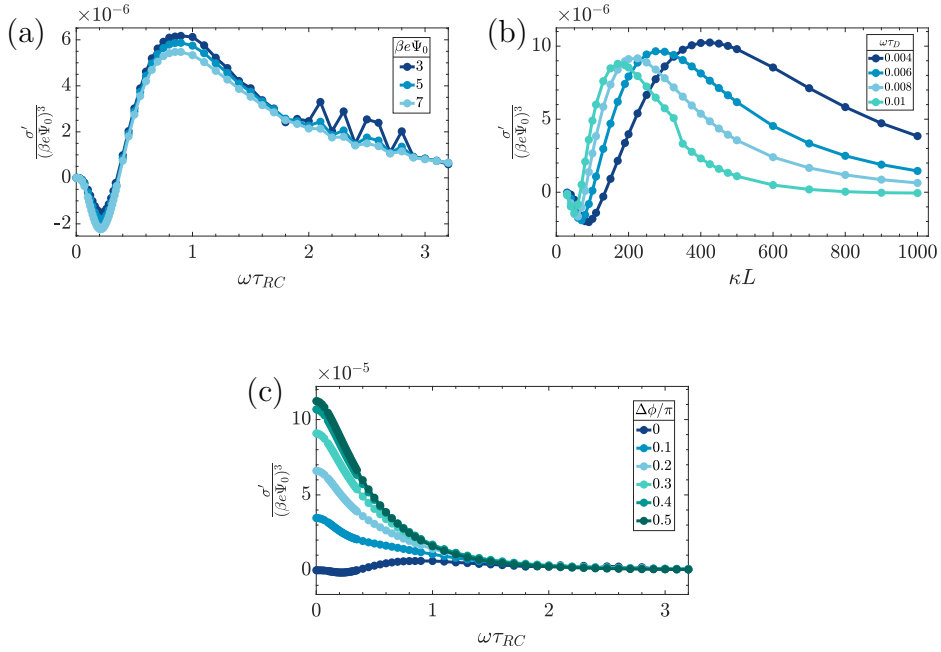

Figure 3.7: Numerically obtained period-averaged dimensionless surface charge $\sigma'/(\beta e\Psi_0)^3$ from late-time solutions of the PNP equations for the standard parameter set (see text) plotted against (a) the dimensionless frequency $\omega\tau_{RC}$ for several voltage amplitudes, (b) the dimensionless system size κL for several dimensionless driving frequencies $\omega\tau_D$, and (c) the driving frequency $\omega\tau_{RC}$ for several phase shifts $\Delta\phi$ of Eq. (3.20). In (a) we see a collapse of the curves for several voltage amplitudes Ψ_0.

Eq. (3.13) to characterize the frequency of the driving voltage, here we use $\omega\tau_D$ defined in Eq. (3.14) as this combination does not depend on L. The maximum σ' for the relatively large system sizes of interest, say in the range of $\kappa L \in [10, 10^3]$, occur at larger κL for lower frequencies $\omega\tau_D$, and one checks that they all correspond to the regime where $\omega\tau_{RC} \sim 1$. This agrees with our findings of Fig. 3.7(a). In fact, the dependence of σ' on frequency in Fig. 3.7(a) and on L in Fig. 3.7(b) are very similar, which in retrospect is

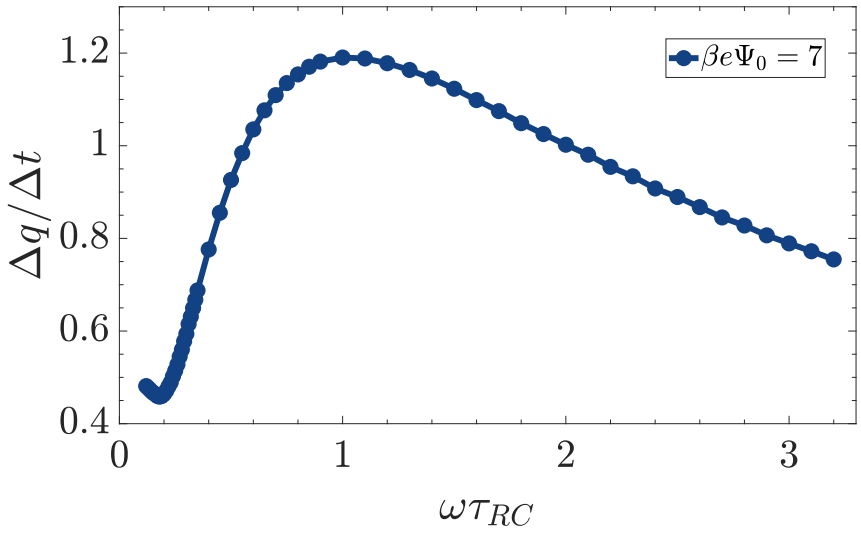

Figure 3.8: Ratio of the amplitude difference and time difference $\Delta q/\Delta t$ for the numerical solution σ' as a function of dimensionless frequency $\omega\tau_{RC}$. Plotted for the standard parameter set (see text), however with $\beta e\Psi_0 = 7$ to minimize the numerical noise seen at higher frequencies in Fig. 3.7(a). The shape of the $\Delta q/\Delta t(\omega)$ curve is remarkably similar to that of the $\sigma'(\omega)$ curve in Fig. 3.7(a).

not surprising since the key dimensionless parameter $\omega\tau_{RC}$ is linear in both L and ω.

3.4.4 *Phase Shift*

As was mentioned in the introduction, the main advantage of using a sawtooth function to drive a symmetric electrolyte in the system of Fig. 3.2 compared to driving an asymmetric electrolyte with a sinusoidal voltage like in Ref.[1], is that one can manipulate AREF by simply altering the sawtooth potential without having to change the electrolyte properties (which would require the electrolyte to be changed in different experiments). As we are using the two-term sawtooth voltage of Eq. (3.6), it is thus interesting to see

whether the AREF can be amplified or suppressed by shifting the relative phase $\Delta\phi$ between two sinusoidal terms away from zero. For this reason we consider the modified driving potential

$$\Psi(t) = \frac{2\Psi_0}{\pi}\left(\sin(\omega t) - \frac{1}{2}\sin(2\omega t + \Delta\phi)\right), \tag{3.20}$$

which is identical to Eq. (3.2) for the case $\Delta\phi = 0$. We note that a nonzero phase shift keeps the period-averaged driving potential equal to zero while it does affect the rate of voltage change substantially and the maximum/minimum voltage during a period somewhat. We plot this driving potential in Fig. 3.9(a) at phase shifts $\Delta\phi/\pi = 0, 0.2, 0.5$, and 0.8 in the panels I through IV, respectively, together with the charge $Q(t)$ accumulated in the capacitor of the equivalent circuit of Fig. 3.4(b) in Fig. 3.9(b). As we see in Fig. 3.9(a), any of the three nonzero phase shifts increases the maximum and decreases the minimum of the driving voltage, resulting in an increase of Δq in the corresponding plots of $Q(t)$ in Fig. 3.9(b). At the same time, while Δt changes with $\Delta\phi$, it does not get affected by the non-linearity of AREF, thus it does not influence the surface charge dependence on the phase shift $\sigma'(\Delta\phi)$. On this basis, one could expect a strong effect of $\Delta\phi$ on the average surface charge σ' in the non-linear electrolytic cell.

This strong effect of the phase shift is indeed confirmed by Fig. 3.7(c), where we plot $\sigma'/(\beta e\Psi_0)^3$ as a function of the dimensionless frequency $\omega\tau_{RC}$ for our standard parameter set at $\Delta\phi/\pi = 0, 0.2, 0.5$, and 0.8. We see that as we shift the phase the AREF effect can actually increase by as much as an order of magnitude, reaching its highest values at $\Delta\phi = 0.5\pi$. At the same time, we see that it only changes sign with frequency for the case $\Delta\phi = 0$. Increase of Δq with phase shift is well reflected in Fig. 3.10, where we plot σ' as a function of the phase shift $\Delta\phi$ at a fixed frequency of $\omega\tau_{RC} = 1$. As we see, the average surface charge has a maximum at $\Delta\phi = 0.4\pi$ and a minimum at $\Delta\phi = 1.4\pi$, where it also has the opposite sign.

3.4.5 *Sawtooth AREF vs. Symmetric AREF*

Here we briefly compare the spatial dependence and the magnitude of AREF in the present case of a symmetric electrolyte with equal ionic diffusion

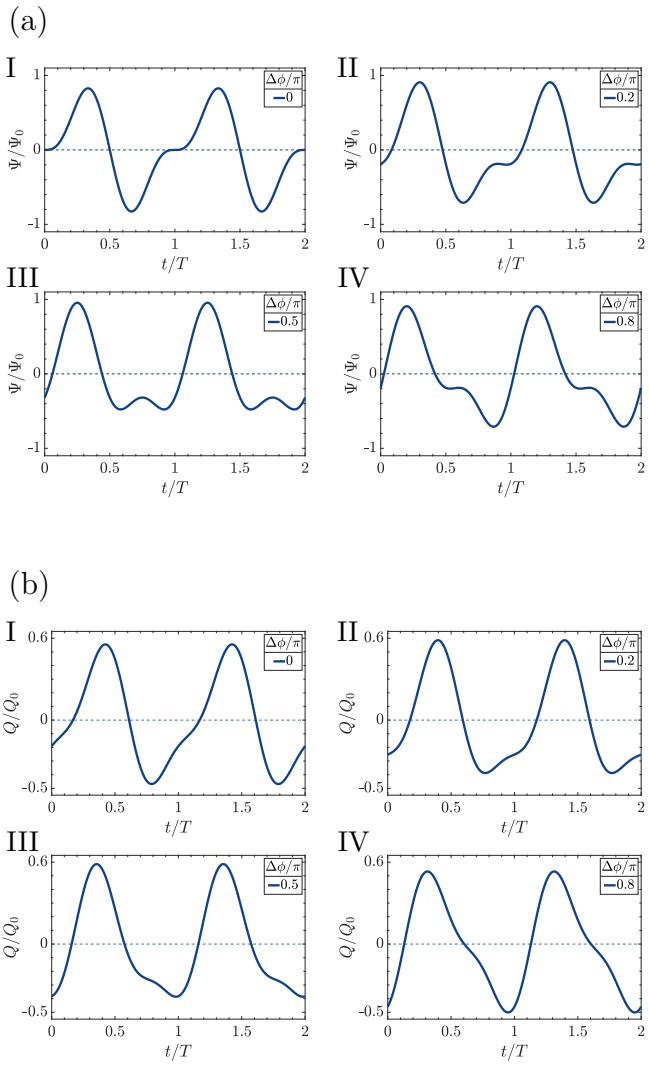

Figure 3.9: (a) Two-term sawtooth voltage of Eq. (3.20) for phase shifts $\Delta\phi/\pi$ equal to (I) 0, (II) 0.2, (III) 0.5, and (IV) 0.8, and (b) the resulting charges accumulating in the capacitors of the equivalent circuit of Fig. 3.4(b).

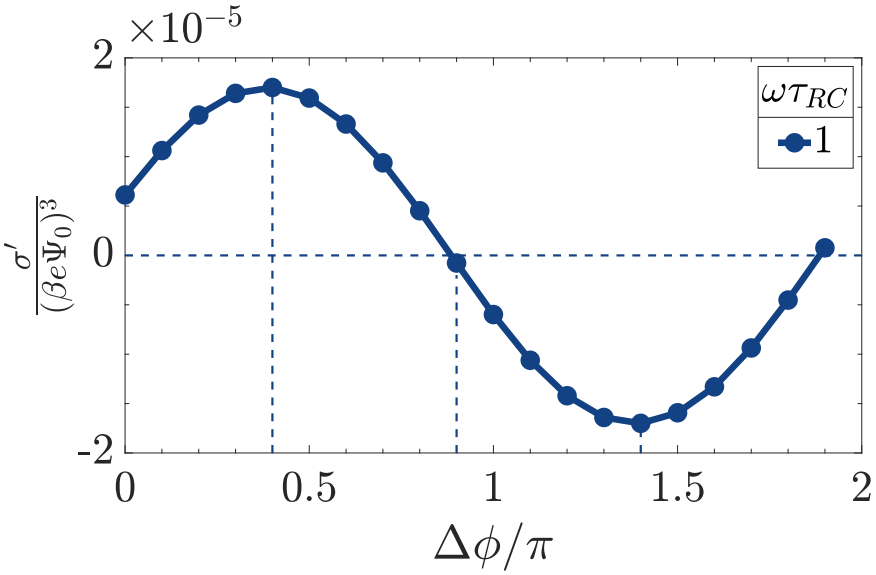

Figure 3.10: Dimensionless and scaled period-averaged surface charge $\sigma'/(\beta e\Psi_0)^3$ as obtained from numerical late-time solutions of the PNP equations for the standard parameter set (see text) as a function of the phase difference $\Delta\phi$ between the two sinusoidal terms of the two-term sawtooth potential of Eq. (3.2) at $\omega\tau_{RC} = 1$. For these parameters the period-averaged surface charge has a maximum at $\Delta\phi = 0.4\pi$ and a minimum (of opposite sign) at $\Delta\phi = 1.4\pi$.

coefficients driven by a sawtooth voltage with the more conventional case of an asymmetric electrolyte (with different ionic diffusion coefficients) driven by a sinusoidal voltage. We focus on the period-averaged electric field profile shown in Fig. 3.3(b) for the present standard parameter set and the equivalent plot shown in Fig.2(b) of Ref. [1] for identical system parameters ($\beta e\Psi_0 = 3$, $\omega\tau_{RC} = 1$, $\kappa L = 50$) at a ratio of ionic diffusion coefficients equal to 2 and 3.5. A striking difference, discussed briefly before, concerns the differences in mirror symmetry with respect to the midplane. Also, for the case of sawtooth driving we see two AREF peaks (a minimum and a maximum) of the same order of magnitude in the Debye-length vicinity of the electrodes, whereas in the case of the asymmetric electrolyte we only obtain a single peak (a

minimum at one electrode and a maximum at the other in agreement with the mirror anti-symmetry). We also note that the scale of the AREF peaks is roughly an order of magnitude larger in the asymmetric case compared to the sawtooth case, however, the latter spreads almost twice as deep into the bulk of the electrolyte.

3.5 SUMMARY AND DISCUSSION

In this work we investigate the time-averaged static electric field generated within the electrolytic cell depicted in Fig. 3.2 when exposed to a sawtooth-shaped AC potential, under the condition of equal diffusion coefficients for monovalent cations and anions, i.e., $D_+ = D_-$. We numerically solve the coupled non-linear Poisson-Nernst-Planck (PNP) equations for ionic diffusion and migration in the cell to examine the dependence of the magnitude of the emerging asymmetric rectified electric field (AREF) on key system parameters. These parameters include the amplitude Ψ_0 of the applied AC sawtooth voltage, the driving frequency ω, the phase shift $\Delta\phi$ between the lowest two harmonic modes of the driving potential, and the system size L, where we note that these system parameters can all be externally tuned without requiring a change of the electrolyte.

The asymmetry in the rate of change of the driving sawtooth voltage induces, despite the equal diffusion coefficients of the cations and anions and despite a zero period-averaged applied voltage, a nonzero period-averaged electrode charge $\langle\sigma\rangle$ that is responsible for a nonzero period-averaged asymmetric rectified electric field (AREF) between the electrodes. While AREF fundamentally represents a non-linear screening phenomenon that we find to be proportional to Ψ_0^3, we could still obtain additional insights by conducting an analysis using the linear RC-circuit of Fig. 3.4(b) that was also used and derived in Ref.[1]. The analytic expression for the time-dependent charge $Q(t)$ on the capacitor of this circuit, in particular the difference between (i) the maximum and the minimum of this charge (represented by Δq) and (ii) the duration of the time-interval of positive and negative charge (represented by Δt), provides a clue on the physics of the nonlinear phenomenon of AREF. These nonzero differences have opposite effects on the the period-averaged charge, which cancels identically even for nonzero Δq and Δt in the case of

linear circuits. However, this cancellation is no longer exact in the nonlinear case of the PNP equations, where an intricate competition between Δq (favoring a net positive charge for our parameter choices) and Δt (favoring a net negative charge) depends sensitively on the system parameters. For driving frequencies ω that are of the same order as the inverse of the characteristic RC-time of electric double layers, i.e., when $\omega\tau_{RC} \sim 1$, this competition between Δq and Δt induces the most prominent period-averaged distribution of ionic charges, which, consequently, results in the largest non-zero AREF structure. The dependence on the system size L is largely reflected by the dependence on the RC-time -which also depends on L. A relatively strong AREF effect of an order of magnitude can be induced by a phase difference $\Delta\phi = \pi/2$ between the two modes of the driving voltage in the two-mode approximation.

Finally, we noted that a recent investigation on floating colloids subjected to AC voltage within an electrolytic cell [69] proposed that apart from AREF also dielectrophoresis (DEP) might also play a role in counteracting the gravitational forces on the colloids, depending on the system parameters. However, the relative contribution of each of these mechanisms to the floating height of the colloids remains an open question. It may well be possible to separate the contributions of the two mechanisms by employing sawtooth potentials, which we have shown here offer substantial opportunities for tuning AREF without the need to change the electrolyte or the colloidal suspension. We hope that this work stimulates experimental work along these lines to manipulate a given electrolyte externally.

4

PRESSURE-GATED MICROFLUIDIC MEMRISTOR

ABSTRACT

A hitherto unexploited characteristic feature of emerging iontronic devices for information processing is the intrinsic mobility of the medium (water), containing charge carriers (ions), which therefore not only responds to voltage but also to pressure. Here we study a microfluidic memristor, in the form of a conical channel, exposed to simultaneously applied time-dependent voltage and pressure drops, through numerical solutions of the Poisson-Nernst-Planck-Stokes equations for ion and fluid transport. We show that the channel's memristive properties can be enhanced, reduced or instantaneously reset by a suitable pressure, and we leverage this finding by two examples of time series processing of simultaneously applied voltage and pressure pulses. We not only show that the distinction between different voltage time series can be improved by enhancing the conductance response with corresponding pressure pulses, but also that the bandwidth of information transfer through the channel can be doubled by letting the pressure pulses represent a second independent time series.

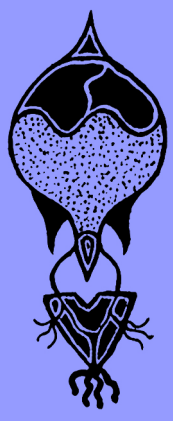

4.1 INTRODUCTION

Memristors (memory-resistors) exhibit a conductance that depends on past current or voltage inputs [84, 85]. They have drawn significant interest, predominantly driven by their ability to emulate neuronal processes in neuromorphic (brain-inspired) circuits [98, 133, 135], which has led to the employment of memristive devices for information processing [136]. For instance, they can emulate weights in neural networks [137] or circumvent the von Neumann bottleneck by co-locating memory and processing as in the brain [112]. These forms of *neuromorphic computing* are considered to be promising candidates for addressing the unsustainably rising energy consumption and the unmanageably large amounts of generated data [134, 136]. For these reasons a diversity of solid-state memristors has by now been explored as possible promising circuit components for neuromorphic and analog computations [85–91, 98, 133, 135].

However, these solid-state memristors for neuromorphic circuits also reveal some fundamental disparities with the brain, which employs ions and molecules in an aqueous environment rather than electrons and holes in a solid semiconductor, thereby utilising chemical regulation as well as multiple information carriers in parallel. These fundamental differences result in tangible challenges, e.g. the fast dynamics of solid-state devices makes them less suited for processing time series with comparatively slower timescales such as biological signals [143]. In order to address this disparity, devices have been proposed that feature electrochemical coupling between (fast) electrons in metallic/semiconducting materials and (slow) dissolved ions/protons [90, 93–98, 138–142]. Interestingly, an emerging class of memristors even operates solely on the basis of aqueous electrolytes without any electronic component [53, 92, 100–111, 145–147]. Various functionalities have recently been extracted from these fluidic iontronic devices, for instance features of synaptic plasticity [148, 149], chemical regulation [53, 145], theoretical proposals of neuron-like spiking [54, 144, 150], implementations for traditional truth tables [151–153], and initial demonstrations of neuromorphic computing [123]. While these results are promising, the advancement of aqueous neuromorphic devices is still in the early stages and more work is required to convert the unique features of iontronics to tangible benefits [154–156].

In this chapter we study iontronic memristors in the form of microfluidic conical channels and leverage the unique property of iontronics that the charge-carrying medium (water) is mobile itself. In response to an applied DC voltage drop, it is well established experimentally and theoretically that conical channels with charged channel walls (i) exhibit ionic current rectification, i.e. the channel conductance depends on the magnitude and the polarity of the applied (static) voltage [114–120], and (ii) act as a pressure-gated transistor because a simultaneously applied pressure drop can strongly affect the electric current [113, 121, 122]. These effects were both quantitatively explained by a theoretical model that describes how the conductance stems from a voltage-dependent steady-state salt concentration profile in the conical channel [122]. This concentration polarisation not only depends on the polarity of the applied voltage but also on the net fluid flow with pressure-induced (Poiseuille-like) and voltage-induced (electro-osmotic) contributions [122]. Recently also the timescale for the voltage-induced build up of concentration polarisation was identified [54], which provided a quantitative explanation for experimentally found memristive effects in conical channels [101–110, 146, 149]. In this chapter we combine these theoretical insights [54, 122] to show that *pulsatile* pressure drops can be combined with AC voltages to not only amplify and reset the memristive properties of a microfluidic conical channel, but also to increase its signalling bandwidth. Although pressure sensors have been integrated into a solid-state device to induce resistive switching [157], pressure sensitivity is not an intrinsic feature of solid-state devices, which usually only allow for pressure signaling via connections to dedicated sensors [132, 158, 159]. In contrast, fluid flow, and hence pressure sensitivity, is an inherent property of fluidic iontronic memristors, therefore the features we present here represent results that we believe will be of relevance across the various emerging iontronic devices.

This chapter will be divided in two parts. Section 4.2 will be devoted to the basics of transport phenomena in microfluidic channels. We will begin by briefly arguing the choice of micrometer scale for microfluidic systems and introducing the equations that we will be using to study such systems. We then give explicit examples of the coupled matter transport in a cylindrical channel. After covering the basics we extend the transport effects to a conical

channel and discuss them in both DC and AC cases, where in the latter case we introduce the notion of memristors. After laying the necessary foundation in section 4.2, section 4.3 will be devoted to studying the pressure gated memristor. Namely, how its memristive effects can be enhanced or suppressed by tuning pressure, while demonstrating potential of such a memristor as a useful tool for neuromorphic computing applications.

4.2 TRANSPORT PHENOMENA IN MICROFLUIDIC CHANNELS

Microfluidic channels, such as the cylindrical one shown in Fig. 4.1, offer excellent opportunities to study coupled transport of matter where, for example, a pressure difference between the reservoirs can create a significant electric current and an electric potential difference can create a significant fluid flow, when the walls of the channel are charged. This is due to the fact, that at this scale surface effects like the influence of the surface charge on the matter transport become significant compared to the volumetric effects.

We use the PNPS equations introduced in section 1.2.2 to describe transport processes in microfluidic channels (where now instead of c, used in the previous chapters and denoting ion concentrations, we use ρ in this chapter):

$$\nabla^2\Psi = -\frac{e}{\varepsilon\varepsilon_0}\rho_e, \tag{4.1}$$

$$\rho_m\frac{\partial \mathbf{u}}{\partial t} = \eta\nabla^2\mathbf{u} - \nabla p - e(\rho_+ - \rho_-)\nabla\Psi; \qquad \nabla\cdot\mathbf{u} = 0, \tag{4.2}$$

$$\mathbf{J}_\pm = -D\left(\nabla\rho_\pm \pm \rho_\pm\frac{e\nabla\Psi}{k_BT}\right) + \rho_\pm\mathbf{u}. \tag{4.3}$$

We recall that Ψ is the electrostatic potential, $\rho_e = \rho_+ - \rho_-$ the ionic charge densities, $\mathbf{J}_\pm$ the ionic fluxes, p pressure, η and $\mathbf{u}$ - fluid viscosity and velocity respectively.

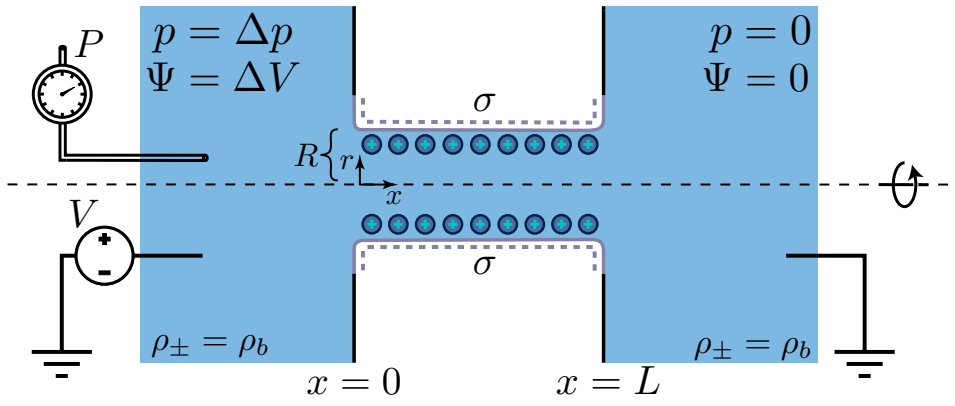

Figure 4.1: Schematic (not to scale) of an azimuthally symmetric cylindrical channel of length L and radius R, connecting two bulk reservoirs of an aqueous 1:1 electrolyte with equal ionic bulk concentration $2\rho_b$. The channel walls carry a negative surface charge density σ. A constant potential drop ΔV and pressure drop ΔP are simultaneously applied across the channel, inducing an electrolyte volume flow Q and an ionic charge current I that we calculate on the basis of Poisson-Nernst-Planck-Stokes equations.

4.2.1 *Transport in a Cylindrical Channel*

To gain a clearer understanding of the coupled nature of transport phenomena in microfluidic channels we begin by examining the simplest scenarios within a long azimuthally symmetric cylindrical channel of length L and radius R depicted in Fig. 4.1. It is described in terms of axial and radial coordinates x and r. The cylindrical channel connects two reservoirs at $x < 0$ and $x > L$. The system is filled with an incompressible 1:1 aqueous electrolyte with ionic bulk concentration $2\rho_b$ in the reservoirs. A uniform surface charge density σ (which will be assumed to be negative throughout this chapter) is imposed on the channel walls, which are assumed to be impermeable, effectively excluding Faradaic processes. Consequently, mobile

cations and anions accumulate to form an electric double layer within the channel. Additionally we assume the channel to be long $L \gg R$, where $R \gg \lambda_D$.

Poiseuille Flow

One of the simplest matter transport effect is the so-called Pouseuille flow, where the electrolyte is pushed through the cylindrical channel of Fig. 4.1 by applying a pressure difference to the reservoirs (the potential difference is kept zero in this case $\Delta V = 0$). We assume $P = \Delta P$ in the left reservoir, whereas the right one is at $P = 0$. The pressure difference will generate liquid flow, whose profile can be calculated using Stokes equation (4.2) with no body force $\eta\nabla^2 u_x(r) - \nabla p(r) = 0$. Since $\mathrm{d}p/\mathrm{d}x = -\Delta p/L$ =const., the Stokes equation in cylindrical coordinates reduces to

$$\frac{1}{r}\partial_r\Big(r\partial_r u_x(r)\Big) = -\frac{1}{\eta}\frac{\mathrm{d}p(x)}{\mathrm{d}x}, \tag{4.4}$$

which after double integration yields

$$u_x(r) = \frac{r^2}{4\eta}\frac{\mathrm{d}p(x)}{\mathrm{d}x} + C_1 \ln r + C_2, \tag{4.5}$$

where C_1 and C_2 are integration constants. Using the no-slip boundary condition $u_x(r = \pm R) = 0$, we arrive at the Pouseuille flow profile

$$u_x(r) = -\frac{1}{4\eta}\frac{\mathrm{d}p(x)}{\mathrm{d}x}(R^2 - r^2), \tag{4.6}$$

characterized by the parabolic shape and peaking at the center of the channel $r = 0$. Poiseuille flow, while being an example of matter transport, is still not an example of a **coupled** matter transport, as the unit of pressure [energy/volume] directly corresponds to that of the fluid transport - [volume/time].

Electroosmosis

Another simple case of matter transport takes place when we apply a potential difference ΔV between the reservoirs, which, due to presence of ions

in the electrolyte will drive electric current through the cylindrical channel. However, it is the presence of EDLs at the walls of the channel that makes matter transport more interesting in this case. The excess of counterions in the EDLs breaks the balance of mobile ion numbers in the channel. This allows the potential difference ΔV to create a net ion current along the channel, which, in turn, drags the fluid along, creating a fluid flow. Thus the applied electric potential difference does not only drive an electric current in the system but also a fluid flow. This is precisely an example of a coupled transport phenomenon, as the unit of electric force source, the potential difference [energy/charge], does not only create an electric current with the unit of [charge/time], but also a fluid flow with the unit of [volume/time].

In this case combining the Stokes equation with the Poisson equation leads to

$$\eta \nabla^2 \mathbf{u} = \varepsilon \varepsilon_0 (\nabla^2 \Psi) \mathbf{E}, \tag{4.7}$$

where $\mathbf{E} = (E_x, 0, 0) = -\nabla \Psi$, which in conjunction with the symmetry and incompressibility arguments similar to those that we used in the Poiseuille flow case results in $\mathbf{u} = (u_x(r), 0, 0)$. Integrating the equation twice yields

$$u_x(r) = \frac{\varepsilon \varepsilon_0 E_x}{\eta} (\Psi(r) - \Psi(R)), \tag{4.8}$$

where $\Psi(R)$ is the surface (zeta) potential, whereas $\Psi(r)$ is the PB potential in the cylindrical case. Here we assumed a thin-EDL limit $R \gg \kappa^{-1}$, for which the curvature of the channel can be neglected and $\partial_r^2 \Psi + (1/r)\partial_r \Psi \approx \partial_r^2 \Psi$ in the EDL at the wall. From Eq. (4.8) it is clear that the velocity of the fluid is only going to vary in the vicinity of the walls, as far from the walls $R - r \gg \kappa^{-1}$ the electric potential vanishes $\Psi(r) = 0$ due to being screened by the EDLs. In the bulk of the channel fluid thus reaches the so-called "slip velocity"

$$u_{x,s} = -\frac{\varepsilon \varepsilon_0 \Psi(R)}{\eta} E_x \tag{4.9}$$

Due to the flow profile being flat in the channel while slipping at the walls, the Electroosmotic flow is called a "Plug Flow".

Streaming Current

One might wonder here, if an external electric field can drive not only the electric current in the channel, but also the fluid flow, can the external pressure be driving the electric current alongside pushing fluid through the channel? The answer turns out to be positive, as if we look at the Poiseuille flow at the walls, its velocity is non-zero $u_x|_{r\to R} = -\frac{1}{4\eta}\frac{\mathrm{d}p}{\mathrm{d}x}R^2$. Therefore the ions in the EDL get dragged along the flow creating the so-called streaming current

$$I_s = -2\pi\int_0^R \mathrm{d}r r\varepsilon\varepsilon_0 u_x(r)\nabla^2\Psi = \frac{\pi\varepsilon\varepsilon_0 R^2}{2\eta}\frac{\mathrm{d}p}{\mathrm{d}x}\Psi(R) \tag{4.10}$$

where we used Poisson and Stokes equations, together with the thin-EDL limit and $\Psi(R) = 0$ due to screening. This is another example of a coupled transport. Thus, we see, that in microfluidic devices, where surface effects play a comparable role to that of the volume effects, a variety of interesting matter transport phenomena arise.

Note on Voltammetry in the Cylinder

Finally, it is also important to note here, that the electric current created in the above transport phenomena has a linear dependence on the applied potential difference ΔV, ensuring the ohmic reponse of the channel to the applied voltage, as seen in Fig. 4.2, where the steady state current amplitude depends on the driving voltage in a linear way, characteristic for the Ohm's law $V = IR$, with R being resistance of the system.

4.2.2 *Transport in a Conical Channel*

After getting a general idea about the simplest cases of transport phenomena in the cylindrical channel, we now turn our attention to a conical channel shown in Fig. 4.3. In contrast to the cylindrical case, the conical channel breaks the symmetry of the system by having unequal base and tip radii $R_b > R_t$.

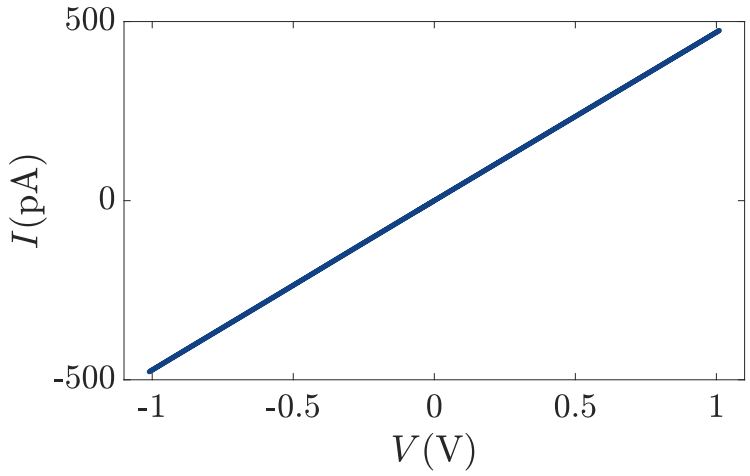

Figure 4.2: Current-voltage relation for a cylindrical channel of length $L = 9.8\,\mu$m, radius $R_b = 441\,$nm at room temperature $T = 293\,$K, containing a $1:1$ electrolyte with viscosity $\eta = 1\,$mPas, mass density $\rho_m = 1\,$kg/L, dielectric constant $\varepsilon = 80$, default bulk salt concentration $\rho_b = 1\,$mM with a Debye screening length $\lambda_D \simeq 9.8\,$nm and ionic diffusion coefficient $D = 1\,\mu\text{m}^2/\text{ms}$. The surface charge applied to the blocking walls of the channel is set to $\sigma \approx -3.4\,\text{mC/m}^2$. We impose a static voltage in the range of $V = (-1, 1)$(V) and pressure that scales linearly with voltage and has a magnitude of $P = \mp 60$(mbar) at $V = \pm 1$(V). We observe a linear current-voltage relation corresponding to the Ohmic case.

Static Voltage and Pressure

As it was briefly mentioned in the introduction, it is well established experimentally and theoretically that when a conical channel with charged walls is driven by an applied DC voltage drop, it (i) exhibits ionic current rectification [114–120], implying that the channel conductance depends on the magnitude and the polarity of the applied (static) voltage. At the same time it also (ii) acts as a pressure-gated transistor because a simultaneously applied pressure drop can strongly affect the electric current [113, 121, 122]. These effects were both quantitatively explained by a theoretical model that describes how the conical channel conductance change stems from a voltage-

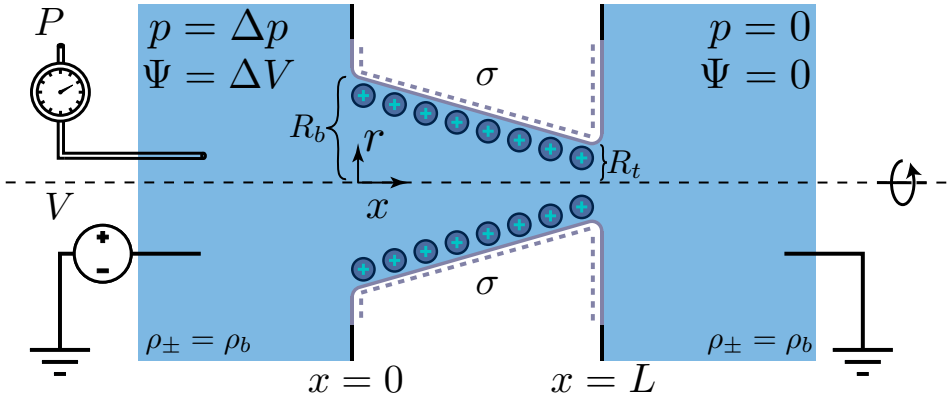

Figure 4.3: Schematic (not to scale) of an azimuthally symmetric conical channel of length L, base radius R_b, and tip radius $R_\mathrm{t} < R_\mathrm{b}$, connecting two bulk reservoirs of an aqueous 1:1 electrolyte with equal ionic bulk concentration $2\rho_\mathrm{b}$. The channel walls carry a negative surface charge density σ. A static potential drop ΔV and pressure drop ΔP are simultaneously applied across the channel, inducing an electrolyte volume flow Q and an ionic charge current I that we calculate on the basis of Poisson-Nernst-Planck-Stokes equations, yielding a pressure-tunable electric conductance $g = I/V$.

dependent steady-state salt concentration profile buildup in it [122]. This concentration polarisation not only depends on the polarity of the applied voltage but also on the net fluid flow with pressure-induced (Poiseuille-like) and voltage-induced (electro-osmotic) contributions [122]. Here we are going to briefly outline the main findings of Ref. [122] and explain the mechanisms behind both of the observed effects.

The system of interest, illustrated in Fig. 4.6, with experimentally realistic parameters, comprises a long azimuthally symmetric conical channel, with axial and radial coordinates x and r, of length $L = 9.8\,\mu$m, a base radius $R_b = 446\,$nm in the plane $x = 0$, and a tip radius $R_t = 98\,$nm in the plane $x = L$. Its cross section radius reads $R(x) = R_b - (x/L)(R_b - R_t)$ for

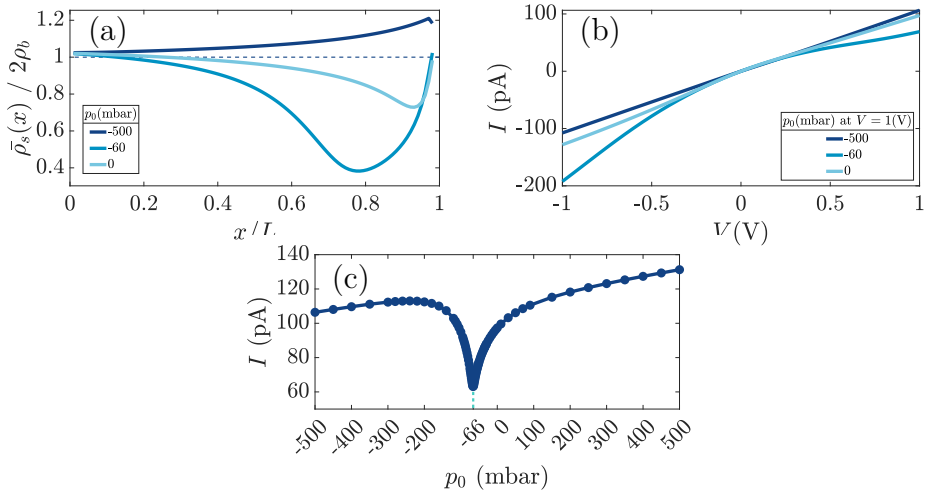

Figure 4.4: In (a) we plot the dimensionless cross-sectional average of the salt density $\bar{\rho}_s(x)$ along the rescaled channel coordinate x/L for $V = 1$(V) voltage and three different pressures $P = -500, -60, 0$(mbar). The density curve at high pressure is the closest to the flat dashed line of homogeneous salt distribution along the channel. Significantly more homogeneity is introduced at zero pressure, whereas the highest level of inhomogeneity is achieved at a certain intermediate pressure $P = -60$(mbar). In (b) the current-voltage relation in the same channel is plotted. Pressure scales linearly for each value of voltage $P = \mp(500, 60, 0)$(mbar) when $V = \pm 1$(V). Similarly to (a) the highest level of current rectification is observed at the intermediate pressure, whereas in the high-pressure case the IV relation is linear. In (c) the current is plotted against pressure magnitude for $V = 1$(V). We see a linear change in current at large pressures, however, as we approach the optimal pressure at around $P = -60$ (mbar), the current magnitude quickly drops forming a sharp minimum. For parameters see text.

$x \in [0, L]$. The channel connects two incompressible aqueous 1:1 electrolyte reservoirs at $x < 0$ and $x > L$, each at equal ionic bulk concentration $2\rho_b$ at room temperature $T = 293\,\mathrm{K}$, viscosity $\eta = 1\,\mathrm{mPas}$, mass density $\rho_m = 1\,\mathrm{kg/L}$, dielectric constant $\varepsilon = 80$, default bulk salt concentration

$\rho_b = 1\,\mathrm{mM}$ and ionic diffusion coefficient $D = 1\,\mu\mathrm{m}^2/\mathrm{ms}$. The walls of the channel carry a homogeneous surface charge density σ, such that the pointlike and mobile cations and anions form an electric double layer in the channel. The channel walls are blocking and we exclude Faradaic processes. The surface charge is set to $\sigma \approx -3.4\,\mathrm{mC/m}^2$, which yields an equilibrium zeta potential of 40 mV to mimic a silica surface in contact with an aqueous 1 : 1 electrolyte with a Debye screening length $\lambda_D \simeq 9.8\,\mathrm{nm}$ [124]. Note that the channel dimensions, which are in the regime of weak double-layer overlap since $\lambda_D \ll R_t$, satisfy $R_t/R_b = 0.22$, found to be optimal for current rectification [122]. On the far side of both reservoirs we impose fixed ionic bulk concentrations of $\rho_\pm = \rho_\mathrm{b} = 1\,\mathrm{mM}$. We impose a static voltage $V = 1(\mathrm{V})$ and pressure $P = -500, -60, 0(\mathrm{mbar})$ at the far side of the reservoir connected to the base, while the far side of the tip reservoir is grounded and at (arbitrary) reference pressure zero. This will be a standard set of parameters that we will use throughout this chapter, unless stated otherwise.

The above-mentioned channel features lead to an electric potential profile $\Psi(x, r, t)$, a pressure profile $p(x, r, t)$, a fluid flow with velocity field $\mathbf{u}(x, r, t)$, and ionic fluxes $\mathbf{J}_\pm(x, r, t)$. To resolve the fluid and ionic dynamics in the channel we solve the full set of Poisson-Nernst-Planck-Stokes (PNPS) equations for diffusive, conductive, and advective transport

$$\nabla^2\Psi = -\frac{e}{\varepsilon_0\varepsilon}(\rho_+ - \rho_-\Big), \tag{4.11}$$

$$\frac{\partial\rho_\pm}{\partial t} = -\nabla\cdot\mathbf{J}_\pm, \tag{4.12}$$

$$\mathbf{J}_\pm = -D\left(\nabla\rho_\pm \pm \rho_\pm\frac{e\nabla\Psi}{k_\mathrm{B}T}\right) + \mathbf{u}\rho_\pm, \tag{4.13}$$

$$\eta\nabla^2\mathbf{u} = \nabla p + e(\rho_+ - \rho_-)\nabla\Psi; \qquad \nabla\cdot\mathbf{u} = 0. \tag{4.14}$$

The Poisson Eq. (4.11) accounts for electrostatics. The conservation of ions is ensured through the continuity Eq. (4.12), while the ionic fluxes are assumed to be described by the Nernst-Planck Eq. (4.13), which combines Fickian diffusion, Ohmic conduction, and Stokesian advection. Finally the force

balance on the (incompressible) fluid is described by the Stokes Eq. (4.14). To close the system of Eqs (4.11)-(4.14) we impose no-slip, no-flux, and Gauss' law boundary conditions on the walls of the system, i.e. $\mathbf{u} = 0$, $\mathbf{n} \cdot \mathbf{J}_{\pm} = 0$, and $\mathbf{n} \cdot \nabla \Psi = -\sigma / \varepsilon_0 \varepsilon$, respectively, with $\mathbf{n}$ the wall's inward normal vector. The PNPS equations can be solved numerically using finite-element methods of COMSOL® to reproduce the results of Ref. [122], albeit for a different parameter set, presented in detail above.

The conductance of the conical channel can only be varied by changing the amount of charge carriers (ions) inside the channel. Therefore, to uncover the reason for the pressure sensitivity of the conductance, ref. [122] employed the cross-sectional averaged salt concentration $\bar{\rho}_s(x)$, where $\rho_s(x, r) \equiv \rho_+(x, r) + \rho_-(x, r)$. It is a measure for the salt concentration at position x and when averaged laterally, $\langle \bar{\rho}_s \rangle$ determines the conductance of the channel g. From numerical calculations it was established that the radial variation of the salt concentration inside the channel (outside of EDLs) is weak, agreeing with Ref.[170], making $\bar{\rho}_s(x)$ an appropriate choice for the task at hand. In Ref. [122], the PNPS system of equations was solved for salt concentration profiles both analytically (within approximations) and numerically. Here, however, we are only going to re-create and discuss the numerical results (albeit for our parameter set) of Ref. [122], in order to explain the main findings.

We start with the density profiles. In Fig. 4.4(a) the re-scaled average density profile $\bar{\rho}_s(x)/2\rho_b$ is plotted as a function of x coordinate in the channel for three values of pressure from the standard parameter set $P = -500, -60, 0$(mbar) at $V = 1$(V) voltage. We see that when the pressure magnitude is high, $P = -500$(mbar), the density profile is deviating only a bit from the bulk density at the tip of the channel. If we remove the pressure completely $P = 0$(mbar), there is a more pronounced deviation of the density profile from the bulk density. However, the largest deviation is seen when the pressure has an intermediate value $P = 60$(mbar) (for the standard parameter set).

As the change in the average salt density $\bar{\rho}_s(x)$ inside the channel gets reflected in the conductance of the channel g, any change in $\bar{\rho}_s(x)$ leads to the deviation of the current-voltage IV curve from the Ohmic linear relation, resulting in electric current rectification as seen in Fig. 4.4(b), where we plot the magnitude of the electric current flowing through the channel against the

amplitude of the driving voltage. Three curves are plotted for different values of pressure, which is scaled linearly with voltage amplitude in such a way that it reaches $P = -500, -60, 0$(mbar) at $V = 1$(V) voltage. We see that while the high-pressure curve is clearly linear i.e. Ohmic, when there is no pressure applied to the channel there is some degree of current rectification to be seen. However, as one could have expected from the salt concentration profiles of Fig. 4.4(a), the maximal current rectification is achieved at the intermediate pressure, for which the density profile deviated the most from the bulk density.

According to Ref.[122] this happens due to a competition between the salt fluxes at the tip and at the base. Salt fluxes created by the electric field are determined by the $(\rho_+ - \rho_-)\frac{e\nabla\Psi}{k_B T}$ term of Eq. (4.3) i.e. by the density of the excess free charge carriers and the strength of electric field. The former scales inversely proportional to the circumference of the channel cross section $\sim 1/R(x)$, as the excess of ions is only observed in the EDLs, which are located along the circumference of channel's cross section. On the other hand, the number of the electric fieldlines within the cone is conserved, resulting in their density, and as a consequence the strength of the electric field, to scale as the inverse of the surface area of channel cross-section i.e. as $\sim 1/R(x)^2$. Thus, if the system is driven by a positive voltage and the surface charge is negative, the ionic charge in the EDL will be positive and the salt current going out of the tip will be stronger than the one entering the base, leading to the depletion of ions close to the tip of the channel, as seen in Fig. 4.4(a). Reversing the sign of the driving voltage will lead to accumulation rather than depletion of salt close to the tip of the channel.

The reason why the salt depletion/accumulation is the strongest at a certain intermediate pressure is, however, connected to the coupled matter transport. Earlier in this chapter we saw that besides creating an electric current, the laterally applied voltage also creates a fluid flow. Therefore, according to Ref.[122], whatever salt profile was built up by the applied voltage keeps getting flushed by the electroosmotic flow generated by the same voltage. Therefore, if alongside the voltage the system is also driven by pressure with its modulus tuned such that it creates a Poiseuille counterflow of the same magnitude as the electroosmotic one, there will be no net fluid flow in the system and the salt profile will have the optimal conditions to

fully develop, as there will be no flow flushing it continuously. Precisely for this reason we see the highest deviation from the bulk density at the intermediate value of $P = -60$(mbar), for $V = 1$(V) as in this case the net fluid flow Q defined as

$$Q(t) = \int_0^{R(x)} \mathbf{u}(x, r, t) \cdot \hat{\mathbf{x}} 2\pi r \mathrm{d}r \tag{4.15}$$

in the system approximately vanishes. For the further discussions on the optimal fluid flow for a given voltage and derivation of its expression, as well as the optimal dimensions of the channel we refer the reader to Ref.[122]. Presence of an optimal pressure for current rectification also explains its the sensitivity with respect to the applied pressure amplitude. In Fig. 4.4(c), where the current amplitude is plotted against the pressure amplitude for a voltage of $V = 1$(V), we see a linear increase in current at large pressure amplitudes, however, as we approach the optimal pressure at around $P = -60$ (mbar), the current magnitude quickly drops forming a sharp minimum.

Harmonic Voltage with No Pressure

The salt concentration buildup does not, however, take place instantaneously. For a purely voltage driven process, the typical salt concentration polarisation timescale was found to be well-estimated by [54, 125]

$$\tau = \frac{L^2}{12D}, \tag{4.16}$$

which results in a voltage-dependent conductance memory retained over a time $\sim \tau$. Here $\tau = 8.33\,\mathrm{ms}$ for the present parameters.

The conductance memory was found to influence the voltammetry in a conical channel driven by time-dependent applied voltage, revealing the emergence of a hysteresis loop [54, 100–111] as plotted in Fig. 4.5. We see, that for every value of voltage there are two corresponding values of the electric current magnitude, forming two hysteresis loops which interstect at the origin when $V = 0$ and $I = 0$. In the above studies the system was driven by a harmonic voltage drop given by $V(t) = V_0 \sin(\omega t)$ at the judiciously chosen frequency of $\omega/2\pi = 25\,\mathrm{Hz}$, where $\omega\tau \simeq 1.3$ is close to unity and

therefore close to the optimal frequency for observing hysteretic properties [160]. In short emergence of the hysteresis loop can be explained as follows: as the voltage changes, the salt profile has to adjust to it accordingly, however, due to frequency being comparable to the characteristic time τ, there is not enough time for salt to fully form its profile that would correspond to the instantaneous voltage value. Thus, depending on the direction of voltage change, whether it is going from the negative values to the positive ones or the other way around, the salt profile ends up being different at the same instantaneous voltage value. This results in two values of channel conductance and, consequently, of the electric current magnitude (as a result of current rectification) for the same instantaneous voltage value, leading to the hysteresis loop that we observe in the plot.

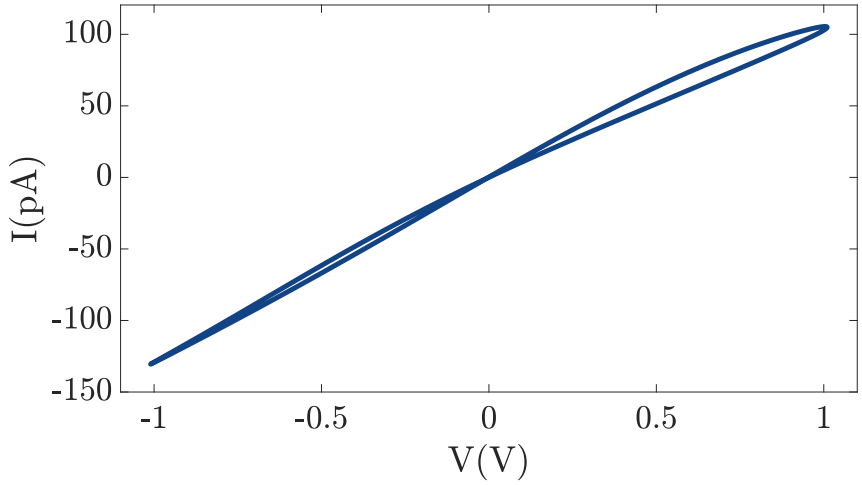

Figure 4.5: Current-voltage hysteresis loop of a conical channel for the same parameters as in Fig. 4.4 with the difference that voltage is harmonic $V = V_0 \sin(\omega t)$ and pressure is assumed to be zero. Here $\omega/2\pi = 25\,\text{Hz}$ is judiciously chosen so that $\omega\tau \simeq 1.3$ is close to unity maximizing the hysteretic properties of the IV curve [160]. We see that the memory of conductance turns the Ohmic curve of Fig. 4.2 into a hysteresis loop with a pinch at the origin. Devices producing such curves are called memristors (memory-resistors) [84, 85].

Devices producing hysteresis loops that are pinched in the origin, i.e. $I = 0(\mathrm{A})$ when $V = 0(\mathrm{V})$, similar to Fig. 4.5, are called memristors (memory-resistors) [84, 85] due to the memory of the system resistance (conductance). Such devices have recently gained a lot of attention due to their ability to simulate neuromorphic processes, as we mentioned in the introduction. Therefore, amplifying their "memristance", which we characterize by the area enclosed by the hysteresis loop, can lead to improvements in neuromorphic computing.

Up to this point studies on conical channels in the dynamic case have concentrated only on the voltage as a driving force [54, 100–111], however, as we saw in the previous section with the static voltage, adding pressure as a second driving force can amplify/suppress the current rectification. Therefore, we want to see, whether the results of the static case with pressure being able to amplify/suppress the current rectification could be employed to achieve the same effect with the memristance when the harmonic voltage is augmented by the harmonic pressure. This is what we are going to investigate in the following section.

4.3 HARMONIC VOLTAGE AND PRESSURE - TUNING CONE CONDUCTANCE

Combining the results of the previous section, we now make both voltage and pressure time-dependent to see, if the pressure sensitivity can be carried over to the time-dependent case amplifying/suppressing memristance and how this sensitivity can be employ to achieve various interesting effects like memory reset and information transfer.

Of particular interest here is the time-dependent electric current $I(t) = 2\pi e \int_0^{R(x)} \left(\mathbf{J}_+(x,r,t) - \mathbf{J}_-(x,r,t)\right) \cdot \hat{\mathbf{x}} r dr$, with $\hat{\mathbf{x}}$ the unit vector in the positive x-direction, and volume fluid flow $Q(t)$, driven through the channel by a simultaneously applied time-dependent potential $V(t)$ and pressure $P(t)$. Numerically we find that the capacitance of the channel is so small that the x-dependence of $I(t)$ is negligible (see Appendix 4.5). The charge flux $\mathbf{J}_+ - \mathbf{J}_-$, from which the current follows, depends on the channel salt concentration $\rho_+ + \rho_-$, which can be (dynamically) increased or decreased

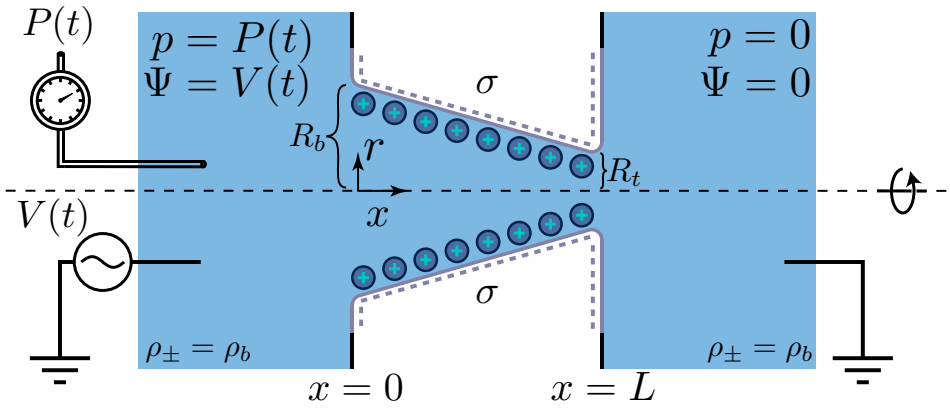

Figure 4.6: Schematic (not to scale) of an azimuthally symmetric conical channel of length L, base radius R_b, and tip radius $R_\mathrm{t} < R_\mathrm{b}$, connecting two bulk reservoirs of an aqueous 1:1 electrolyte with equal ionic bulk concentration $2\rho_\mathrm{b}$. The channel walls carry a negative surface charge density σ. A time-dependent potential drop $V(t)$ and pressure drop $P(t)$ are simultaneously applied across the channel, inducing an electrolyte volume flow $Q(t)$ and an ionic charge current $I(t)$ that we calculate on the basis of Poisson-Nernst-Planck-Stokes equations, yielding a pressure-tunable time-dependent electric conductance $g(t) = I(t)/V(t)$, that can be used to transfer information.

by (simultaneously) applied potential and pressure drops [54, 122]. As it was already mentioned, for a purely voltage driven process, the typical salt concentration polarisation timescale was found to be $\tau = 8.33\,\mathrm{ms}$ for the present parameters, which results in a voltage-dependent conductance memory retained over a time $\sim \tau$. However, steady-state salt concentration polarisation also strongly depends on the fluid flow field [122], which develops much faster as we will see. Therefore we expect that the dynamic voltage-dependent conductance can be tuned by a quasi-instantaneous response of the fluid flow to an applied pressure drop $P(t)$. To investigate the resulting interesting interplay between voltage and pressure drop $V(t)$ and $P(t)$, we numerically solve the PNPS equations using finite-element methods of COMSOL®.

We first study harmonic voltage- and pressure drops given by $V(t) = V_0 \sin(\omega t)$ and $P(t) = P_0 \sin(\omega t)$ at the judiciously chosen frequency of $\omega/2\pi = 25\,\mathrm{Hz}$, where $\omega\tau \simeq 1.3$ is close to unity and therefore close to the optimal frequency for observing memristive properties [160]. We fix $V_0 = 1\,\mathrm{V}$ and consider a variety of pressure amplitudes P_0. In Fig. 4.7(a) we plot the limit cycle of the parametric $I(t)$-$V(t)$ curve for $P_0 = 0$ (red) and $P_0 = -60\,\mathrm{mbar}$ (blue). For both pressures the current-voltage relation features a characteristic pinched hysteresis loop, with a closed loop at either voltage polarity and a crossing in the origin [130]. However, the total area of the closed loop, a measure for the strength of the memristive effect, is seen to be much more pronounced for the non-zero pressure drop. The inset of Fig. 4.7(a) quantifies this by showing the P_0-dependence of the area of the hysteresis loop, featuring a well-defined peak at about $P_0 = -60\,\mathrm{mbar}$, where the area is enhanced by a factor larger than three compared to that at $P_0 = 0$; by contrast, the area is reduced compared to $P_0 = 0$ for $P_0 > 0$ and $P_0 < -140\,\mathrm{mbar}$, where a strong fluid flow washes out salt concentration polarisation and hence any significant conductance memory [121, 122]. Note that the zero-flow condition, $Q = 0$ as indicated in the inset at $P_0 \simeq -82\,\mathrm{mbar}$, is close to the maximum, however not spot on. Nevertheless, the basic intuition that a static pressure washes out concentration polarisation or cancels the electro-osmotic fluid flow, thereby enhancing concentration polarisation, as detailed in section 4.2.2 and Ref. [122], largely carries over to the time-dependent regime. This is because the typical timescale for developing a Poiseuille-like velocity profile in a cylinder of radius R, as

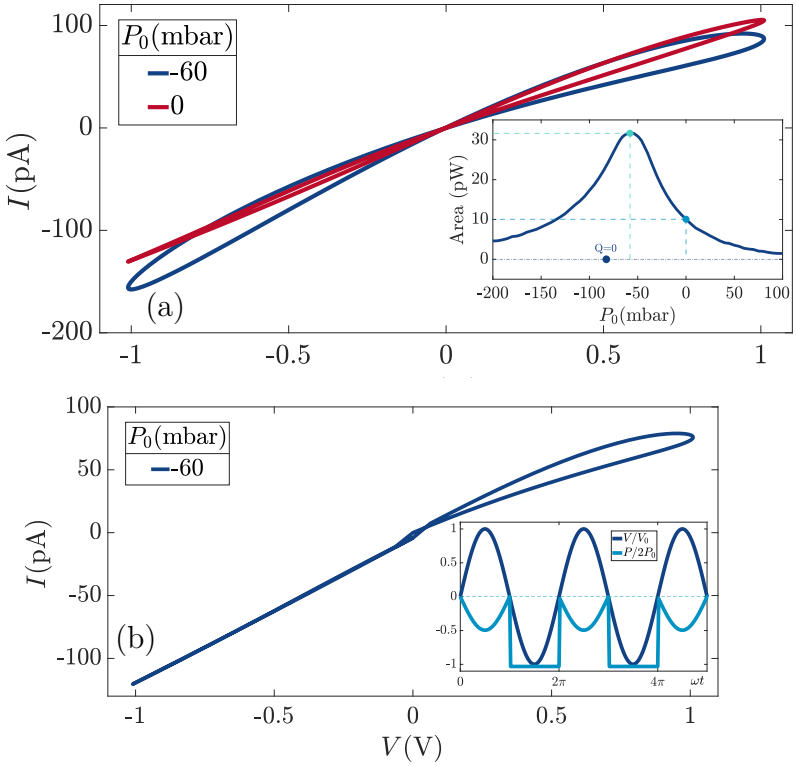

Figure 4.7: Current-voltage hysteresis loops of a conical channel, for our standard parameter set (see text), driven by a harmonic voltage drop (amplitude $V_0 = 1$ V and frequency 25 Hz) combined with a simultaneously applied pressure-drop. **(a)** The pressure drop is also harmonic with amplitudes $P_0 = -60$ mbar (blue) and $P_0 = 0$ (red), the inset showing the dependence of the area enclosed by the hysteresis loop on P_0. **(b)** The applied pressure $P(t)$, shown in the inset, equals $P_0 \sin(\omega t)$ with $P_0 = -60$ mbar as in (a) if $V(t) > 0$ and a constant -120 mbar if $V(t) < 0$, such that the memristive response at $V(t) > 0$ is reset into an Ohmic response at $V(t) < 0$.

obtained from Stokes' Eq. (4.2), is given by $\tau' = R^2/(\eta/\rho_m)$, which equals $\tau' = 0.2\,\mu$s for $R = R_b$ and is therefore many orders of magnitude smaller than

τ and $1/\omega$. Therefore the fluid flow is essentially established instantaneously with pressure and acts very similar to a quasi-static flow [131].

Interestingly, besides allowing for manipulations of the memristance of a conical channel by applying pressure drops, the major difference between the characteristic timescales τ for ionic relaxation and $\tau' \ll \tau$ for momentum relaxation allows also for applications of pressure as a memory reset tool. This is illustrated in the current-voltage characteristic of Fig. 4.7(b) for the same system parameters and the same sinusoidal voltage $V(t)$ as in Fig. 4.7(a), however with a sinusoidal pressure $P(t) = P_0 \sin(\omega t)$ with $P_0 = -60$ mbar only if $V(t) > 0$, and a constant pressure $P(t) = -120$ mbar if $V(t) < 0$, as plotted in the inset. This protocol for $P(t)$ reduces the flow and thus enhances the conductance memory (as shown in Fig. 4.7(a)) only for $V(t) > 0$, while it increases the flow and washes out the concentration polarisation for $V(t) < 0$, when it turns the channel essentially into an Ohmic conductor without conductance memory. Therefore, the pressure-induced flow for $V(t) < 0$ acts as a memory eraser. The time-scale of the memory reset process is of order τ' and is therefore essentially instantaneous on the relevant memristive and electric time scales τ.

Inspired by Refs. [123, 126, 128, 129], where memristors were shown to distinguish time series in the form of voltage pulses, we now study simultaneously applied voltage- and pressure pulses of magnitude $V_0 = \pm 1\,\mathrm{V}$ and $P_0 = \mp 60\,\mathrm{mbar}$, which we expect to optimise the electric response on the basis of our results of Fig. 4.7, and we show this to yield and enhanced response compared to only voltage pulses with $P_0 = 0$. We focus on trains of four of these pulses, all four of equal duration $\tau/8$ and all four preceded by a zero-voltage and zero-pressure interval of duration $\tau/8$, such that a train of four pulses together takes a total time τ. By assigning a binary "0" and "1" to a negative and positive pulse, respectively, a train of four pulses can represent any of the 16 binary numbers between 0000 and 1111. For each of the 16 possible trains, described by block signals $V(t)$ and $P(t)$, we solve the PNPS Eqs. (4.1)-(4.2) for our standard parameter set and calculate the electric conductance $g(t) = I(t)/V(t)$ of the channel at $4t/\tau = 0, 1, 2, 3$, and 4, so at the end of each pulse and at the start, to find $g(0)$. In Fig. 4.8(a) we plot the resulting normalised channel conductance $g(t)/g(0)$ for the two pulse trains representing 0000 and 1111, both at $P_0 = -60\,\mathrm{mbar}$ (solid lines)

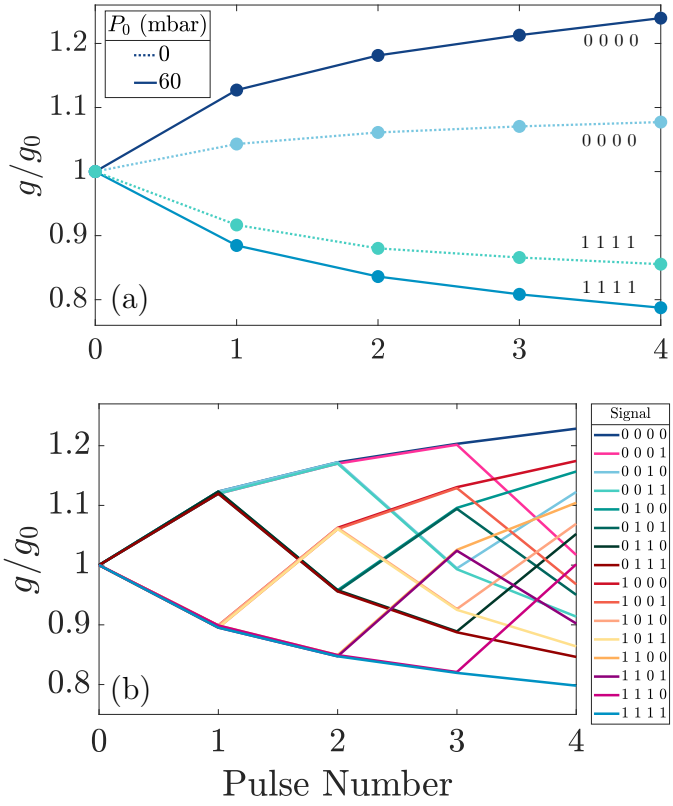

Figure 4.8: Relative channel conductance $g(t)/g(0)$ at $4t/\tau = 0, 1, 2, 3, 4$ during a train (of duration τ) of four voltage pulses, in (a) for the extremes of four positive (1111) and four negative (0000) voltage pulses, without (dashed line) and with (solid line) a simultaneously applied train of four pressure pulses and in (b) for all 16 combinations of four positive/negative voltage pulses with negative/positive simultaneous pressure pulses leading to a relatively wide range of 16 distinguishable conductances after the fourth pulse (see text).

and $P_0 = 0$ (dashed). We observe, in agreement with our earlier findings, that negative/positive voltages increase/decrease the channel conductance, both for finite and zero pressure. However, the effect of the carefully chosen

finite pressure $P_0 = -60\,\mathrm{mbar}$ considerably increases the range of achieved conductances. In Fig. 4.8(b) we again show $g(t)/g(0)$ at the very end of each of the four pulses, but now only for $P_0 = -60\,\mathrm{mbar}$ and for all 16 possible trains. We see that each train, i.e. each bit string, is mapped onto a unique conductance $g(\tau)/g(0)$ that lies in between the two extreme ones of 0000 and 1111 (shown already in Fig. 4.8(a)). The 16 unique conductances shown in Fig. 4.8(b) are considerably closer to each other if only voltage pulses are used (see Appendix 4.5), therefore the pressure pulses significantly enhance the channel's capacity for distinguishing these time series.

Clearly, the pressure-induced widening of the conductance window enhances the separation of the different conductances $g(\tau)/g(0)$, which should facilitate their mutual distinction in conductance measurements of experimental realisations of these channels. In line with Ref. [123], where a colloid-filled tapered microchannel was employed as a synaptic device for reservoir computing with voltage-only pulses, an enhanced window of conductances and longer trains could be employed to increase the performance and computational capacity of the device or to decrease the number of required channels per computation.

Instead of tuning the channel conductance by applying the pressure pulses according to the voltage pulses, we can also decouple voltage and pressure signals and use them as independent driving forces, for instance as independent (but simultaneous) pulses of magnitude $\pm(V_0, \pm P_0)$. Fig. 4.9(a) explicitly shows that in this case only two rather than four pressure- and voltage pulses are required to arrive at 16 combinations. For all 16 combinations we calculate the conductance after the first and second block pulse using the same pulse and train protocol as before, however with slightly longer pulses and separation intervals of 0.15τ (rather than $\tau/8$ in Fig. 4.8(b)) such that the present train of two pulses only takes a time 0.6τ (rather than τ). The result is shown in Fig. 4.9(b) and indeed reveals 16 distinct values of the conductance after the second pulse, with a window and a degree of separation that is very similar to that of Fig. 4.8(b). Apart from a similar resolution as obtained for the 4-pulse trains, the shorter duration of the 2-pulse train implies an increased bandwidth of the channel caused by the simultaneous transmission of an electric and a mechanical (or acoustic) signal. We stress that our findings on manipulation and signalling with pressure pulses should

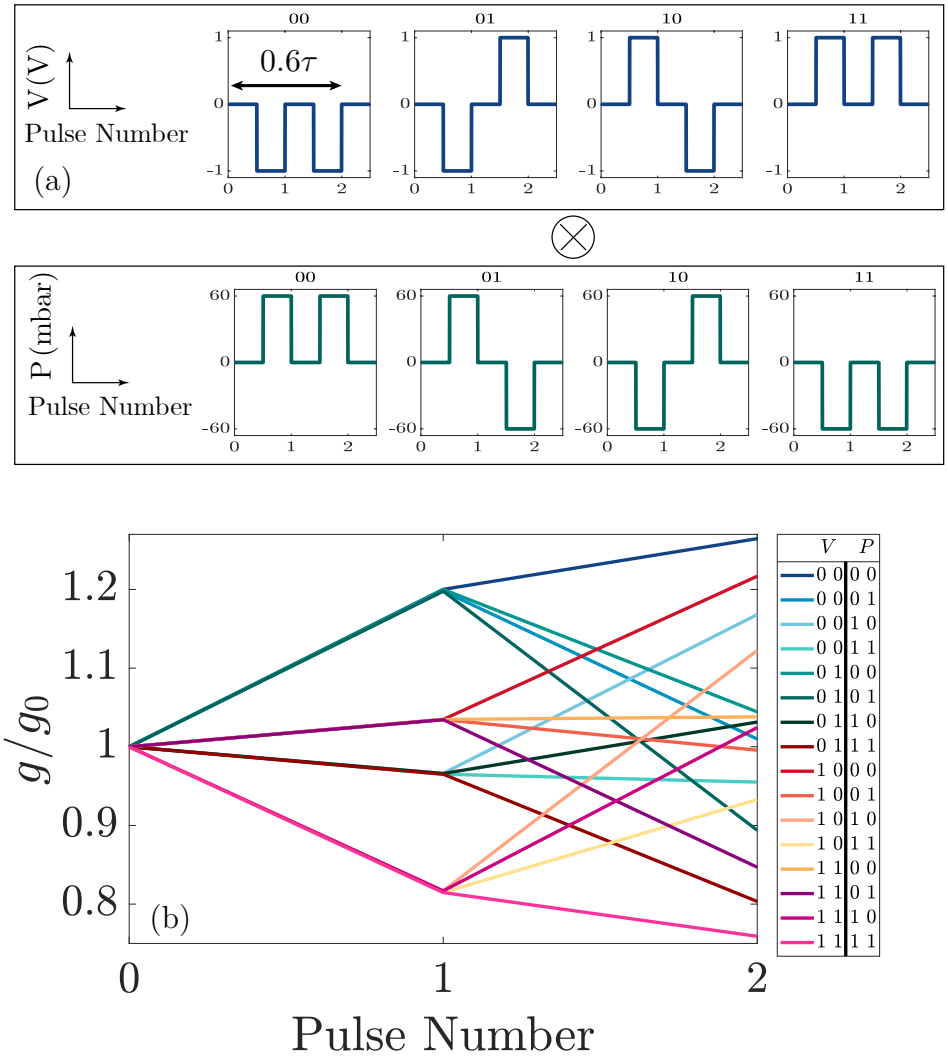

Figure 4.9: (a) Representation of all 16 possible combinations of independent 2-pulse trains of voltage and pressure of total duration 0.6τ. (b) Relative channel conductance $g(t)/g(0)$ at $t/\tau = 0.3$ and 0.6 for all 16 possible voltage-pressure trains leading to 16 different resulting conductances at $t = 0.6\tau$.

apply to any conical channel as this concerns merely intrinsic features of such a device. Therefore, these results represent a significant step beyond the use of pressure pulses as sensory input [159].

4.4 SUMMARY AND DISCUSSION

In conclusion, we theoretically predict on the basis of conventional transport theory for aqueous electrolytes in a conical microfluidic channel, that pulsatile flow driven by a time-dependent pressure drop can be exploited to modify and enhance the time series processing of iontronic memristors. We show how pressure pulses can either enhance the distinction of voltage signals or be used as an independent second input to achieve simultaneous electrical and mechanical time series processing, consequently doubling the channel information processing bandwidth. The classification of such time series was already shown to be applicable for iontronic fluidic reservoir computing [123] and therefore our results here offer a direct relevance to future development of iontronic computing. No specific features are taken into consideration apart from the standard properties of conical channels, rather our results are an intrinsic feature that should materialise in any of the widely available experimental realisations of conical channels [119–121, 161–168]. Consequently we provide a clear experimentally accessible method of exploiting the unique feature of a mobile medium (water) into tangible information processing benefits.

4.5 APPENDIX

4.5.1 *Divergence-free time-dependent currents and flow*

The electric current $I(t)$ and the volumetric fluid flow $Q(t)$ through the conical channel described in the main text and schematically shown in Fig.1 are defined in terms of the radially integrated x-components of the ionic fluxes $\mathbf{J}_\pm(x,r,t)$ and the fluid velocity $\mathbf{u}(x,r,t)$, such that

$$\begin{pmatrix} Q(t) \\ I(t) \end{pmatrix} = \int_0^{R(x)} \begin{pmatrix} \mathbf{u}(x,r,t)\cdot\hat{\mathbf{x}} \\ e\Big(\mathbf{J}_+(x,r,t)-\mathbf{J}_-(x,r,t)\Big)\cdot\hat{\mathbf{x}} \end{pmatrix} 2\pi r \mathrm{d}r. \tag{B1}$$

Strictly speaking these expressions depend on the position in the channel $x \in [0,L]$, where we recall that the radius of channel is given by $R(x)$ that decreases linearly from a base radius R_b at $x = 0$ to a tip radius R_t at $x = L$ with L the length of the channel (see also main text). The incompressibility condition of the flow, $\nabla\cdot\mathbf{u} = 0$ as imposed in Eq. (4.2), combined with the no-slip and no-flux boundary conditions guarantee that $Q(t)$ is independent of x. To a high degree of accuracy this is confirmed by our solutions of the PNPS equations, that we present in the main text and here for our standard parameter set given by $L = 9.8$ μm, $R_b = 446$ nm, $R_t = 98$ nm and an aqueous electrolyte with Debye length $\lambda_D = 9.8$ nm and ionic diffusion coefficient $D = 1$ μm^2/ms such that memristor retention time equals $\tau = 8.33$ ms according to Eq.(5). For periodic driving by a simultaneous pressure $P(t) = P_0\sin(\omega t)$ and voltage $V(t) = V_0\sin(\omega t)$, with $V_0 = 1$ V, $P_0 = -60$ mbar, and frequency $\omega/2\pi = 25$ Hz, we show the resulting (limit cycle of) $Q(t)$ at many positions between $x/L \in [0.3,1]$ in Fig. 4.10(a). The collapse of these curves, which is excellent for $0.5 < x/L < 1$ for all times, is the hallmark for incompressibility of the flow, and the small deviations from collapse in the wider part of the channel at $x/L < 0.5$ can be attributed to the finite grid of the numerical calculations. For the same system parameters and driving, we plot the electric current $I(t)$ for the same set of positions in the channel in Fig. 4.10(b). Interestingly, whereas some degree of x-dependence of $I(t)$ could in principle be possible, the essentially perfect collapse of all curves indicates that the (differential) capacity of the channel is apparently so small that no sign of a net charge build up can be

detected anywhere in the channel. We conclude, therefore, that we can speak of *the* fluid flow $Q(t)$ and *the* current $I(t)$ through the channel, rather than of their local analogues that depend (weakly if at all) on the position in the channel.

4.5.2 *Pressure-induced widening of the conductance window*

In Fig. 4.8 of this chapter we consider the time-dependent channel conductance $g(t)$ due to simultaneously applied sequences of voltage and pressure block pulses, each of duration $\tau/8$ and magnitude $\pm(V_0, P_0)$ with $V_0 = 1$ V and either $P_0 = -60$ mbar or $P_0 = 0$. Here a single block pulse $-(V_0, P_0)$ can represent a binary "0" and $+(V_0, P_0)$ a binary "1". If each of these pulses is preceded by a period $\tau/8$ with zero voltage and pressure, a train of four pulses takes a time τ and can represent any of the 16 binary numbers between 0000 and 1111, where the latter is represented for the case $P_0 = -60$ mbar in Fig. 4.11(a). For our standard parameter set, and for $V(t)$ and $P(t)$ representing the "1111" signal of Fig. 4.11(a), we solve the PNPS equations and calculate the time-dependent current $I(t)$, from which the time-dependent channel conductance $g(t) = I(t)/V(t)$ follows. Here we use small and short voltage "read" pulses in between the block "write" pulses, such that $V(t)$ and $I(t)$ are not strictly zero and $g(t)$ is also (numerically) well defined during several short time intervals in between the block pulses. In Fig. 4.11(b) we plot (dark blue line) the relative channel conductance $g(t)/g(0)$ associated with the 1111 signal of Fig. 4.11(a). We see a progressive reduction of $g(t)$ during the block pulses and a tendency to relax back towards $g(0)$ in between the block pulses. This effect is attributed to ionic depletion and re-accumulation in the channel upon applying positive and zero voltages, respectively, occurring on the time scale τ so only taking place partially during the pulses and their intervals of duration $\tau/8$. The five connected light blue dots in Fig. 4.11(a) represent $g(t)/g(0)$ at $t = 0$ and at the very end of the n-th pulse for $n = 1, \ldots, 4$ at times $t = n\tau/4$, showing a steady decrease with n towards $g(\tau)/g(0) \simeq 0.8$.

In Fig. 4.8(b) of this chapter we present the channel conductance $g(t)$ for $4t/\tau = 1, 2, 3, 4$, so directly after each of the four pulses of the train, not only for the 1111 signal shown in Fig. 4.11(a) but for all 16 possible

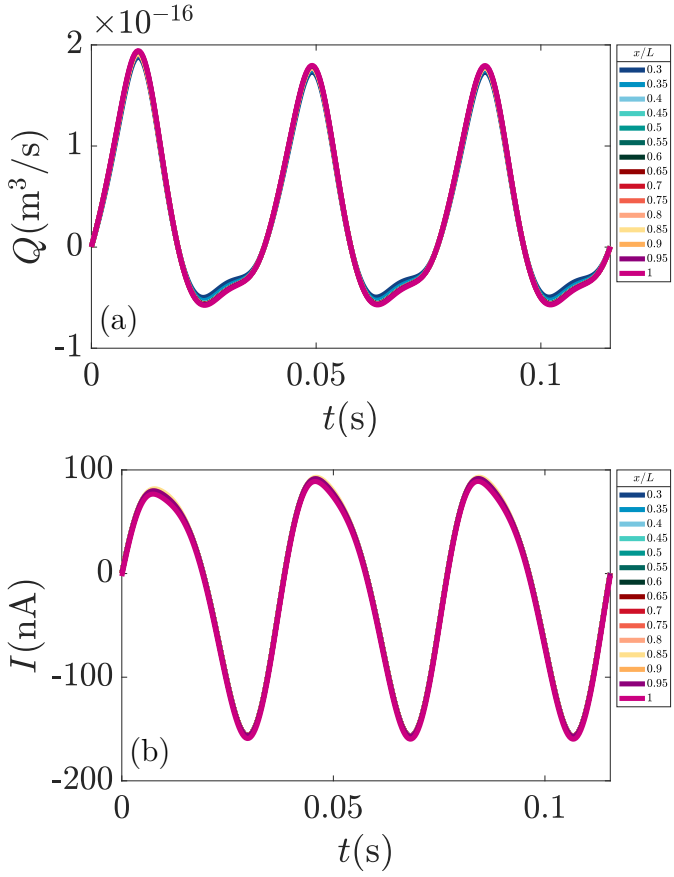

Figure 4.10: Time dependence of (a) the volumetric flow $Q(t)$ and (b) the electric current $I(t)$ during the limit cycle of a periodically driven conical channel as obtained at different positions $x \in [0, L]$ in the channel for our standard parameter set (see text). The flow and current are driven by a simultaneously applied drop of the voltage $V(t) = V_0 \sin(\omega t)$ and pressure $P(t) = P_0 \sin(\omega t)$ with $V_0 = 1$ V, $P_0 = -60$ mbar and driving frequency $\omega/2\pi = 25$ Hz.

trains at $P_0 = -60$ mbar. In Fig. 4.11(b) we present the same plot for the case with voltage pulses without simultaneous pressure pulses, so for

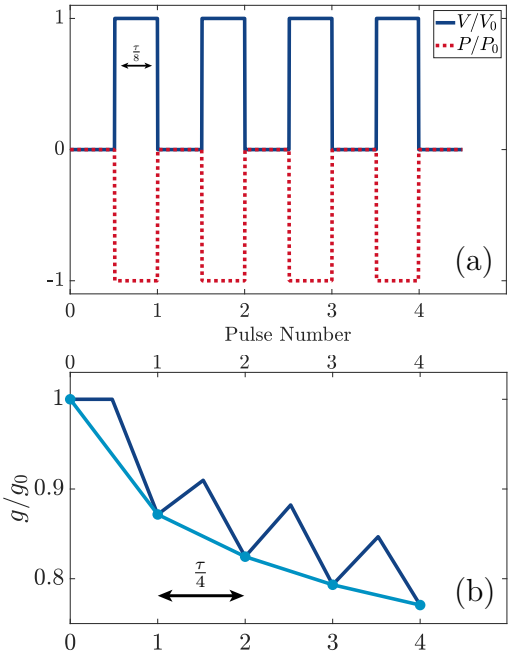

Figure 4.11: (a) Example of an external driving signal, representing the bit-string 1111 and consisting of a train of 4 block pulses $+(V_0, P_0)$ of positive voltage V_0 and negative pressure P_0, each of duration $\tau/8$ and separated by an interval $\tau/8$ with τ the typical retention time of salt in the channel. The magnitude of voltage and pressure ensure ideal conditions for salt depletion, which implies for our standard parameter set and the present case of $V_0 = 1$ V that $P_0 = -60$ mbar. (b) Evolution of the normalized channel conductance $g(t)/g_0$ (dark blue) under the influence of the driving of (a) that lowers the salt concentration in the channel, with $g_0 = g(0)$ the initial equilibrium conductance at zero voltage and zero pressure. The connected light blue dots represent the (scaled) conductance at the very end of each block pulse, which are time-separated by $\tau/4$.

$P_0 = 0$. This explicitly shows that the window of $g(t)$ with voltage-only pulses is substantially narrower than with pressure pulses of magnitude

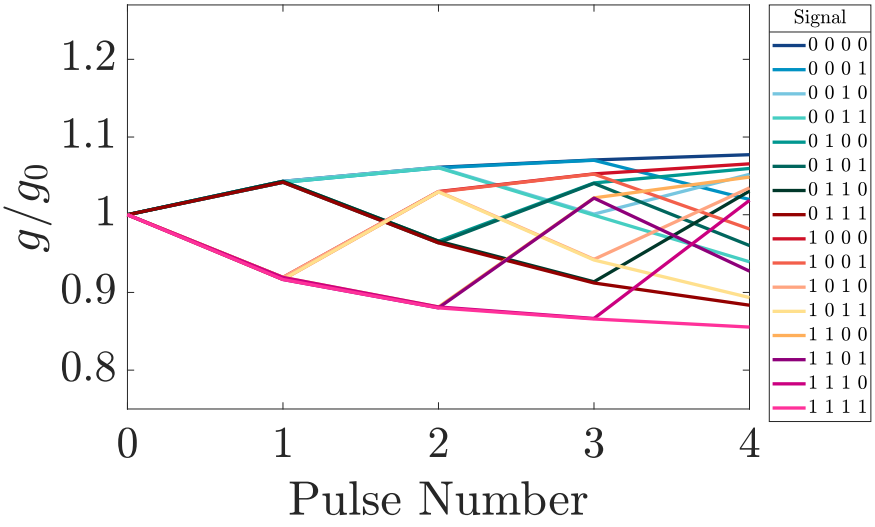

Figure 4.12: Relative channel conductance $g(t)/g_0$ at $4t/\tau = 0, 1, 2, 3, 4$ for all 16 combinations of trains (of duration τ) of four voltage pulses ($V_0 = \pm 1$ V, duration $\tau/8$) without pressure ($P_0 = 0$). The scale of the plot is identical to the scale of Fig. 4.8(b) of this chapter to emphasize the relatively narrow conductance window in the absence of pressure pulses.

$P_0 = -60$ mbar. The ordering of $g(t)$ at zero and at finite pressure remains the same, however, and one checks by a comparison with Fig. 4.8(a) of this chapter that the window of the conductance is set by the two extreme pulses representing 0000 and 1111, both for zero and for the nonzero pressure. Thus, without pressure the resulting 16 conductances at the end of the train are packed in a significantly narrower range, making it harder to resolve them.

ENGLISH SUMMARY

Studying the response of an aqueous electrolyte to an externally applied oscillating electric field is a very active research direction, as AC voltages can be used to achieve various goals in a wide range of practical applications in electrolytes. For example, an AC voltage can be used to drive electrokinetic pumps, induce fluid flow within microfluidic systems, manipulate charged colloids in aqueous electrolytes, desalinate and de-ionize the electrolyte using porous membranes, study the electrolyte dynamics with impedance and dielectric spectroscopy, render memristive properties to aqueous electrolytes in confinement, induced charge electrokinetics, particle assembly in electrolytes, AC electroosmosis, cyclic voltammetry, batteries, sensing and study bioparticles.

One of the key motivations to use (alternating) AC electric fields over (direct) DC fields is to eliminate any net current or net charge in the system due to the vanishing field when averaged over a period. In chapters 2 and 3 we will see, however, that the period-averaged current and charge do not necessarily vanish. The motivation for our study stems from recent experiments [S. H. Hashemi et al., *Physical Review Letters* **121**, 185504 (2018)] that have shown the existence a long-ranged steady electric field that emerges when applying an oscillating voltage $\Psi(t) = \Psi_0 e^{i\omega t}$ over an electrolyte with unequal mobilities of cations and anions confined between two planar blocking electrodes at a distance L from each other. To explain and quantify this asymmetric rectified electric field (AREF) as a function of many system parameters (such as amplitude and frequency of the voltage, system size), in Chapter 2 we analyse full numerical calculations based on the Poisson-Nernst-Planck equations by means of analytically constructed equivalent electric circuits. Surprisingly, we find that the equivalent circuit corresponding to the above electrolytic cell has two capacitive elements, rather than only one, which introduces a new timescale for electrolyte dynamics. We find good qualitative agreement between the numerical results and our simple analytic model, which shows that the long-range steady electric field

emerges from the different charging rates of cations and anions in the electric double layers (EDLs).

We consider large systems $\kappa L \gg 1$ (with κ^{-1} the Debye length) to avoid the EDL overlap and voltages of the order of at most several times the thermal voltage $\Psi_0 \leq 200\text{mV}$ in order for the point-ion approximation, that we use throughout the thesis, to be applicable. For such systems we find that AREF is maximized at $\omega\tau_{RC} \sim 1$, where the RC time τ_{RC} is the characteristic buildup time of an EDL.

In Chapter 3 building upon the findings and results of Chapter 2, we explore the generation of AREF by applying a sawtooth-like voltage to 1:1 electrolytes with equal diffusion coefficients confined between two planar blocking electrodes. This differs from the case of Chapter 2 based on a sinusoidal AC voltage applied to 1:1 electrolytes with unequal diffusion coefficients. By numerically solving the full Poisson-Nernst-Planck equations, we demonstrate that AREF can be generated by a slow rise and a fast drop of the potential (or vice versa), even for electrolytes with equal diffusion coefficients of the cations and anions. Similarly to Chapter 2, we employ an analytically constructed equivalent electric circuit to explain the underlying physical mechanism. Importantly, we find that the strength of AREF can be effectively tuned from zero to its maximal value by only manipulating the time-dependence of the driving voltage, eliminating the necessity to modify the electrolyte composition between experiments. This provides valuable insights to control the manipulation of AREF, which facilitates enhanced applications in diverse electrochemical systems.

Finally, in Chapter 4 we study a microfluidic conical channel exposed to simultaneously applied time-dependent voltage and pressure drops through numerical solutions of the Poisson-Nernst-Planck-Stokes equations for ion and fluid transport. Such channels are known to exhibit memristive properties when subjected to an AC driving voltage in the form of a hysteresis in the current-voltage curve. The intrinsic mobility of the medium (water) of dissolved ions in aqueous electrolytes, which therefore not only respond to voltage but also to pressure, is the characteristic feature of emerging iontronic devices for information processing that has been hitherto unexploited. We show that the channel's memristive properties can be enhanced, reduced or instantaneously reset by a suitable pressure, and we leverage this finding

with two examples of time series processing of simultaneously applied voltage and pressure pulses. We not only show that the distinction between different voltage time series can be improved by enhancing the conductance response with corresponding pressure pulses, but also that the bandwidth of information transfer through the channel can be doubled by letting the pressure pulses represent a second independent time series.

NEDERLANDSE SAMENVATTING

Het bestuderen van de reactie van een waterig elektrolyt op een extern aangelegd oscillerend elektrisch veld is een zeer actieve onderzoeksrichting, aangezien wisselspanningen kunnen worden gebruikt om verschillende doelen te bereiken in een breed scala van praktische toepassingen in elektrolyten. Bijvoorbeeld, een wisselspanning kan worden gebruikt om elektrokinetische pompen aan te drijven, vloeistofstromen op te wekken binnen microfluïdische systemen, geladen colloïden te manipuleren in waterige elektrolyten, het elektrolyt te ontzilten en te de-ioniseren met behulp van poreuze membranen, de elektrolytdynamica te bestuderen met impedantie- en dielectrische spectroscopie, memristieve eigenschappen te geven aan waterige elektrolyten in een poreus materiaal, geïnduceerde ladingelektrokinetica, deeltjesassemblage in elektrolyten, wisselstroomelektroforese, cyclische voltammetrie, batterijen, sensoren en het bestuderen van biodeeltjes.

Een van de belangrijkste motivaties om (alternerende) AC-elektrische velden te gebruiken in plaats van (directe) DC-velden is om eventuele netto stromen of netto ladingen in het systeem te elimineren als gevolg van het verdwijnen van het veld wanneer gemiddeld wordt over een periode. In hoofdstukken 2 en 3 zullen we echter zien dat de periode-gemiddelde stroom en lading niet noodzakelijk verdwijnen. De motivatie voor onze studie komt voort uit recente experimenten [S. H. Hashemi et al., *Physical Review Letters* **121**, 185504 (2018)] die hebben aangetoond dat er een lange-dracht stabiel elektrisch veld ontstaat wanneer een oscillerende spanning $\Psi(t) = \Psi_0 e^{i\omega t}$ wordt aangebracht over een elektrolyt met ongelijke mobiliteiten van kationen en anionen ingesloten tussen twee vlakke blokkerende elektroden op een afstand L van elkaar. Om dit asymmetrische gelijkgerichte elektrische veld (AREF) te verklaren en kwantificeren als een functie van vele systeemparameters (zoals amplitude en frequentie van de spanning, systeemgrootte), analyseren we in hoofdstuk 2 volledige numerieke berekeningen gebaseerd op de Poisson-Nernst-Planck-vergelijkingen door middel van analytisch geconstrueerde equivalente elektrische circuits. Tot onze verrassing vinden we

dat het equivalente circuit dat overeenkomt met de bovengenoemde elektrolytische cel twee capacitieve elementen heeft, in plaats van slechts één, wat een nieuw tijdsschaal voor elektrolytdynamica introduceert. We vinden een goede kwalitatieve overeenstemming tussen de numerieke resultaten en ons eenvoudige analytische model, wat laat zien dat het lange-drachts stabiele elektrische veld voortkomt uit de verschillende laadsnelheden van kationen en anionen in de elektrische dubbellagen (EDL's).

We beschouwen grote systemen $\kappa L \gg 1$ (met κ^{-1} de Debye-lengte) om de overlap van de EDL te vermijden en spanningen van de grootteorde van hooguit van enkele malen de thermische spanning $\Psi_0 \leq 200\text{mV}$ om de puntionbenadering, die we gedurende de hele these gebruiken, van toepassing te laten zijn. Voor dergelijke systemen vinden we dat AREF gemaximaliseerd wordt bij $\omega\tau_{RC} \sim 1$, waarbij de RC-tijd τ_{RC} de karakteristieke opbouwtijd is van een EDL.

In hoofdstuk 3, voortbouwend op de bevindingen en resultaten van hoofdstuk 2, onderzoeken we de opwekking van AREF door een zaagtandachtige spanning toe te passen op 1:1 elektrolyten met gelijke diffusiecoëfficiënten ingesloten tussen twee vlakke blokkerende elektroden. Dit verschilt van het geval van hoofdstuk 2 gebaseerd op een sinusvormige AC-spanning toegepast op 1:1 elektrolyten met ongelijke diffusiecoëfficiënten. Door de volledige Poisson-Nernst-Planck-vergelijkingen numeriek op te lossen, demonstreren we dat AREF kan worden gegenereerd door een langzame stijging en een snelle daling van de potentiaal (of vice versa), zelfs voor elektrolyten met gelijke diffusiecoëfficiënten van de kationen en anionen. Net als in hoofdstuk 2, maken we gebruik van een analytisch geconstrueerd equivalent elektrisch circuit om het onderliggende fysische mechanisme te verklaren. Belangrijk is dat we vinden dat de sterkte van AREF effectief kan worden afgestemd van nul tot zijn maximale waarde door alleen de tijdsafhankelijkheid van de aandrijfspanning te manipuleren, waarbij de noodzaak wordt geëlimineerdom de samenstelling van het elektrolyt tussen experimenten te wijzigen. Dit biedt waardevolle inzichten om de manipulatie van AREF te controleren, wat verbeterde toepassingen in diverse elektrochemische systemen mogelijk maakt.

Ten slotte, in hoofdstuk 4 bestuderen we een microfluïdisch kegelvormig kanaal dat tegelijkertijd wordt blootgesteld aan een tijdsafhankelijke spanning

en drukval door numerieke oplossingen van de Poisson-Nernst-Planck-Stokes-vergelijkingen voor ion- en vloeistoftransport. Dergelijke kanalen vertonen memristieve eigenschappen wanneer ze worden onderworpen aan een AC-aandrijfspanning in de vorm van een hysterese in de stroom-spanningscurve. De intrinsieke mobiliteit van het medium (water) van opgeloste ionen in waterige elektrolyten, die daarom niet alleen reageren op spanning maar ook op druk, is het karakteristieke eigenschap van opkomende iontronische apparaten voor informatieverwerking dat tot nu toe onbenut is gebleven.

We laten zien dat de memristieve eigenschappen van het kanaal kunnen worden verbeterd, verminderd of onmiddellijk kunnen worden gereset door een geschikte druk, en we maken gebruik van deze bevinding met twee voorbeelden van tijdsreeksverwerking van tegelijkertijd aangebrachte spannings- en drukpulsen. We tonen niet alleen aan dat het onderscheid tussen verschillende spanningsreeksen kan worden verbeterd door de geleidingsrespons te verbeteren met overeenkomstige drukpulsen, maar ook dat de bandbreedte van de informatieoverdracht door het kanaal kan worden verdubbeld door de drukpulsen een tweede onafhankelijke tijdsreeks te laten vertegenwoordigen.

ACKNOWLEDGEMENTS

First and foremost I would like to thank René. I could probably go on saying many things here. This PhD has been quite a journey. It had many ups and surprisingly many external downs as well. But no matter what was happening, I knew that I could always rely on you. Even when I did not use all the additional support that you offered (e.g. during the pandemic), just the fact of knowing that you were ready to help was very encouraging. I think there is no better way of saying that I was very happy to work with you than to state that despite all the external downs, I will save the PhD as a very good memory. Additionally, all the freedom and flexibility that you were offering was crucial as it taught me how to be more independent and take important responsibilities on board. Looking back at it, I consider this to be one of the crucial aspects of the PhD. At the same time I should definitely mention your patience as well... especially while correcting my drafts where I was prioritizing the 0^{th} and 1^{st} order results and missing a lot of 2^{nd} order details (and still some 0^{th} and 1^{st} order ones, truth be told). As I said, I could go on, but I will keep it short and will only briefly mention the trip to Avignon, during which we talked quite a lot and I got to know you as a "non-supervisor" as well, which was very interesting. Thus, thank you again for everything - I enjoyed it a lot!

Proceeding with the university hierarchy in mind, I would like to thank Rembert and Dirk for making the lunches fun for people with their sense of humor. Rembert's skill of maintaining a composed expression while delivering a joke, combined with Dirk's approach of skillfully and carefully wrapping the humor into trademark German seriousness, significantly enhanced the atmosphere at the table. Thanks Rembert for organizing all the cycling tours as well! I really enjoyed them and will be great if it becomes an ITF tradition. I would also like to thank Lars, with whom, despite him being quite elusive, I still managed to talk quite a bit. The vast variety and the spiciness of the topics that could have been discussed with you just using pure logic without sugarcoating anything and feeling relaxed at the same was like a breath of

fresh air. I would also like to thank JOOST - to be honest, before getting to know you, I was a bit afraid to be the TA for Statistical Physics :D, I ended up enjoying working with you on that course a lot and got to know you from a different angle! It was also fun to chase bats in the corridors and offices with you and I should also highlight the word "spelunking" that you told me - I had no idea that such a word even existed.

It is a pity that I did not have a chance to talk more to all of you outside of work environment.

I would also like to thank the members of the secretariat - MARIELLE, ANNETTE and OLGA, for running the ITF, replenishing the fruit/vegetable supplies in the bowls on the tables and putting "iets lekkers" in the lunchroom every Thursday!

Next I would like to thank WILLEM for many things - helping me adapt at the start of my PhD, all the interesting, useful and helpful discussions that we had during the PhD. Of equal importance was all the fun that we had outside of work like spending amazing time at Callantsoog beach parties laughing to death or spending an evening doing a pub crawl while sending weird (but utterly beautiful) emails to an important person after drinking quite a bit. I would also like to thank PETER - you were a symbol of calmness at the start of my PhD and helped me see what was actually important and not to worry about unimportant aspects of life and PhD. Besides the work-related discussions I also really enjoyed the general conversations with you as it was always interesting to see what your perspective on different topics was. I would also like to thank TIM for keeping me company in the final year as the sole fellow group member! And I really enjoyed our trip to Edinburgh where I got to know you better and saw you from a different perspective, which was cool.

And then there were the long-serving officemates - SOFIA and IRIS. I was very lucky to share the office with you. If I were to put it concisely, I would say that it was probably the nicest and the most comfortable experience of sharing a room with anyone, be it in or outside the office. All the talks, all the laughs, all the little presents, that started as sticker eyes and slowly transformed into Christmas hats and chicken, created truly an amazing atmosphere in the office. Truth be told, we had our share of downturns as well... when Iris's plants, which she brought to the office, ended up being on

life support (being an optimist I still hope they will make it through), when my computer kept making sounds in my absence, even though I thought I had muted it, when a bat was flying around like crazy inside our office and when the mugs were getting broken, but we stayed strong and got through all the hardships, emerging stronger than ever. And for that (and many more which was not mentioned here) I would like to thank both of them!

I would also like to thank my colleagues Emanuele (Emanuel, Emanuelle, Emmanuelle, Emmanuele, Emmanuel) (pick your favorite), Kim William, Meike, Jeroen, Joren, Artim (Leonardo Bassani), Tomas (heir of Federer in terms of soul and Medvedev in terms of game style, albeit with a tiny bit weaker backhand), Lumen, Anouar, Valentina, Marjolein, Elisa, Farshid, Tomislav, Hossein, Mick, Shradha, Mikael, Robin, William, Diego, Santiago, Yaïr, Vova, Masha, Maialen, Tess, Aravindh, David (dC), Genia, Alvaro. We shared many nice moments both at the ITF and outside of it during Callantsoog, ice rink skating, bike trips, football and other activities. I am very happy to have met you!

Next I would also like to thank Sebastian and Thijs who are the last of the Mohicans from the masters studies for me. It is always interesting to talk to you guys and I always have to be at my sharpest while expressing my opinion in your presence (especially to avoid Sebastian's wrath... a friendly one, but still very much a wrath), however, all of this in a very relaxed, exciting, friendly and pleasant atmosphere.

Another kind of special thanks goes to Aisesha, Ekboy, Alexander G, Daria, Georgy, Polina, Alexey K for all the moral support, interaction, activities, discussions and importantly - making me feel home. Happy that I met you.

Finally, I would like to thank my family for their loyal service as a sturdy, stable, firm, monolithic, irreplaceable, immovable, consistent, permanent, towering, vast, colossal, gargantuan, titanic and enormous supportive structure and a reference frame of my life. ⟍(◎o◎)⟋

I should also separately mention my grandparents who passed away during my Master's and PhD. They put a lot of effort into making me interested in physics and mysteries of life in general, while keeping the atmosphere fun, light and exciting at all times. They would have been very happy to see this thesis.

ABOUT THE AUTHOR

Alexander Barnaveli was born on 9th of May 1995 in Tbilisi, Georgia. From the early school years at Tbilisi G. Ramishvili 6th authorized German School he became interested in the structure of our Universe and the laws of Nature, inspired by his physicist grandfather's work in Cosmic Ray Physics. Later he transferred to Tbilisi I. Vekua 42nd school of Physics and Mathematics with advanced courses of physics and mathematics, where, during his late school years, he participated in several International Young Physicist Tournaments and Olympiads. This attractive process of learning and exploration of physical phenomena further developed his interest for the subject and led him to a decision to become a physicist.

After finishing school, he started studying physics at Free University of Tbilisi, however a year later he transferred to the Department of Physics of Tbilisi State University, which has a long tradition of teaching physical and mathematical sciences, where he finished his studies with a thesis in Astrophysics under the supervision of Prof. Dr. Nana Shatashvili in 2016. He continued his master's studies at Utrecht University and defended his thesis in Cosmology under the supervision of Dr. Tomislav Prokopec in 2018.

Due to a huge variety of reasons he then decided to change the direction of his career and in 2019 began his PhD under the supervision of Prof. Dr. René van Roij at the Institute of Theoretical Physics of Utrecht University, where he studied dynamic ion transport in electrolytes. The main results of his work, described in this thesis, have been presented at several (inter)national conferences. Some of it has already been published in a peer-reviewed scientific journal, whereas the other part is, as of writing of this piece, in the review process at other scientific journals.

BIBLIOGRAPHY

1. Barnaveli, A. & van Roij, R. Asymmetric rectified electric fields: nonlinearities and equivalent circuits. *Soft Matter* **20,** 704–716 (2024).
2. Barnaveli, A. & van Roij, R. *Asymmetric rectified electric fields for symmetric electrolytes* 2024. arXiv: 2404.15055 [cond-mat.soft].
3. Barnaveli, A., Kamsma, T. M., Boon, W. Q. & van Roij, R. *Pressure-Gated Microfluidic Memristor for Pulsatile Information Processing* 2024. arXiv: 2404.15006 [cond-mat.soft].
4. Jones, R. A. *Soft condensed matter* (Oxford University Press, 2002).
5. Frenkel, D. Soft condensed matter. *Physica A: statistical mechanics and its applications* **313,** 1–31 (2002).
6. Doi, M. *Soft matter physics* (Oxford University Press, USA, 2013).
7. Basak, R. & Bandyopadhyay, R. Encapsulation of hydrophobic drugs in Pluronic F127 micelles: effects of drug hydrophobicity, solution temperature, and pH. *Langmuir* **29,** 4350–4356 (2013).
8. Batrakova, E. V. & Kabanov, A. V. Pluronic block copolymers: evolution of drug delivery concept from inert nanocarriers to biological response modifiers. *Journal of controlled release* **130,** 98–106 (2008).
9. Chelu, M. & Musuc, A. M. Polymer gels: Classification and recent developments in biomedical applications. *Gels* **9,** 161 (2023).
10. Huber, P. Soft matter in hard confinement: phase transition thermodynamics, structure, texture, diffusion and flow in nanoporous media. *Journal of Physics: Condensed Matter* **27,** 103102 (2015).
11. Pathria, R. & Beale, P. *Statistical Mechanics. [Sl]* 1996.
12. Lu, Y. *et al.* Aerosol-assisted self-assembly of mesostructured spherical nanoparticles. *Nature* **398,** 223–226 (1999).
13. Cui, H., Chen, Z., Zhong, S., Wooley, K. L. & Pochan, D. J. Block copolymer assembly via kinetic control. *Science* **317,** 647–650 (2007).

14. Thorsen, T., Roberts, R. W., Arnold, F. H. & Quake, S. R. Dynamic pattern formation in a vesicle-generating microfluidic device. *Physical review letters* **86,** 4163 (2001).

15. Dukhin, S. Non-equilibrium electric surface phenomena. *Advances in Colloid and Interface Science* **44,** 1–134. ISSN: 0001-8686 (1993).

16. Bernal, J. D., Fowler, R. H., *et al.* A theory of water and ionic solution, with particular reference to hydrogen and hydroxyl ions. *J. chem. Phys* **1,** 515–548 (1933).

17. Stillinger, F. H. Water Revisited. *Science* **209,** 451–457. eprint: https://www.science.org/doi/pdf/10.1126/science.209.4455.451 (1980).

18. Clark, G. N., Cappa, C. D., Smith, J. D., Saykally, R. J. & Head-Gordon, T. The structure of ambient water. *Molecular Physics* **108,** 1415–1433 (2010).

19. Rubinstein, I. & Zaltzman, B. Electro-osmotically induced convection at a permselective membrane. *Physical Review E* **62,** 2238 (2000).

20. Yethiraj, A. & van Blaaderen, A. A colloidal model system with an interaction tunable from hard sphere to soft and dipolar. *Nature* **421,** 513–517 (2003).

21. Welling, T. A. *et al.* Frequency-controlled electrophoretic mobility of a particle within a porous, hollow shell. *Journal of Colloid and Interface Science* **627,** 761–773 (2022).

22. Derjaguin, B. V. Theory of the stability of strongly charged lyophobic sol and of the adhesion of strongly charged particles in solutions of electrolytes. *Acta phys. chim. URSS* **14,** 633 (1941).

23. Verwey, E. J. & Overbeek, J. T. G. Long distance forces acting between colloidal particles. *Transactions of the Faraday Society* **42,** B117–B123 (1946).

24. Derjaguin, B. *et al.* The Derjaguin—Landau—Verwey—Overbeek (DLVO) theory of stability of lyophobic colloids. *Surface forces,* 293–310 (1987).

25. Singh, H. The milk fat globule membrane—A biophysical system for food applications. *Current opinion in colloid & interface science* **11,** 154–163 (2006).

26. Mulder, H. & Walstra, P. *The milk fat globule* (Commonwealth Agricultural Bureaux Farnham Royal, 1974).

27. Obeid, S. *et al.* The phase and charge of milk polar lipid membrane bilayers govern their selective interactions with proteins as demonstrated with casein micelles. *Journal of colloid and interface science* **534,** 279–290 (2019).

28. Provost, J. *The Science of Cooking: Milk* Accessed: 24th April 2024. 2024.

29. Helmholtz, H. Ueber einige Gesetze der Vertheilung elektrischer Ströme in körperlichen Leitern mit Anwendung auf die thierisch-elektrischen Versuche. *Annalen der Physik* **165,** 211–233. eprint: https://onlinelibrary.wiley.com/doi/pdf/10.1002/andp.18531650603 (1853).

30. Gouy, M. Sur la constitution de la charge électrique à la surface d'un électrolyte. *J. Phys. Theor. Appl.* **9,** 457–468 (1910).

31. Chapman, D. L. LI. A contribution to the theory of electrocapillarity. *The London, Edinburgh, and Dublin philosophical magazine and journal of science* **25,** 475–481 (1913).

32. Stern, O. ZUR THEORIE DER ELEKTROLYTISCHEN DOPPELSCHICHT. *Zeitschrift für Elektrochemie und angewandte physikalische Chemie* **30,** 508–516. eprint: https://onlinelibrary.wiley.com/doi/pdf/10.1002/bbpc.192400182 (1924).

33. Grahame, D. C. The electrical double layer and the theory of electrocapillarity. *Chemical reviews* **41,** 441–501 (1947).

34. Phillies, G. D. *Elementary lectures in statistical mechanics* (Springer Science & Business Media, 2000).

35. Gregersen, M. M., Olesen, L. H., Brask, A., Hansen, M. F. & Bruus, H. Flow reversal at low voltage and low frequency in a microfabricated ac electrokinetic pump. *Physical Review E* **76,** 056305 (2007).

36. Ajdari, A. Pumping liquids using asymmetric electrode arrays. *Physical Review E* **61,** R45 (2000).

37. Dukhin, S. S. Electrokinetic phenomena of the second kind and their applications. *Advances in colloid and interface science* **35,** 173–196 (1991).

38. Ramos, A., Morgan, H., Green, N. G. & Castellanos, A. AC electric-field-induced fluid flow in microelectrodes. *Journal of colloid and interface science* **217,** 420–422 (1999).

39. Studer, V., Pépin, A., Chen, Y. & Ajdari, A. An integrated AC electrokinetic pump in a microfluidic loop for fast and tunable flow control. *Analyst* **129,** 944–949 (2004).

40. Catalano, J. & Biesheuvel, P. AC-driven electro-osmotic flow in charged nanopores. *Europhysics Letters* **123,** 58006 (2018).

41. Woehl, T. *et al.* Bifurcation in the Steady-State Height of Colloidal Particles near an Electrode in Oscillatory Electric Fields: Evidence for a Tertiary Potential Minimum. *Physical Review X* **5,** 011023 (2015).

42. Bukosky, S. C. & Ristenpart, W. D. Simultaneous aggregation and height bifurcation of colloidal particles near electrodes in oscillatory electric fields. *Langmuir* **31,** 9742–9747 (2015).

43. Ristenpart, W., Aksay, I. A. & Saville, D. Electrically guided assembly of planar superlattices in binary colloidal suspensions. *Physical review letters* **90,** 128303 (2003).

44. Biesheuvel, P., Fu, Y. & Bazant, M. Electrochemistry and capacitive charging of porous electrodes in asymmetric multicomponent electrolytes. *Russian Journal of Electrochemistry* **48,** 580–592 (2012).

45. Campione, A. *et al.* Electrodialysis for water desalination: A critical assessment of recent developments on process fundamentals, models and applications. *Desalination* **434,** 121–160 (2018).

46. Al-Amshawee, S. *et al.* Electrodialysis desalination for water and wastewater: A review. *Chemical Engineering Journal* **380,** 122231 (2020).

47. Lasia, A. in *Modern aspects of electrochemistry* 143–248 (Springer, 2002).

48. Orazem, M. E. & Tribollet, B. Electrochemical impedance spectroscopy. *New Jersey* **1,** 383–389 (2008).

49. Solomentsev, Y., Böhmer, M. & Anderson, J. L. Particle clustering and pattern formation during electrophoretic deposition: a hydrodynamic model. *Langmuir* **13,** 6058–6068 (1997).

50. Cole, K. S. & Cole, R. H. Dispersion and absorption in dielectrics I. Alternating current characteristics. *The Journal of chemical physics* **9,** 341–351 (1941).

51. Fröhlich, H. & Maradudin, A. Theory of dielectrics. *Physics Today* **12,** 40–42 (1959).

52. Robin, P. *et al. Long-term memory and synapse-like plasticity in carbon-based nanofluidic channels* in *APS March Meeting Abstracts* **2022** (2022), Q02–012.

53. Robin, P. *et al.* Long-term memory and synapse-like dynamics in two-dimensional nanofluidic channels. *Science* **379,** 161–167 (2023).

54. Kamsma, T., Boon, W., ter Rele, T., Spitoni, C. & van Roij, R. Iontronic Neuromorphic Signaling with Conical Microfluidic Memristors. *Physical Review Letters* **130,** 268401 (2023).

55. Tada, S., Natsuya, T., Tsukamoto, A. & Santo, Y. Contactless cell trapping by the use of a uniform AC electric field. *Biorheology* **50,** 283–303 (2013).

56. Lim, J.-H., McCullen, S. D., Piedrahita, J. A., Loboa, E. G. & Olby, N. J. Alternating current electric fields of varying frequencies: effects on proliferation and differentiation of porcine neural progenitor cells. *Cellular Reprogramming (Formerly "Cloning and Stem Cells")* **15,** 405–412 (2013).

57. Helmholtz, H. Ueber einige Gesetze der Vertheilung elektrischer Ströme in körperlichen Leitern mit Anwendung auf die thierisch-elektrischen Versuche. *Annalen der Physik* **243,** 337–382 (1879).

58. Hashemi, A., Miller, G. H., Bishop, K. J. & Ristenpart, W. D. A perturbation solution to the full Poisson–Nernst–Planck equations yields an asymmetric rectified electric field. *Soft Matter* **16,** 7052–7062 (2020).

59. Balu, B. & Khair, A. S. A thin double layer analysis of asymmetric rectified electric fields (AREFs). *Journal of Engineering Mathematics* **129,** 4 (2021).

60. Torres, A., van Roij, R. & Téllez, G. Finite thickness and charge relaxation in double-layer interactions. *Journal of colloid and interface science* **301,** 176–183 (2006).

61. Hollingsworth, A. & Saville, D. A broad frequency range dielectric spectrometer for colloidal suspensions: cell design, calibration, and validation. *Journal of colloid and interface science* **257,** 65–76 (2003).

62. Mangelsdorf, C. & White, L. Dielectric response of a dilute suspension of spherical colloidal particles to an oscillating electric field. *Journal of the Chemical Society, Faraday Transactions* **93,** 3145–3154 (1997).

63. DeLacey, E. H. & White, L. R. Dielectric response and conductivity of dilute suspensions of colloidal particles. *Journal of the Chemical Society, Faraday Transactions 2: Molecular and Chemical Physics* **77,** 2007–2039 (1981).

64. Olesen, L. H., Bazant, M. Z. & Bruus, H. Strongly nonlinear dynamics of electrolytes in large ac voltages. *Physical Review E* **82,** 011501 (2010).

65. Bazant, M. Z., Thornton, K. & Ajdari, A. Diffuse-charge dynamics in electrochemical systems. *Physical review E* **70,** 021506 (2004).

66. Hashemi, A., Bukosky, S. C., Rader, S. P., Ristenpart, W. D. & Miller, G. H. Oscillating electric fields in liquids create a long-range steady field. *Physical review letters* **121,** 185504 (2018).

67. Hashemi, A., Miller, G. H. & Ristenpart, W. D. Asymmetric rectified electric fields generate flows that can dominate induced-charge electrokinetics. *Physical Review Fluids* **5,** 013702 (2020).

68. Hashemi, A., Miller, G. H. & Ristenpart, W. D. Asymmetric rectified electric fields between parallel electrodes: Numerical and scaling analyses. *Physical Review E* **99,** 062603 (2019).

69. Chen, X., Chen, X., Peng, Y., Zhu, L. & Wang, W. Dielectrophoretic Colloidal Levitation by Electrode Polarization in Oscillating Electric Fields. *Langmuir* **39,** 6932–6945 (2023).

70. Janssen, M. & Bier, M. Transient dynamics of electric double-layer capacitors: Exact expressions within the Debye-Falkenhagen approximation. *Physical Review E* **97,** 052616 (2018).

71. Rubinstein, I., Zaltzman, B., Futerman, A., Gitis, V. & Nikonenko, V. Reexamination of electrodiffusion time scales. *Physical Review E* **79,** 021506 (2009).

72. *Table of Diffusion Coefficients* https://www.aqion.de/site/diffusion-coefficients. Accessed: 17th November 2022).

73. Bikerman, J. Ionic theory of electroosmosis, the current flow and the surface conductivity. *Zeitschrift Fur Physikalische Chemie-Abteilung a-Chemische Thermodynamik Kinetik Elektrochemie Eigenschaftslehre* **163,** 378–394 (1933).

74. Kilic, M. S., Bazant, M. Z. & Ajdari, A. Steric effects in the dynamics of electrolytes at large applied voltages. II. Modified Poisson-Nernst-Planck equations. *Physical review E* **75,** 021503 (2007).

75. Fedorov, M. V. & Kornyshev, A. A. Towards understanding the structure and capacitance of electrical double layer in ionic liquids. *Electrochimica Acta* **53,** 6835–6840 (2008).

76. Bazant, M. Z., Kilic, M. S., Storey, B. D. & Ajdari, A. Towards an understanding of induced-charge electrokinetics at large applied voltages in concentrated solutions. *Advances in colloid and interface science* **152,** 48–88 (2009).

77. Macdonald, J. R. Theory of ac space-charge polarization effects in photoconductors, semiconductors, and electrolytes. *Physical review* **92,** 4 (1953).

78. Macdonald, J. R. Electrical response of materials containing space charge with discharge at the electrodes. *The Journal of Chemical Physics* **54,** 2026–2050 (1971).

79. Barker, G. The equivalent circuit for the electrical double layer. *Journal of Electroanalytical Chemistry (1959)* **12,** 495–503 (1966).

80. Abouzari, M. S., Berkemeier, F., Schmitz, G. & Wilmer, D. On the physical interpretation of constant phase elements. *Solid State Ionics* **180,** 922–927 (2009).

81. Geddes, L. Historical evolution of circuit models for the electrode-electrolyte interface. *Annals of biomedical engineering* **25,** 1–14 (1997).

82. Macdonald, J. R. Theory of the differential capacitance of the double layer in unadsorbed electrolytes. *The Journal of Chemical Physics* **22,** 1857–1866 (1954).

83. Kortschot, R. *Dielectric spectroscopy of colloidal quantum dots in apolar liquids* PhD thesis (University Utrecht, 2014).

84. Chua, L. Memristor-the missing circuit element. *IEEE Transactions on circuit theory* **18,** 507–519 (1971).

85. Strukov, D. B., Snider, G. S., Stewart, D. R. & Williams, R. S. The missing memristor found. *Nature* **453,** 80–83 (2008).

86. Jo, S. H. *et al.* Nanoscale memristor device as synapse in neuromorphic systems. *Nano letters* **10,** 1297–1301 (2010).

87. Yang, J. J., Strukov, D. B. & Stewart, D. R. Memristive devices for computing. *Nature nanotechnology* **8,** 13–24 (2013).

88. Kuzum, D., Jeyasingh, R. G., Lee, B. & Wong, H.-S. P. Nanoelectronic programmable synapses based on phase change materials for brain-inspired computing. *Nano letters* **12,** 2179–2186 (2012).

89. Prezioso, M. *et al.* Training and operation of an integrated neuromorphic network based on metal-oxide memristors. *Nature* **521,** 61–64 (2015).

90. Lanza, M. *et al.* Memristive technologies for data storage, computation, encryption, and radio-frequency communication. *Science* **376,** eabj9979 (2022).

91. Wang, Z. *et al.* Fully memristive neural networks for pattern classification with unsupervised learning. *Nature Electronics* **1,** 137–145 (2018).

92. Martinez-Calvo, A. *et al.* The fluidic memristor: collective phenomena in elastohydrodynamic networks. *arXiv preprint arXiv:2303.10777* (2023).

93. Waser, R., Dittmann, R., Staikov, G. & Szot, K. Redox-based resistive switching memories–nanoionic mechanisms, prospects, and challenges. *Advanced materials* **21,** 2632–2663 (2009).

94. Waser, R. & Aono, M. Nanoionics-based resistive switching memories. *Nature materials* **6,** 833–840 (2007).

95. Sawa, A. Resistive switching in transition metal oxides. *Materials today* **11,** 28–36 (2008).

96. Kim, K. M., Jeong, D. S. & Hwang, C. S. Nanofilamentary resistive switching in binary oxide system; a review on the present status and outlook. *Nanotechnology* **22,** 254002 (2011).

97. Valov, I., Waser, R., Jameson, J. R. & Kozicki, M. N. Electrochemical metallization memories—fundamentals, applications, prospects. *Nanotechnology* **22,** 254003 (2011).

98. Zhu, J., Zhang, T., Yang, Y. & Huang, R. A comprehensive review on emerging artificial neuromorphic devices. *Applied Physics Reviews* **7** (2020).

99. Rele, T. T. *Memristive Effects in Ionic Nanopores* MA thesis (2023).

100. Zhou, X. *et al.* Nanofluidic memristor by elastic deformation of nanopores with nanoparticles adsorption. *National Science Review,* nwad216 (2023).

101. Wang, D. *et al.* Transmembrane potential across single conical nanopores and resulting memristive and memcapacitive ion transport. *Journal of the American Chemical Society* **134,** 3651–3654 (2012).

102. Li, Y. *et al.* History-dependent ion transport through conical nanopipettes and the implications in energy conversion dynamics at nanoscale interfaces. *Chemical science* **6,** 588–595 (2015).

103. Wang, D. *et al.* Physical origin of dynamic ion transport features through single conical nanopores at different bias frequencies. *Chemical Science* **5,** 1827–1832 (2014).

104. Wang, D. & Wang, G. Dynamics of ion transport and electric double layer in single conical nanopores. *Journal of Electroanalytical Chemistry* **779,** 39–46 (2016).

105. Wang, D. *et al.* Correlation of ion transport hysteresis with the nanogeometry and surface factors in single conical nanopores. *Analytical chemistry* **89,** 11811–11817 (2017).

106. Sheng, Q., Xie, Y., Li, J., Wang, X. & Xue, J. Transporting an ionic-liquid/water mixture in a conical nanochannel: a nanofluidic memristor. *Chemical Communications* **53,** 6125–6127 (2017).

107. Brown, W. *et al.* Deconvolution of electroosmotic flow in hysteresis ion transport through single asymmetric nanopipettes. *Chemical Science* **11,** 5950–5958 (2020).

108. Brown, W., Kvetny, M., Yang, R. & Wang, G. Selective Ion Enrichment and Charge Storage through Transport Hysteresis in Conical Nanopipettes. *The Journal of Physical Chemistry C* **126,** 10872–10879 (2022).

109. Brown, W., Kvetny, M., Yang, R. & Wang, G. Higher ion selectivity with lower energy usage promoted by electro-osmotic flow in the transport through conical nanopores. *The Journal of Physical Chemistry C* **125,** 3269–3276 (2021).

110. Wang, D. *et al.* Hysteresis charges in the dynamic enrichment and depletion of ions in single conical nanopores. *ChemElectroChem* **5,** 3089–3095 (2018).

111. Ramirez, P. *et al.* Negative differential resistance and threshold-switching in conical nanopores with KF solutions. *Applied Physics Letters* **118** (2021).

112. Ielmini, D. & Wong, H.-S. P. In-memory computing with resistive switching devices. *Nature Electronics* **1,** 333–343 (2018).

113. Poggioli, A. R., Siria, A. & Bocquet, L. Beyond the tradeoff: Dynamic selectivity in ionic transport and current rectification. *The journal of physical chemistry B* **123,** 1171–1185 (2019).

114. White, H. S. & Bund, A. Ion current rectification at nanopores in glass membranes. *Langmuir* **24,** 2212–2218 (2008).

115. Wen, C., Zeng, S., Li, S., Zhang, Z. & Zhang, S.-L. On rectification of ionic current in nanopores. *Analytical chemistry* **91,** 14597–14604 (2019).

116. Proctor, J. E. *Theory of ion transport and ion current rectification in nanofluidic diodes* PhD thesis (Clemson University, 2021).

117. Woermann, D. Electrochemical transport properties of a cone-shaped nanopore: high and low electrical conductivity states depending on the sign of an applied electrical potential difference. *Physical Chemistry Chemical Physics* **5,** 1853–1858 (2003).

118. Woermann, D. Electrochemical transport properties of a cone-shaped nanopore: revisited. *Physical Chemistry Chemical Physics* **6,** 3130–3132 (2004).

119. Kovarik, M. L., Zhou, K. & Jacobson, S. C. Effect of conical nanopore diameter on ion current rectification. *The Journal of Physical Chemistry B* **113,** 15960–15966 (2009).

120. Lin, C.-Y., Yeh, L.-H. & Siwy, Z. S. Voltage-induced modulation of ionic concentrations and ion current rectification in mesopores with highly charged pore walls. *The journal of physical chemistry letters* **9,** 393–398 (2018).

121. Jubin, L., Poggioli, A., Siria, A. & Bocquet, L. Dramatic pressure-sensitive ion conduction in conical nanopores. *Proceedings of the National Academy of Sciences* **115,** 4063–4068 (2018).

122. Boon, W. Q., Veenstra, T. E., Dijkstra, M. & van Roij, R. Pressure-sensitive ion conduction in a conical channel: Optimal pressure and geometry. *Physics of Fluids* **34** (2022).

123. Kamsma, T. *et al.* Brain-inspired computing with fluidic iontronic nanochannels. *arXiv preprint arXiv:2309.11438* (2023).

124. Iler, R. K. *The colloid chemistry of silica and silicates* **1** (LWW, 1955).

125. Kamsma, T., Boon, W., Spitoni, C. & van Roij, R. Unveiling the capabilities of bipolar conical channels in neuromorphic iontronics. *Faraday Discussions* **246,** 125–140 (2023).

126. Du, C. *et al.* Reservoir computing using dynamic memristors for temporal information processing. *Nature communications* **8,** 1–10 (2017).

127. Midya, R. *et al.* Reservoir computing using diffusive memristors. *Advanced Intelligent Systems* **1,** 1900084 (2019).

128. Kim, D., Shin, J. & Kim, S. Implementation of reservoir Computing using volatile WOx-based Memristor. *Applied Surface Science,* 153876 (2022).

129. Pyo, J. & Kim, S. Non-volatile and volatile switching behaviors determined by first reset in Ag/TaOx/TiN device for neuromorphic system. *Journal of Alloys and Compounds* **896,** 163075 (2022).

130. Chua, L. If it's pinched it'sa memristor. *Semiconductor Science and Technology* **29,** 104001 (2014).

131. Womersley, J. R. Method for the calculation of velocity, rate of flow and viscous drag in arteries when the pressure gradient is known. *The Journal of physiology* **127,** 553 (1955).

132. Zhu, J. *et al.* An artificial spiking nociceptor integrating pressure sensors and memristors. *IEEE Electron Device Letters* **43,** 962–965 (2022).

133. Sangwan, V. K. & Hersam, M. C. Neuromorphic Nanoelectronic materials. *Nature Nanotechnology* **15,** 517–528 (2020).

134. Mehonic, A. & Kenyon, A. J. Brain-inspired computing needs a master plan. *Nature* **604,** 255–260 (2022).

135. Schuman, C. D. *et al.* A survey of neuromorphic computing and neural networks in hardware. *arXiv preprint arXiv:1705.06963* (2017).

136. Schuman, C. D. *et al.* Opportunities for neuromorphic computing algorithms and applications. *Nature Computational Science* **2,** 10–19 (2022).

137. Xia, Q. & Yang, J. J. Memristive crossbar arrays for brain-inspired computing. *Nature Materials* **18,** 309–323 (2019).

138. Van De Burgt, Y., Melianas, A., Keene, S. T., Malliaras, G. & Salleo, A. Organic electronics for neuromorphic computing. *Nature Electronics* **1,** 386–397. ISSN: 25201131 (July 2018).

139. Harikesh, P. C. *et al.* Ion-tunable antiambipolarity in mixed ion-electron conducting polymers enables biorealistic organic electrochemical neurons. *Nature Materials* **22,** 242–248. ISSN: 14764660 (Feb. 2023).

140. Harikesh, P. C. *et al.* Organic electrochemical neurons and synapses with ion mediated spiking. *Nature Communications 2022 13:1* **13,** 1–9. ISSN: 2041-1723 (Feb. 2022).

141. Luo, S. *et al.* Highly Bionic Neurotransmitter-Communicated Neurons Following Integrate-and-Fire Dynamics. *Nano Letters* **23,** 4974–4982. ISSN: 15306992 (June 2023).

142. Wang, Y. *et al.* Dynamic molecular switches with hysteretic negative differential conductance emulating synaptic behaviour. *Nature Materials 2022 21:12* **21,** 1403–1411. ISSN: 1476-4660 (Nov. 2022).

143. Chicca, E. & Indiveri, G. A recipe for creating ideal hybrid memristive-CMOS neuromorphic processing systems. *Applied Physics Letters* **116,** 120501. ISSN: 00036951 (Mar. 2020).

144. Robin, P., Kavokine, N. & Bocquet, L. Modeling of emergent memory and voltage spiking in ionic transport through angstrom-scale slits. *Science* **373,** 687–691 (2021).

145. Xiong, T. *et al.* Neuromorphic functions with a polyelectrolyte-confined fluidic memristor. *Science* **379,** 156–161 (2023).

146. Ramirez, P. *et al.* Neuromorphic responses of nanofluidic memristors in symmetric and asymmetric ionic solutions. *The Journal of Chemical Physics* **160** (2024).

147. Powell, M. R., Cleary, L., Davenport, M., Shea, K. J. & Siwy, Z. S. Electric-field-induced wetting and dewetting in single hydrophobic nanopores. *Nature nanotechnology* **6,** 798–802 (2011).

148. Han, S. H., Kim, S. I., Oh, M.-A. & Chung, T. D. Iontronic analog of synaptic plasticity: Hydrogel-based ionic diode with chemical precipitation and dissolution. *Proceedings of the National Academy of Sciences* **120,** e2211442120 (2023).

149. Ramirez, P., Gómez, V., Cervera, J., Mafe, S. & Bisquert, J. Synaptical tunability of multipore nanofluidic memristors. *The Journal of Physical Chemistry Letters* **14,** 10930–10934 (2023).

150. Kamsma, T., Rossing, E., Spitoni, C. & van Roij, R. Advanced iontronic spiking modes with multiscale diffusive dynamics in a fluidic circuit. *arXiv preprint arXiv:2401.14921* (2024).

151. Emmerich, T. *et al.* Ionic logic with highly asymmetric nanofluidic memristive switches. *arXiv preprint arXiv:2306.07617* (2023).

152. Sabbagh, B., Fraiman, N. E., Fish, A. & Yossifon, G. Designing with Iontronic Logic Gates-From a Single Polyelectrolyte Diode to an Integrated Ionic Circuit. *ACS Applied Materials & Interfaces* **15.** PMID: 37068481, 23361–23370. eprint: https://doi.org/10.1021/acsami.3c00062 (2023).

153. Li, J., Li, M., Zhang, K., Hu, L. & Li, D. High-Performance Integrated Iontronic Circuits Based on Single Nano/Microchannels. *Small,* 2208079 (2023).

154. Han, S. H., Oh, M.-A. & Chung, T. D. Iontronics: Aqueous ion-based engineering for bioinspired functionalities and applications. *Chemical Physics Reviews* **3,** 031302 (2022).

155. Xie, B. *et al.* Perspective on Nanofluidic Memristors: From Mechanism to Application. *Chemistry–An Asian Journal* **17,** e202200682 (2022).

156. Noy, A., Li, Z. & Darling, S. B. Fluid learning: Mimicking brain computing with neuromorphic nanofluidic devices. *Nano Today* **53,** 102043 (2023).

157. Keshari, B. K. *et al.* Light-and Pressure-Stimulated Silver Oxide (AgO x)-Based Memristors for In-Sensor Memory and Computing Applications. *ACS Applied Electronic Materials* (2024).

158. Zhang, X. *et al.* An artificial spiking afferent nerve based on Mott memristors for neurorobotics. *Nature communications* **11,** 51 (2020).

159. Liu, X. *et al.* Near-Sensor Reservoir Computing for Gait Recognition via a Multi-Gate Electrolyte-Gated Transistor. *Advanced Science* **10,** 2300471 (2023).

160. Kamsma, T., van Roij, R. & Spitoni, C. A simple mathematical theory for Simple Volatile Memristors and their spiking circuits. *arXiv preprint arXiv:2404.08647* (2024).

161. Cheng, L.-J. & Guo, L. J. Rectified ion transport through concentration gradient in homogeneous silica nanochannels. *Nano Letters* **7,** 3165–3171 (2007).

162. Siwy, Z. S. Ion-current rectification in nanopores and nanotubes with broken symmetry. *Advanced Functional Materials* **16,** 735–746 (2006).

163. Bush, S. N., Volta, T. T. & Martin, C. R. Chemical sensing and chemoresponsive pumping with conical-pore polymeric membranes. *Nanomaterials* **10,** 571 (2020).

164. Siwy, Z. *et al.* Rectification and voltage gating of ion currents in a nanofabricated pore. *EPL (Europhysics Letters)* **60,** 349 (2002).

165. Siwy, Z. *et al.* Preparation of synthetic nanopores with transport properties analogous to biological channels. *Surface Science* **532,** 1061–1066 (2003).

166. Siwy, Z. & Fuliński, A. Fabrication of a synthetic nanopore ion pump. *Physical Review Letters* **89,** 198103 (2002).

167. Fuliński, A., Kosińska, I. & Siwy, Z. Transport properties of nanopores in electrolyte solutions: the diffusional model and surface currents. *New Journal of Physics* **7,** 132 (2005).

168. Siwy, Z., Kosińska, I., Fuliński, A. & Martin, C. Asymmetric diffusion through synthetic nanopores. *Physical Review Letters* **94,** 048102 (2005).

169. Kosińska, I. & Fuliński, A. Asymmetric nanodiffusion. *Physical Review E* **72,** 011201 (2005).

170. Lan, W.-J., Holden, D. A. & White, H. S. Pressure-dependent ion current rectification in conical-shaped glass nanopores. *Journal of the American Chemical Society* **133,** 13300–13303 (2011).

171. Bazant, M. Z. & Squires, T. M. Induced-charge electrokinetic phenomena: theory and microfluidic applications. *Physical review letters* **92,** 066101 (2004).

172. Ramos, A., García-Sánchez, P. & Morgan, H. AC electrokinetics of conducting microparticles: A review. *Current Opinion in Colloid & Interface Science* **24,** 79–90 (2016).

173. Squires, T. M. Induced-charge electrokinetics: fundamental challenges and opportunities. *Lab on a Chip* **9,** 2477–2483 (2009).

174. Hermanson, K. D., Lumsdon, S. O., Williams, J. P., Kaler, E. W. & Velev, O. D. Dielectrophoretic assembly of electrically functional microwires from nanoparticle suspensions. *Science* **294,** 1082–1086 (2001).

175. Gierhart, B. C., Howitt, D. G., Chen, S. J., Smith, R. L. & Collins, S. D. Frequency dependence of gold nanoparticle superassembly by dielectrophoresis. *Langmuir* **23,** 12450–12456 (2007).

176. Gangwal, S., Cayre, O. J. & Velev, O. D. Dielectrophoretic assembly of metallodielectric Janus particles in AC electric fields. *Langmuir* **24,** 13312–13320 (2008).

177. Gangwal, S., Pawar, A., Kretzschmar, I. & Velev, O. D. Programmed assembly of metallodielectric patchy particles in external AC electric fields. *Soft Matter* **6,** 1413–1418 (2010).

178. Smith, P. A. *et al.* Electric-field assisted assembly and alignment of metallic nanowires. *Applied Physics Letters* **77,** 1399–1401 (2000).

179. Fan, D., Zhu, F., Cammarata, R. & Chien, C. Controllable high-speed rotation of nanowires. *Physical review letters* **94,** 247208 (2005).

180. Edwards, B., Engheta, N. & Evoy, S. Electric tweezers: Experimental study of positive dielectrophoresis-based positioning and orientation of a nanorod. *Journal of Applied Physics* **102** (2007).

181. García-Sánchez, P., Arcenegui, J. J., Morgan, H. & Ramos, A. Self-assembly of metal nanowires induced by alternating current electric fields. *Applied Physics Letters* **106** (2015).

182. Bazant, M. Z. & Squires, T. M. Induced-charge electrokinetic phenomena. *Current Opinion in Colloid & Interface Science* **15,** 203–213 (2010).

183. Song, Y. *et al.* AC electroosmosis-enhanced nanoplasmofluidic detection of ultralow-concentration cytokine. *Nano letters* **17,** 2374–2380 (2017).

184. Du, K., Song, J., Liu, W., Tao, Y. & Ren, Y. Multifrequency induced-charge electroosmosis. *Micromachines* **10,** 447 (2019).

185. Lee, C.-A., Teramoto, A. & Watanabe, H. Monte carlo simulation of nanowires array biosensor with AC electroosmosis. *IEEE Transactions on Electron Devices* **65,** 1932–1938 (2018).

186. Talapatra, S. & Chakraborty, S. Double layer overlap in ac electroosmosis. *European Journal of Mechanics-B/Fluids* **27,** 297–308 (2008).

187. Chiou, P.-Y., Ohta, A. T., Jamshidi, A., Hsu, H.-Y. & Wu, M. C. Light-actuated AC electroosmosis for nanoparticle manipulation. *Journal of Microelectromechanical Systems* **17,** 525–531 (2008).

188. Zhou, H., White, L. R. & Tilton, R. D. Lateral separation of colloids or cells by dielectrophoresis augmented by AC electroosmosis. *Journal of colloid and interface science* **285,** 179–191 (2005).

189. Wang, H., Thiele, A. & Pilon, L. Simulations of cyclic voltammetry for electric double layers in asymmetric electrolytes: A generalized modified poisson–nernst–planck model. *The Journal of Physical Chemistry C* **117,** 18286–18297 (2013).

190. Wang, H. & Pilon, L. Physical interpretation of cyclic voltammetry for measuring electric double layer capacitances. *Electrochimica Acta* **64,** 130–139 (2012).

191. Zhao, T., Zhao, S., Zhou, S. & Xu, Z. How Thermal Effect Regulates Cyclic Voltammetry of Supercapacitors. *arXiv preprint arXiv:2305.18713* (2023).

192. Aderyani, S. *et al.* Simulation of cyclic voltammetry in structural supercapacitors with pseudocapacitance behavior. *Electrochimica Acta* **390,** 138822 (2021).

193. Levey, K. J., Edwards, M. A., White, H. S. & Macpherson, J. V. Simulation of the cyclic voltammetric response of an outer-sphere redox species with inclusion of electrical double layer structure and ohmic potential drop. *Physical Chemistry Chemical Physics* **25,** 7832–7846 (2023).

194. Lin, Y., Lian, C., Berrueta, M. U., Liu, H. & van Roij, R. Microscopic model for cyclic voltammetry of porous electrodes. *Physical Review Letters* **128,** 206001 (2022).

195. Zhang, Z. & Faez, S. Iontronic microscopy of a tungsten microelectrode:" seeing" ionic currents under an optical microscope. *arXiv preprint arXiv:2303.10755* (2023).

196. Venkateswarlu, M. & Satyanarayana, N. AC conductivity studies of silver based fast ion conducting glassy materials for solid state batteries. *Materials Science and Engineering: B* **54,** 189–195 (1998).

197. Krichen, M., Megdiche, M., Guidara, K. & Gargouri, M. AC conductivity and mechanism of conduction study of lithium barium pyrophosphate Li 2 BaP 2 O 7 using impedance spectroscopy. *Ionics* **21,** 935–948 (2015).

198. Sheha, E. Ionic conductivity and dielectric properties of plasticized PVA0. 7 (LiBr) 0.3 (H2SO4) 2.7 M solid acid membrane and its performance in a magnesium battery. *Solid State Ionics* **180,** 1575–1579 (2009).

199. Pandey, M., Joshi, G. M., Deshmukh, K., Khutia, M. & Ghosh, N. N. Optimized AC conductivity correlated to structure, morphology and thermal properties of PVDF/PVA/Nafion composites. *Ionics* **20,** 1427–1433 (2014).

200. Eswaragomathy, S. *et al.* Preparation of pectin biopolymer electrolyte for zinc-ion battery application. *Ionics* **29,** 2329–2340 (2023).

201. Li, J., Yao, W., Martin, S. & Vaknin, D. Lithium ion conductivity in single crystal LiFePO4. *Solid State Ionics* **179,** 2016–2019 (2008).

202. Buvaneshwari, P., Mathavan, T., Selvasekarapandian, S., Vengadesh Krishna, M. & Meera Naachiyar, R. Preparation and characterization of biopolymer electrolyte based on gellan gum with magnesium perchlorate for magnesium battery. *Ionics* **28,** 3843–3854 (2022).

203. Tron, A., Yoon, T., Park, Y. D., Oh, S. M. & Mun, J. Surface modification of LiCoO2 by NASICON-Type ceramic materials for lithium ion batteries. *Journal of Nanoscience and Nanotechnology* **17,** 4977–4982 (2017).

204. Barsoukov, E. & Macdonald, J. R. *Impedance spectroscopy: theory, experiment, and applications* (John Wiley & Sons, 2018).

205. Balu, B. & Khair, A. S. The electrochemical impedance spectrum of asymmetric electrolytes across low to moderate frequencies. *Journal of Electroanalytical Chemistry* **911,** 116222 (2022).